ISAS - INTERNATIONAL SCHOOL FOR ADVANCED STUDIES

The Continuum of Radio Quiet AGNs

Thesis submitted for the degree of

"Magister Philosophiae"

Astrophysics Sector

Candidate:

Gian Luigi GRANATO

Supervisor:

Prof. D.W. SCIAMA
Prof. L. DANESE

Academic Year 1990/91

TRIESTE

SISSA - SCUOLA INTERNAZIONALE SUPERIORE DI STUDI AVANZATI
TRIESTE
Strada Costiera 11

Contents

Preface

The main subject of this master thesis is the origin of the continuum radiation we receive from radio quiet Active Galactic Nuclei (AGNs), with particular emphasis to the possible effects of dust in shaping this radiation.

Our study is based on a homogeneous sample of Seyfert 1 (Sy 1) nuclei. Low luminosity local AGNs such as Sy 1 nuclei play an important role in the progress of our understanding of nuclear activity, because their power with respect to the host galaxy is not overwhelming, giving us the potential opportunity to better investigate the relations and interactions between the nucleus and the host. This same circumstance very often constitutes a problem in interpreting the data, since the contamination of nuclear observables caused by other galactic components can be very important, especially in optical and infrared bands. We have therefore implemented some analysis methods which allow a reliable separation of the emissions of the nuclei and of the galaxies. These techniques, as well as the results obtained by using them, are presented and discussed in this thesis.

The plan of this work is the following. Chapter 1 reviews the main emission mechanisms thought to be responsible of the continuum we receive from radio quiet active galactic nuclei (RQ AGNs). In Chapter 2 it is defined the homogenous sample of 56 AGNs which are the object of our work. Then it is described a precise method for separating the nuclear and galaxian fluxes in the optical and near–IR bands, based on imaging data. This procedure, together with less sophisticated ones, have been extensively applied in the next two chapters. Chapter 3 is devoted to the discussion of near–IR data, and it is shown, among other things, that the nuclei largely dominate the 12 μm IRAS fluxes, whereas the galaxies are the major contributors at $\lambda \geq 60\mu m$. In Chapter 4 the optical results are presented. The better quality of optical data allows a discussion of the characteristics of the host galaxies. Finally, in Chapter 5, we have successfully used the simple dust model for the IR emission described by Barvainis (1987,1990) to fit the UV–optical-infrared spectral energy distributions (SEDs) of some AGNs of our sample, for which we have derived in the previous chapters nuclear optical and infrared magnitudes.

All the reported quantities have been normalized to $H_o = 50$ km s^{-1} Mpc^{-1} and $q_0 = 0.5$ whenever necessary.

Chapter 1

Continuum Radiation from Radio Quiet AGNs

Summary. This chapter reviews the main emission mechanisms thought to be responsible of the continuum we receive from radio quiet active galactic nuclei (RQ AGNs). In such objects the bulk of the power appears to be emitted in the spectral region between the far infrared and the extreme ultraviolet. The proposed models for these regimes are described with greater detail. The more reliable emission mechanisms are thermal in nature.

1.1 Introduction

No more than a decade ago, there was a broad consensus on the idea that non thermal processes led to the observed continuum emission from nearly all kind of active galactic nuclei (AGNs) and in all spectral regimes. This view was mainly based on the rapid variability and high degree of polarization displayed by a minority of them, which now are commonly referred to as Blazars (Optically Violently Variable (OVVs) and BL Lac objects), and comprise less than 10% of optically discovered AGNs.

In the intervening years the satellite observations in the far infrared, ultraviolet and X–ray bands, together with more sophisticated solid-state measurements in optical, near infrared and submillimetric bands from the earth, have made it possible to study the continuum emission of AGN over a very broad range of frequencies. The main general result of this observational effort is the growing evidence that the

emission mechanisms responsible for the observed radiation in blazar and non–blazar AGNs are like to be of very different nature. While the evidences for nonthermal processes in blazar are reinforced, it seems like that most of the power, and all the emission we observe in the 0.01–1000 μm region of non–blazar AGNs, is originated by thermal processes (e.g. Sanders et al. 1989; Lawrence et al. 1991). This fact neither necessarily means that these two classes of AGNs are intrinsically different, nor it implies that the *primary* radiation in non blazar-AGNs is thermal in origin.

Woltjer (1990) lists 11 classes of AGNs appearing in the literature and observationally distinct: Radio Galaxies (RG), Radio Quasars (QSR), BL Lac Objects, Optically Violent Variables (OVV), Radio Quiet Quasars (QSO), Seyfert 1 Galaxies (Sy 1), Seyfert 2 Galaxies (Sy 2), Low Ionization Nuclear Emission-Line Regions (LINER), Nuclear HII Regions, Star Burst Galaxies (SBG) and strong IRAS galaxies. However, in this thesis we concentrate ourselves on Sy 1s and QSOs which, following the more popular current view, we treat as the lower and higher luminosity counterpart of the same kind of object (e.g. Lawrence 1987). Indeed from now on, unless otherwise explicitly stated, we will refer our considerations to these classes of AGNs, which, to avoid confusion, we will indicate as RQ AGNs (Radio Quiet AGNs).

We begin this chapter by presenting the typical Spectral Energy Distribution (SED) of RQ AGNs from X–ray to radio bands (Section 1.2). At this stage, only the proposed radiation mechanism for the radio and X–ray emission are quickly recalled, while a more detailed discussion of the models for the IR and Optical–UV continuum, which dominates the energetic budget, is deferred to the subsequent Section 1.3.

1.2 Typical Broadband Spectra of RQ AGNs

In Fig. 1.1 is shown the mean SED from X–ray to radio wavelengths of different kinds of AGNs. In AGNs studies it has became customary to plot the SED in the plane $\log(\nu F_\nu)$ vs. $\log \nu$. There are two reasons why νF_ν is preferred to F_ν in plots: (i) since νF_ν is proportional to the power per logarithmic bandwidth ($\int F_\nu d\nu \propto \int F_\nu \nu d(\log \nu)$), it is easier to appreciate the relative energetical importance of the different spectral features when plotting against $\log \nu$; and (ii) since the SEDs of AGNs have νF_ν constant to within an order of magnitude over a broad range of frequency, plotting this quantity enables one to reduce the vertical plot range, in order to emphasize details in the shape.

In general the SEDs of RQ AGNs appear remarkably similar, even when we consider objects differing in bolometric luminosity by as much as 10^3. The bulk of the emission occurs between 100 Å and 300 μm, and this is true also for QSRs.

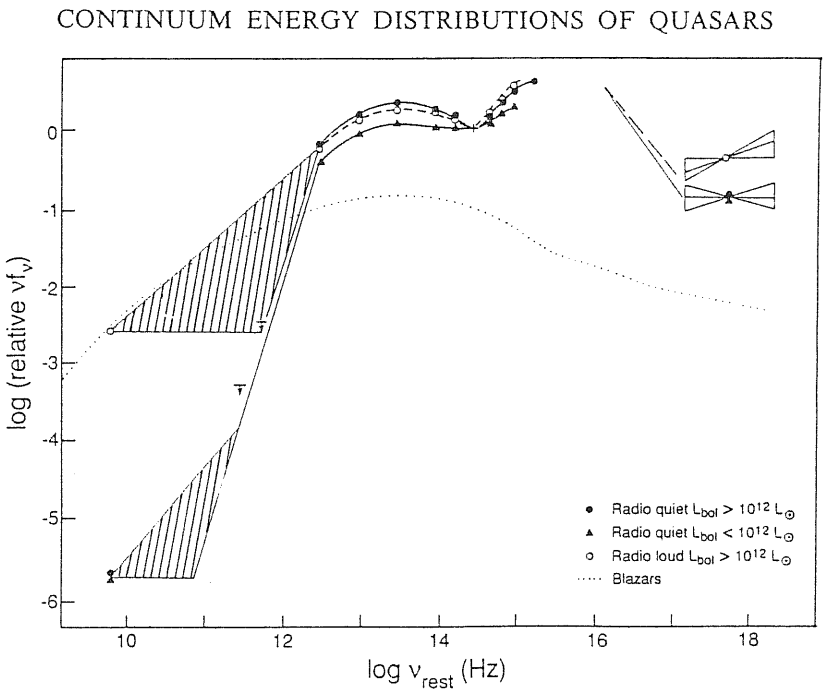

Figure 1.1: The mean continua of different kinds of AGN (from Sanders et al. 89)

In this range there appear to be two main broad components: an infrared bump between 1 and 300 μm (10^{12}–$10^{14.5}$ Hz), containing typically 1/3 of the bolometric luminosity, and an optical-UV bump between 100 Å and 1 μm ($10^{14.5}$–$10^{16.5}$ Hz). The minimum separating the two components has a nearly constant position around $10^{14.5}$ Hz. In the following paragraphs we will discuss the various spectral regimes with more details. To avoid confusion, we explicitly note that throughout this thesis, whenever we mention the spectral index α of a power law spectrum, we mean that $F_\nu \propto \nu^\alpha$.

1.2.1 Radio emission

Even radio quiet quasars have radio luminosities considerably greater than that of ordinary spiral galaxies, but, as apparent from Fig. 1.1, the power emitted in the radio region is nearly negligible compared to the bolometric luminosity, and this is true even if we consider radio loud quasars. The radio emission can be seen from scales of 1 pc up to at least 1 kpc. The radio spectrum of radio quiet AGNs is usually steep ($-1.1 < \alpha < -0.4$), but a few objects have compact flat spectrum cores. The fact that radio spectrum typically does not connect smoothly into the submillimeter-infrared regions suggests that it must be regarded as a distinct component, usually

interpreted as synchrotron radiation emitted by relativistic plasma.

1.2.2 The Infrared Bump

The SED of RQ AGNs rises sharply in the poorly observed region between 1000 and 100 μm (Lawrence et al. 1985), and has a convex shape in the 1–100 μm range, with a peak somewhere in between, as demonstrated by IRAS data at 12, 25, 60 and 100 μm. However, it must be kept in mind that these data have a very poor spatial resolution (typically $4' \times 2'$), with the result that in lower luminosity RQ AGNs (in practise Sy 1), the fluxes at 60 and 100 μm are mainly originated by the host galaxies, while those at 12 and 25 μm are indeed mainly nuclear in their origin (see Chapter 3).

Several authors (e.g. Edelson and Malkan 1986; Carleton et al. 1987) have pointed out the existence of an excess of emission in the near infrared above the "basic infrared continuum". The precise location and the shape of this bump depends on the shape of the supposed underlying basic continuum, typically a power law, and also on the quantity being plotted (F_ν or νF_ν). Therefore it has been referred to alternatively as 3 μm or 5 μm excess. Indeed, as noticed by Barvainis (1990), probably the near IR bump is not an isolated feature, but just the initial rising portion of the broad, continuous hump that extends sometimes out to 100 μm. When one tries to fit the IR continuum with a power law, the high degree of convex curvature in the near-IR tends to produce an excess over the power law in this region.

We will describe in some details the emission mechanisms proposed for the IR continuum in Section 1.3.2.

1.2.3 Optical–UV continuum: the Blue Bump

From 1μm down to the optical and UV region, the typical continuum of RQ AGNs rises continuously in the $\log F_\nu\nu$–$\log \nu$ plane, giving origin to one of the most interesting and well studied components in the AGN continuum, usually referred to as the *(big) blue bump*. The name is justified by the fact that in many papers this component has been regarded as an excess over a power law supposed to extend from the infrared to the X-ray (e.g. Malkan and Sargent 1982), and in this view the excess sets in around the B band. However most recent interpretations have cast serious doubts on the real existence of the underlying power law component in non-Blazar AGN (Sanders et al. 1989), and therefore the "blue bump" could well be the main continuum component from the optical to the soft X. This big blue bump is further contaminated by the *little blue bump*, in the near UV, consisting of Balmer

continuum emission (mostly important from 3700 to 3200 Å) and many unresolved Fe II emission multiplets (mostly from 2400 to 2700 Å), which accounts typically for $\sim 17\%$ of the apparent 2400–3800 Å continuum (see for instance Wills et al. 1985; Malkan 1988; Sun and Malkan 1989). The observational limit of the blue bump is usually set by data obtained with the International Ultraviolet Explorer (IUE), which is insensitive to radiation below 1200 Å. In some objects a turn-down or at least a flattening is seen in the shortest accessible part of the spectra (which need to be carefully corrected for galactic extinction), indicating that the peak in the power can occur between 1200 and 2000 Å (Malkan 1988; Sun and Malkan 1989), but in other cases the power peaks in the extreme UV (EUV) region, 1200–100 Å (Elvis et al. 1990). This result depends upon the continuum absorption correction applied to take into account the effect of material intrinsic to the AGN. This internal absorption is very difficult to asses, but even a modest amount of optical absorption can alter significantly the emitted spectrum in the UV region. The presence of an extremely soft X–ray component in some sources indicates that their internal absorbing columns must be less than 10^{21} cm^{-2} (Turner and Pounds 1989), and this would correspond to $A_V < 0.2$ in these sources for a standard gas to dust ratio of 100.

The proposed models for the Blue Bump continuum are discussed in Section 1.3.1.

1.2.4 X-ray Region

Continuum emission from RQ AGNs can be observed again at energies above 0.1 keV ($\log \nu > 16.4$), where the Galaxy becomes transparent once more. However in the *soft X* regime, between say 0.1 and 1 keV, extinction by the galactic disk gas and by gas intrinsic to the AGN is an important effect, which must to be taken into account in interpreting the data. Since the beginning of X–ray astronomy, RQ AGNs where recognized as powerful sources in this spectral range (Wilson 1979), and was discovered the strict proportionality between the H_α (broad) flux and the X–ray flux. The general result of spectral studies performed to date is that at energies exceeding 1 keV up to at least 10 keV (*hard X*), the continuum can be represented by a power law $F_\nu \propto \nu^\alpha$, which in hard X–ray selected samples has a remarkably uniform slope of -0.7 ± 0.2 (average deviation; see e.g. review by Mushotsky 1987), while in other samples, in particular in soft X–ray selected ones, the situation seems to be more complex (e.g. Elvis et al. 1986; Maccacaro et al. 1988; Sanders et al. 1989). Moreover, at lower energies, evidence has accumulated in the past few years for a "soft excess" in several sources above the power law determined in the hard X (see review by Pounds 1989 and references therein). This excess is often regarded as the hard tail of the blue bump.

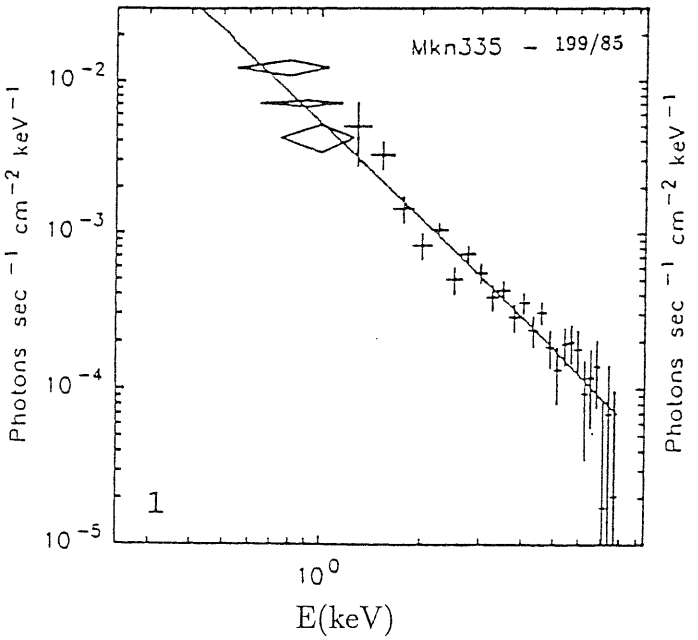

Figure 1.2: The 0.5–10 keV spectrum of the Sy 1 Mkn 335 (from Turner and Pounds 1989)

The origin of the X–ray emission is a quite open problem. Variability measurements, along with the rather uniform spectral shape above 2 keV, provide important clues that limit the possible models. Extensive monitoring programs have reported significant variations on the shortest accessible timescales ($\sim$ 100 s) for many objects, thereby demonstrating that the X–ray are produced in a small region. This fact, and the power law shaped hard X continuum, suggests a nonthermal emitting mechanism. Within the picture where an accretion disk and a massive black hole lie at the center of an AGN, this region is a natural site for X–ray production, for instance through a two phase accretion disk (Haardt and Maraschi 1991). In any case, the majority of the proposed models predicts a strict link between the UV and the X-ray continuum: X-ray photons can be produced by Compton upscattering of UV-optical photons by high energy electrons (e.g. Czerny and Elvis 1987; Maraschi and Molendi 1990; Haardt and Maraschi 1991), or, alternatively, X-ray primary photons may be in part reprocessed into UV-optical photons (see e.g. Collin-Souffrin 1991).

1.3 Interpretations

1.3.1 The Origin of the Blue Bump

The fact that the power usually peaks in the optical to soft X–ray region suggests an underlying physical mechanism closely linked to the ultimate energy source. Indeed, the big blue bump is generally attributed to optically thick emission of an accretion disk fuelling a central massive ($10^6 \div 10^9 M_\odot$) black hole (BH), in which the gravitational energy of the matter falling in the hole is dissipated and then thermally radiated. This idea was first introduced by Shields (1978) and soon welcome, since it was in agreement with the current orthodoxy, according to which the ultimate energy source in RQ AGNs is accretion on to a massive BH. The specific angular momentum of the gas orbiting in a typical galaxy is $\sim 10^{30}\mathrm{cm}^2\mathrm{s}^{-1}$, far larger than the maximal spin angular momentum of a BH ($\sim 5 \times 10^{23} M_8 \mathrm{cm}^2\mathrm{s}^{-1}$, where M_8 is the mass of the hole in units of $10^8 M_\odot$). Therefore this material cannot be accreted directly and settles in an accretion disk, where it slowly looses its angular momentum. Accretion with angular momentum is currently investigated in three different regimes: thin disks, radiation torii and ion torii, differing in the physical process (thermal pressure, gas pressure and electromagnetic stresses respectively) that dominate, in conjunction with gravity, in fixing the structure (see e.g. Begelman 1990; Frank et al. 1985; Treves et al. 1988). If the gas near the hole can cool in an inflow time, a thin disk will form. There are two opposite situations when this does not happen. When the accretion rate is high enough, yielding a luminosity at least of the order of the Eddington limit, radiation can be trapped in the surrounding gas which forms a radiation supported torus in orbit about the hole. Alternatively, if the accretion rate is low enough, and the viscosity large enough, a thick torus supported by ion pressure will be formed.

Another possible origin for the blue bump has been recently proposed: thermal emission by an assembly of "cold clouds" located very near the center, and condensing out of a hot spherical accretion flow (Lightman and White 1988; Guilbert and Rees 1988; Ferland and Rees 1988). In this class of models, mainly developed to account for the X ray spectra, the primary radiation is usually though to be the X–ray continuum, in part reprocessed by the cold clouds, while in models involving disk emission it is more natural to think that the primary continuum is that emitted by the disk itself.

O'Dell et al. (1987) have also proposed a non thermal model based on synchrotron emission from electrons secondary to pp collisions, in analogy to the non-thermal processes which are believed to be the main sources of the observed radiation in blazars.

However in this section we will concentrate on more standard disk models, in particular thin ones, for which extensive comparisons with observations do exist.

Thin disks

Indeed, almost all the published quantitative interpretations of observational data have been made in terms of disks models (Malkan 1983; Edelson and Malkan 1986; Wandel 1987; Band and A 1989; Sun and Malkan 1989), and more specifically that of a geometrically thin, optically thick accretion disk, which is the simplest case to treat, and is realized for luminosities below the Eddington luminosity, and when electromagnetic stresses can be ignored.

The first comparison between calculated disk spectra and the observed AGN continua from the IR to the UV was made by Malkan (1983), who noted that the blue bump has a shape broader than that of a single temperature blackbody, suggesting a range of temperatures of the emitting material, such as that of the surface of an accretion disk. In this and subsequent papers (Edelson and Malkan 1986; Band and A 1989; Sun and Malkan 1989) a thin disk model was used to fit the infrared to UV continuum of increasingly large samples of AGNs, together with a power law and other less important components such as a recombination continuum.

The structure of the disk used by Malkan and coworkers is that described by Novikov and Thorne (1973) and Page and Thorne (1974) , who extended the newtonian equations of the α-disk of Shakura and Sunyaev (1972), to include the effects of general relativity on an accretion disk in a Kerr metric. The disk is assumed to be sufficiently geometrically thin and optically thick that its surface flux is emitted as a blackbody. The radial distribution of the black body temperature, and therefore the emergent integrated spectrum, is then fixed by the *local* balance between the energy irradiated by the two disk surfaces and that dissipated by viscous torques in the interior. Because of the local blackbody assumption, the emergent spectrum is independent of the quite uncertain viscosity parameter α.

Neglecting for a moment the general relativistic effects on the propagation of the photons, once they leave the surface, the spectrum has at low frequencies the classical shape $f_\nu \propto \nu^{1/3}$, followed by a broad flat region and then by an exponential cutoff, less sharp than that of a single planck function, whose location is connected to the maximum temperature reached by the emitting surfaces at the interior edge of the disk.

The radius of this interior edge is set by the radius of the last stable orbit in a Kerr metric, and decreases for more rapidly rotating BHs. Therefore the hardness of the spectrum, as well as the efficiency of the disk, increases with increasing angular momentum of the BH. Two extreme cases are usually considered: nonro-

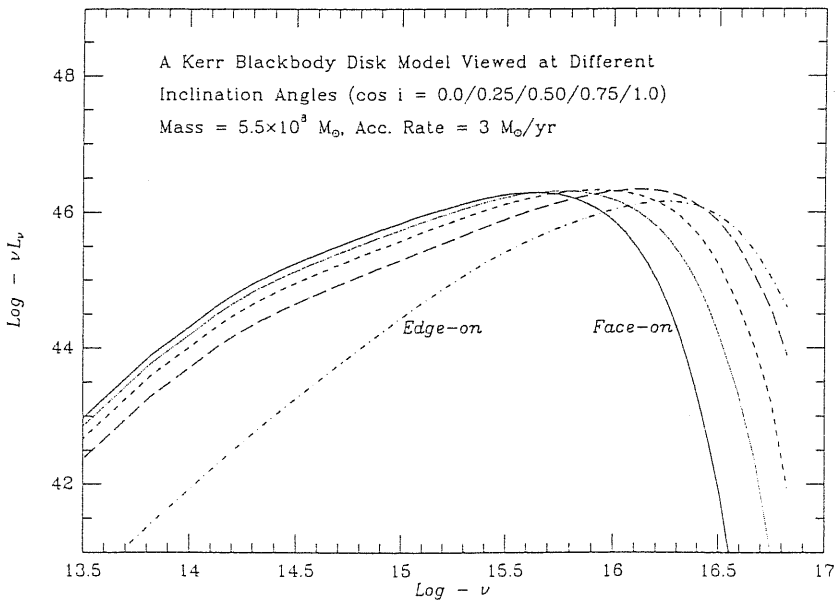

Figure 1.3: The dependence of an accretion disk spectrum on the viewing angle (from Sun and Malkan 1989)

tating (Schwarzschild) holes with a dimensionless angular momentum to mass ratio $a/M = 0$, or rapidly rotating (extreme Kerr) holes with $a/M = 0.988$. The latter case is usually considered more realistic, since the accreting matter soon spins the black hole up to this limiting value (Bardeen 1970), but it is also more complicated to compute because more heavily affected by relativistic effects. Indeed, the light emitted by the inner regions of the disk is affected by gravitational redshift and defocusing, and by Doppler beaming. These effects are of course much more important for rapidly rotating holes, and produce a strong inclination dependence, considered in details by Sun and Malkan (1989) who fit their model to the spectrum of 60 RQ AGNs. The dependence on inclination is in the sense that observers near the plane of the disk see a significantly harder spectrum than those who view the disk face on. These authors have also attempted to take into account the vertical structure of the disk, by introducing non–LTE model atmospheres in place of the crude blackbody assumption. However, this produced unacceptable fits and was not pursued (a similar problem was faced by Wade 1984 in a stellar accretion disk study).

The free disk parameters in these fits are the hole mass M and the accretion rate $\dot{M}$, while the angular moment (Schwarzschild or extreme Kerr) and the inclination angle are taken as given. Sun and Malkan (1989) used the extreme Kerr case and

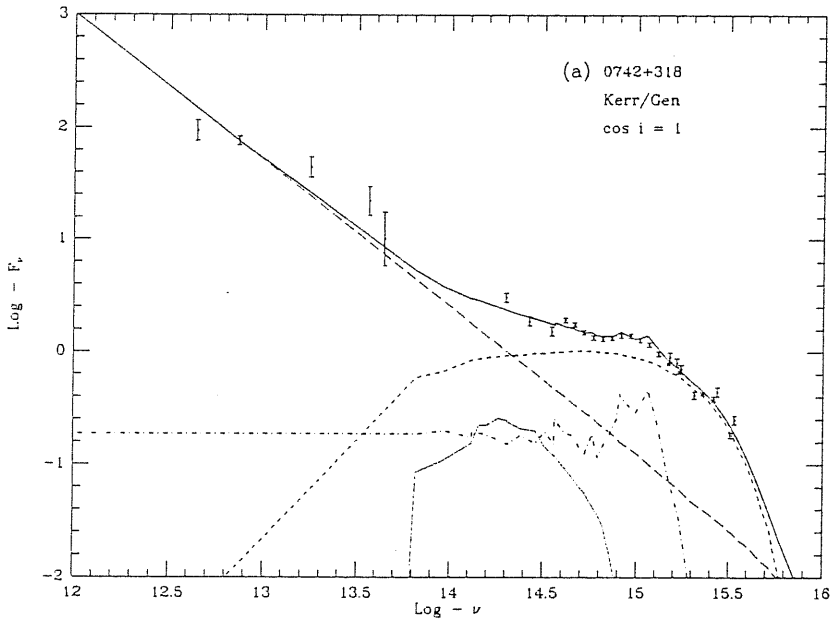

Figure 1.4: Multicomponent fit to the SED of a RQ AGNs (from Sun and Malkan 1989). The fit contains a disk (small dashes), a nonthermal power law (large dashes), recombination emission (dot–dash line), and a starlight component (dotted line)

found a simple inverse relation between the assumed inclination angle i and the inferred mass: $\log(M/M_{\text{face-on}}) = -1.2 \times \cos i + 1.2$, while the accretion rate is independent of i. For face on disks, the hole masses ranges from $10^{7.8} M_\odot$ for low luminosity Seyferts, up to $10^{9.7} M_\odot$ for high redshift luminous QSOs. Low redshift Seyfert galaxies are found to have relatively low accretion rates, only a few percent of their Eddington limit, while the most luminous QSOs are accreting near their Eddington limit.

A somewhat more realistic model has been investigated by Czerny and Elvis 1987, using a non-rotating BH, but taking into account the effects of free-free absorption, electron–scattering and comptonization, in place of employing the crude blackbody assumption. Since they where interested in a model to be used in fitting procedures, they where forced to take a simplified approach to these effects: in place of looking for exact solutions of a transfer equation, they derive simple formulas for a factor $f\nu$, describing the departures of the local spectrum from a blackbody, which can be used everywhere in the disk.

This model has been fit to the spectrum of only one object, a bright nearby

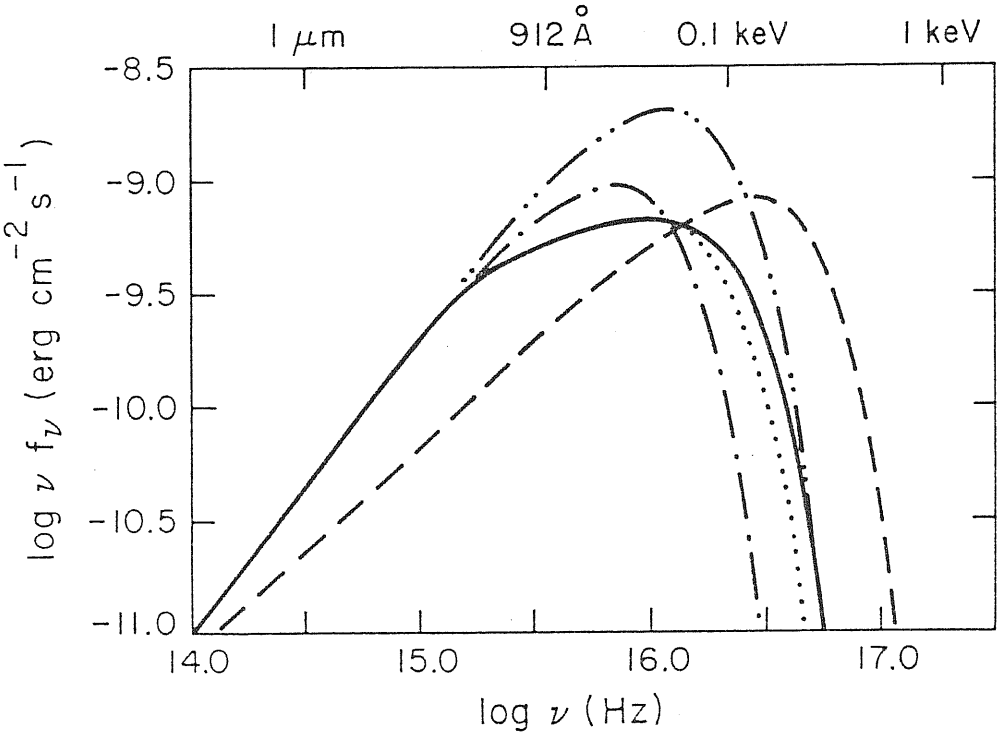

Figure 1.5: Face on disk spectra calculated with different assumption about the locally emitted radiation spectrum (from Czerny and Elvis 1987). Blackbody (dot–dashed curve), grey body (dashed curve), modified blackbody (dotted curve), and modified blackbody including Comptonization (solid curve). Disk parameters are $M = 10^8 M_\odot$, $\dot{M} = 10 M_\odot \mathrm{yr}^{-1}$, $\alpha = 0.1$, leading to $L/L_E \sim 2$. For comparison, it is also shown a blackbody–type spectrum (dot–dot–dashed curve) matching the final model at high frequencies. Required parameters corresponds then to $L/L_E = 17$.

quasar (PG 1211+143). According to the authors, the main advantages of such a model, with respect to those using the local blackbody approximation, are two: (i) the fact that the observed UV spectrum of many objects turns down close to $\sim$ 1200 Å is naturally explained by the onset of electron scattering, rather than by a maximum disk temperature that should be surprisingly uniform ($2 \div 3 \times 10^4$ K), and (ii) this opacity driven turndown is less dramatic, allowing to explain the strong EUV spectra and, introducing the effects of comptonization in a hot corona, soft X–ray excesses observed in some object, with lower, less super-Eddington, accretion rates (we remind that super-Eddington accretion rates are inconsistent with the thin disk approximation). For instance, for the object considered by the authors, the inferred disk parameters correspond to $L = 3L_E$, while using simpler models it was found $L = 20L_E$. This milder super-Eddington dilemma could be avoided

employing a more efficient geometry, namely that of a rotating black hole.

The most recent, and to date most physically complete spectra calculations for α–disks around massive black holes, are those of Laor and coworkers (Laor and Netzer 1989; Laor et al. 1990). In their models, the radiative transfer equations are solved by means of the Eddington approximation for an atmosphere with a vertical temperature gradient, including all significant sources of opacity for $T > 10^4$ K and full relativistic corrections. They have found the effect of electron scattering and comptonization to be less important compared with the more approximate model of Czerny and Elvis (1987) , resulting in a surface temperature everywhere close to the effective temperature. A detailed comparison of these calculations to observed spectra has been deferred to "another paper". However, the authors have stressed that some previous fit of AGN spectra through thin disk spectra are badly inconsistent with the thin disk approximation, due to the stringent upper limit they set on the luminosity ($L < 0.3L_E$) or accretion rate for its validity (see Fig. 1.6).

Indeed, it must be recognized that real problems remain in fitting the observed spectra with thin accretion disk model, suggesting to keep the mind open to alternative possibilities:

- Thin disk fit to the blue bump may be inconsistent with the requirement $L < 0.3L_E$, at least for bright quasars and/or if we want to explain the soft X–ray excesses observed in some objects as the tail of the disk emission.

- The thermal emission from a thin accretion disk is expected to be highly polarized, from 0 % for face-on disks up to $\geq$ 10% for edge on disks, since most of the radiation comes from regions where electron scattering is the main opacity source (Webb and Malkan 1986). The observed degree of optical polarization in non blazar AGNs is instead very low, less than 2%. This conflict has been regarded as a problem for thin disk models, which can be solved by geometrically thick disks (Coleman and Shields 1990). However more recent calculations (Laor et al. 1990) have shown that, taking into account general relativistic effects on the propagation of radiation and all the opacity sources, the expected polarization of thin disk radiation is reduced to levels consistent with available observations.

- Another possible problem with thin disks is that many calculations predict a large absorption discontinuity at the Lyman limit (λ916) (Kolykhalov and Sunyaev 1984; Laor and Netzer 1989), not confirmed by observations. In realistic accretion disks, the gas has a vertical structure whereby the density decreases vertically until it becomes transparent. This density gradient, coupled with the hydrogen bound–free opacity should produce a Lyman limit

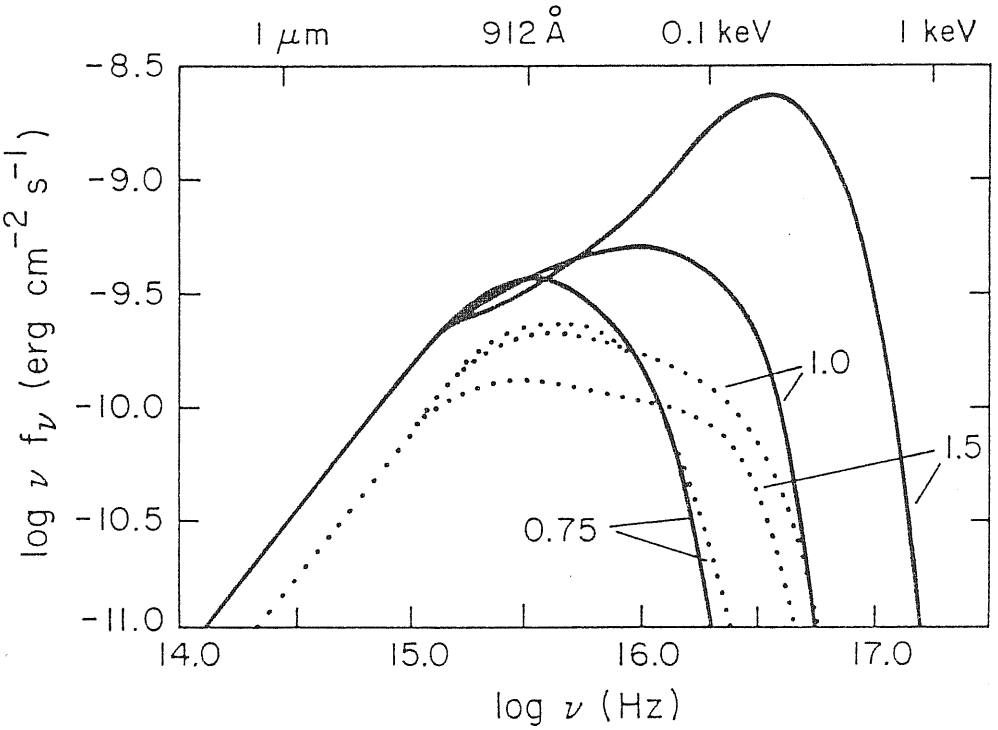

Figure 1.6: Disk profiles for non-rotating BH with different accretion rates (from Czerny and Elvis 1987). The luminosity, in units of the Eddington luminosity, is marked on the curves. The radius and the thickness are in units of the gravitational radius $2GM/c^2$. R_h is the radius inside which half of the total luminosity is emitted.

discontinuity, like in stellar atmospheres. However, as remarked by Laor et al. (1990) , this discontinuity may well be too small to be detected, because of the high effective temperatures of atmospheres in AGNs accretion disk.

Thick disks

The problems reported with thin disk interpretations of the blue bump, in particular the inferred accretion rates sometimes close or greater than the Eddington limit, has suggested some authors to consider thick disk models. Contrary to what happens with thin disk models, very little work has been devoted to calculate the emission from such systems in a suitable fashion for quantitative comparison with observed spectra. The only work in this direction know to us is that in (Madau 1988), but no one has yet published a quantitative comparison between theoretical and observed spectra, due both to the poorness of the relevant data (thick disks are expected to

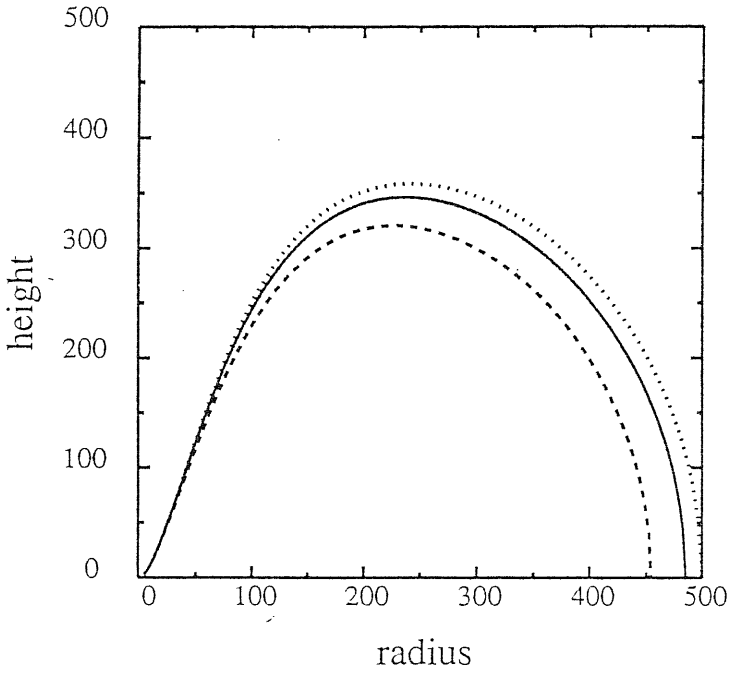

Figure 1.7: Meridional cross section of the model considered by Madau (1988). The radius and the thickness are in units of the gravitational radius $2GM/c^2$.

emit the bulk of their luminosity in the extreme UV region) and the uncertainties of the theory. Indeed, the thick disk theory is still in an initial stage (Treves et al. 1988), and up to now the majority of the efforts has been concentrated to investigate the self–consistency of the models. The main difficulties to be solved, in addition to those shared with thin disk theory, are inherent to the bi–dimensional structure and hence the diversity of the transport processes taking place inside the torus.

The model considered by Madau (1988) has a toroidal shape with a narrow funnel inside (fig. 1.7). As a consequence of this, its spectrum has a strong dependence on the viewing angle, which becomes more important at the highest frequencies. This dependence is in the sense that the spectrum becomes softer if the torus is observed from directions more close to the equatorial plane, and therefore is in the opposite direction to that found in thin disk (see pag. 15). In fact the hottest, more internal, parts of the disk surface are affected by self shadowing when the torus is seen nearly edge on. This dependence is however reduced if one takes into account the effects of multiple scatterings off the funnel walls (fig. 1.8 a and b), but can still have important effects on photoionization models of the BLR (e.g. Netzer 1997), and also on models explaining the infrared power as reprocessing of a primary optical–UV

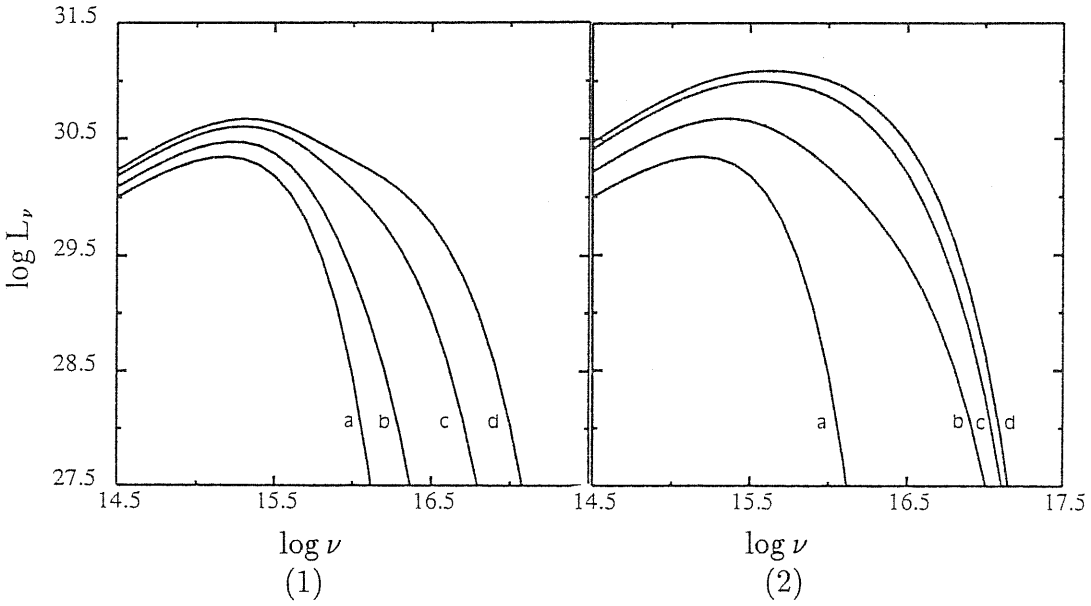

Figure 1.8: Thick disk spectra for different angles i between the rotation axis and the line of sight (from Madau 1988). Curves labeled a, b, c, and d are computed for $i = 90°$, $50°$, $25°$ and $0°$, respectively. Those in panel 1 and 2 are computed without and with inclusion of the reflection effect, respectively (see text)

radiation from a distribution of dust.

Concluding Remarks

In conclusion, the common interpretation of the blue bump as thermal emission of a thin disk is the only one extensively compared with observations, and undoubtedly with interesting results. However it must be noted that much of the work has been done with models somewhat unrealistic, due both to theoretical–computational and observational limitations. Indeed, the peak of the emission falls for many models in the EUV region, where the observations are not available and/or are affected by heavy and uncertain corrections (Galactic and internal reddening, intervening absorption line systems which depress the continuum shortward of Lyα). In principle, it might be possible to use the observed relative strengths of optical and UV emission lines to infer informations about the extreme-UV shape (Krolik and Kalmann 1987). The main problem with this approach is that the ionization parameter is much more important than the exact shape of the ionizing spectrum in determining the lines ratios.

Another point to mention is that virtually all the fitting work has been done assuming an underlying power law extrapolated from the IR region, whose existence seems now very doubtful.

Therefore we think that the only relatively firm conclusion about the blue bump is its thermal origin, but the precise class of models responsible for it is still uncertain and open to future investigation.

1.3.2 Origin of the Infrared Continuum

As we already anticipated, the commonly accepted origin for the infrared emission (1–1000 μm) in radio quiet AGNs has changed dramatically in the past two decades. In the mid 1970s, the favorite picture was that the IR region, as well as almost all the rest of the continuum, was produced trough nonthermal processes in all classes of AGNs. This view was based mainly on a minority of them (less than 8% of optically selected quasar samples), namely radio-loud objects, whose radio emission, which is clearly nonthermal, appeared to extend smoothly into the IR region. In these objects the simplest interpretation is that the near IR emission is optically thin synchrotron emission from the innermost parts of a jet, while the millimeter and radio power comes from its photosphere. By analogy, also in radio quiet sources, the near IR continuum was though to be nonthermal, even if in such objects a radio spectrum extrapolated into the IR region would account for less than 0.1% of the IR power (fig. 1.1). Furthermore, the near IR continuum could be fit by a power law, which is consistent with a nonthermal emission mechanism. The alternative suggestion of thermal emission from dust heated by a primary UV radiation (Rees et al. 1969; Bollea and Cavaliere 1976), was not taken very seriously, since without the general ability to obtain measurements in the submillimeter and far IR regions, supporting evidence was not forthcoming.

Only during the first half of 1980s, the dust reemission picture began to be regarded as attractive, at least for certain classes of AGNs, as a result of a variety of near–IR observing programs of starbursts and AGNs, that were designed to investigate the structure of the continuum and the underlying physical processes (e.g. Neugebauer et al. 1979; Rieke 1978; Rieke et al. 1980; Balzano and Weedman 1981; Rieke et al. 1985). Sy 2 galaxies were found to be characterized by steeply falling near-IR continua, and Sy 1 by more moderate power law. It was therefore suggested that the spectra of Sy 2 galaxies was the result of emission from dust, in contrast to those of "true" AGNs such as Sy 1s.

Dust in star-forming regions often show some distinct spectral features in moderate resolution ($\Delta\lambda/\lambda \sim 0.1$) infrared spectra, between 8 and 13 μm, usually attributed to small ($r \leq 0.01\mu$m) silicate grains. When these features where searched

for in the brightest Sy 1 galaxies, they were found in a fraction of them (e.g. Aitken and Roche 1985). It seemed clear that at least some Sy 1 galaxies contained a significant amount of dust responsible for part of the near IR emission. On the other hand, the failure to see dust features in all objects, was generally taken as a proof that thermal dust emission is often not an important contributor to the continuum emission, even if it is quite plausible that the response of dust composition and size distribution to the environment of AGNs can led to the loss of these spectral features.

Many improvements have been made possible in the last few years, especially following the availability of far IR (IRAS) and submmillimetric data for conspicuous samples of AGNs. An important argument, favoring the dust origin of the IR emission, is the observed steep rise of the submillimetric continuum between 1000 and 100 μm (e.g. Engargiola et al. 1988; Chini et al. 1989; Lawrence et al. 1991). If this spectral region is interpreted as optically thick synchrotron emission, coming from a pure power law population of relativistic electrons, the expected slope is $f_\nu \propto \nu^{2.5}$, if the emitting medium is homogeneous, and shallower otherwise. In many sources the spectrum is definitively steeper than this. Such sources could be in principle be arranged, if one takes into account the modifications of the electron energy distribution due to self absorption (Ghisellini et al. 1988), which can produce a rise as steep as ν^3 over a decade in frequency, but only for an almost fully homogeneous and sharp edged source, a quite unrealistic case (for a more quantitative discussion see Sanders et al. 1989). By converse, a steep submillimetric rise is very natural in dust models since at this long wavelengths dust is expected to be optically thin. The absorption efficiency of the dust grains scales as ν^γ, where $0.6 < \gamma < 1.0$, and therefore the emissivity scales as $\nu^{2+\gamma} T_d$, where T_d is the temperature of the emitting gas. The only needed requirement is therefore a source with a well defined minimum dust temperature, of the order of 50 K. This does not require much contriving since even dust far away, or shielded from the central source, is kept heated to temperatures if this order by starlight.

Following these lines of argument, Barvainis (1987) substantiated previous hints of many authors in a very simple model, which naturally explains the IR continuum with the reradiation by dust, heated up to the evaporation temperature by a primary optical and ultraviolet continuum emissions. This model has been then successfully used to fit the 0.3 to 100 μm continuum of 11 sources (Barvainis 1990), see Fig. 1.9). An analogous model, in which however the dust is geometrically organized in a warped disk, has been proposed by Sanders et al. 1989. A fundamental starting point of such models is that the shape of the infrared emission cannot be reproduced by dust at a single temperature, but by dust with a range of temperatures. Indeed, it is assumed that the dust temperature is established by the balance between the

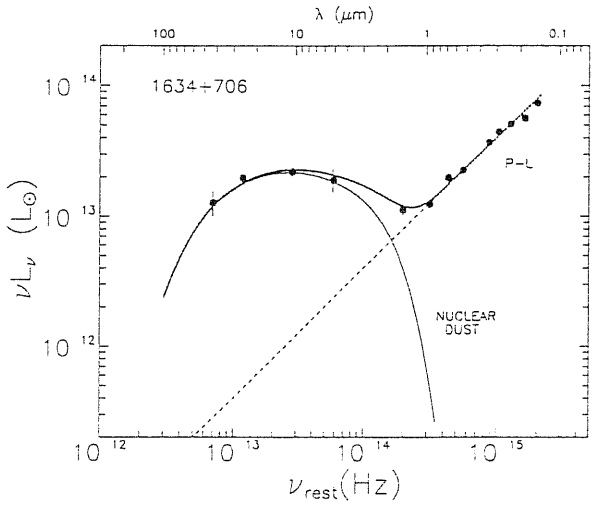

Figure 1.9: Fit to the 0.3–100 μm continuum of a quasar using an optical-UV power law plus reradiation from dust grains in the IR (from Barvainis 1990).

energy absorbed and emitted, so that a broad distribution of dust temperatures, where the hotter dust lies closer to the central radiation source is naturally achieved. The radius of the hottest infrared emitting region (1000 $\div$ 2000 K) would be $\sim$ 0.3 $\div$ 1 pc at 1 $\div$ 2 μm, while the radius of the coolest regions (30 $\div$ 60 K) would be $\sim 10^3 \div 10^4$ pc at 60 $\div$ 100 μm. A qualitative prediction of similar models is that the IR variability, should it arise, would occur on timescales increasing with the wavelength, of the order of months–years at 1–2 μm and thousands of years at 100 μm. Also the time lag with respect to the optical-UV variability should be an increasing function of the wavelength. By converse, since synchrotron models must became self absorbed at a few tens of μm, the derived source size, and therefore the expected timescales for IR variability, would be of the order of a few light hours and a few hours respectively (e.g. Lawrence et al. 1991). Available observations of IR variability confirms the predictions of dust models: in most objects the variability decreases from the optical to the near infrared regions, where the typical timescales are of the order of a few months, and is lacking in the IRAS bands at least up to scales of many months (Edelson and Malkan 1987). In addition, a study on the variability of Fairall 9 (Clavel et al. 1989) has shown that, while the optical and the J fluxes varied in the same sense and almost in phase with the UV continuum, the K and L emissions show a delay of about 400 days.

Another strong support for the dust models is the nearly universality of the local minimum in νF_ν at $\log \nu = 14.5$, that is $\lambda \sim 1 \mu$m (Fig. 1.1). This feature arises quite

naturally in models where dust reradiates a primary optical-UV thermal continuum with $T \sim 25000$ K, since dust is destroyed at temperature exceeding ~ 2000 K, and therefore around 1μm both the dust reradiation and the primary continuum are low. If instead the IR is interpreted as a nonthermal component separated from the blue bump, the universality of the minimum location requires that the nonthermal flux in all sources is the same constant fraction of the thermal blue bump luminosity, a requirement difficult to explain.

Many authors have explored the correlation between near IR and X-ray luminosities of AGNs, to probe the relevance of the non-thermal emission in the IR band. So far no definite conclusion has been reached about the true importance of this correlation (see discussion and references in Sanders et al. 1989 and in Chapter 3). However it must pointed out that its existence is not in contrast with an IR continuum dominated by thermal dust reradiation. Actually many models predict a tight connection between X-ray and UV-optical emissions of AGNs: X-ray photons can be produced by Compton upscattering of UV-optical photons by high energy electrons, or, alternatively, X-ray primary photons may be reprocessed into UV-optical photons (see e.g. Collin-Souffrin 1991). Therefore, if thermal dust emission is directly powered by the UV emission of the nucleus, a significant correlation between the IR and X-ray emissions is expected.

We can conclude that, according to many evidences collected in the last few years, in radio quiet AGNs the IR continuum seems to be thermal in origin, in contrast to what happens in blazars. Radio loud quasar can be sometimes intermediate cases where nonthermal emission can make a measurable contribution to the infrared continuum. A well known example of this is 3C 273, whose infrared variability on timescale of some days implies a component with a brightness temperature $> 10^6$ K, which most probably has a nonthermal origin. As we shall see in Chapter 3 and 5, our work further supports the thermal origin of the IR continuum for the Seyfert 1 nuclei.

Chapter 2

An Analysis Method for Seyfert Images

Summary. Our work is based on a homogeneous sample of 56 local AGNs, which is defined in this Chapter. Since we are interested in the study of the nuclear properties, as well as in the characteristic of the hosting galaxies, a precise method for separating the nuclear and galaxian fluxes is needed in the optical and near IR bands. Here it is described a procedure developed for this purpose and based on imaging data, which we have extensively applied for the analysis contained in the next two chapters.

2.1 The Sample and The Problem

Low luminosity local AGNs such as Sy 1 nuclei play an important role in the progress of our understanding of nuclear activity, because their power with respect to the host galaxy is not overwhelming, giving us the potential opportunity to better investigate the relations and interactions between the nucleus and the host. On the other hand, this same circumstance very often constitutes a problem in interpreting the data, because the contamination of nuclear observables caused by other galactic components can be very important, especially in optical and infrared bands. In the past, many efforts have been made in order to solve this problem when deriving magnitudes of the bare nucleus, usually using photometric data (Sandage 1973; Penston et al. 1974; Cheng et al. 1985; McAlary and Rieke 1988; Simons et al.

1988) but also two dimensional imaging (Yee 1983; Malkan and Filippenko 1983; Ward et al. 1987)

The methods employed with photometric data are usually based on heavy assumptions about the host galaxy and/or the nucleus. As a result, the information about the host is completely lost, and the results even for the nucleus have in general quite large (systematic) error bars, though they can still give useful informations at least for statistical purposes. On the other hand, methods based on imaging can give, if carefully implemented, much more reliable results, but they have the obvious disadvantage that they are much more time consuming and requires high quality data. As a result, this is the first time that a method of this kind is applied in the study of a large sample of Seyfert, and in particular to near-IR data. In most of the interpretative studies of the nuclear SEDs that we have mentioned in Chapter 1, the contribution to the IR and optical emission from the host galaxies is either neglected, or it enters as a free parameter in fitting the SEDs. However in this spectral region the contributions of the host galaxies are often relevant, even in the case of QSOs observed with small apertures. The determination of truly nuclear fluxes of a well defined and statistically significant sample of AGNs is of course extremely important, when discussing the possible emission mechanisms operating in the IR and optical bands.

We have concentrated ourselves on the sample of Seyfert 1 and 1.5 galaxies defined by Cheng et al. 1985 (in the following we will sometimes refer to it as "our sample"), from which they derived the luminosity function of low luminosity AGNs (see table 2.1). This optical luminosity function matches remarkably well with that of the optically selected QSOs and it also compares favorably with the local luminosity function of the X-ray selected active galactic nuclei. Moreover about 70% of the sample objects have been detected in one of the IRAS bands and the same percentage has been detected also in radio. X-ray observations allow for the computation of 2 keV fluxes for about 60% of the objects. The sample comprises 56 AGNs in the area covered by the first nine Markarian lists, with the restrictions $U \leq 16.3$, $M_u \leq -18.5$ and $z \leq 0.08$. It has been shown that there is no significant correlation of the apparent magnitudes with the absolute magnitudes, or with the ratios of the fluxes of the nuclei to those of the underlying galaxies. Following Neyman and Scott (1961, 1974) the sample is called *homogeneous* in the sense that the probability for an objects to be included depends solely on apparent magnitude.

It is therefore quite informative to investigate the IR and optical properties of this well defined sample of faint active galactic nuclei harbored in Seyfert 1 galaxies with techniques which allow a reliable separation of the emissions of the nuclei and of the galaxies.

In this chapter we describe the procedure that we have developed for deriving

the nuclear and galaxian fluxes from camera images (sec. 2.2), taking full advantages from the much greater amount of information contained in imaging data, in order to reduce to the minimum the assumptions to be made. We have applied this method to both K band IRCAM images and CCD optical images of the objects of our sample. Since the procedure is essentially the same for K band and optical images, we describe it in a common chapter. Then we will present and discuss the result obtained in the infrared (Chapter 3) and in the optical (Chapter 4). We have also collected two-aperture photometry in J, H, K and L bands of the objects of our sample, for which we have worked out methods for separating the nuclear and galactic fluxes, taking into account the results of K band images. These methods, and their results, will be described and discussed in the chapter devoted to the IR.

2.2 Analysis Procedure for Imaging Data

2.2.1 Goal

Our scope in analyzing imaging data, both optical and in the K band, is to obtain reliable determinations of nuclear fluxes and of the main characteristics of the galaxies hosting the AGNs, such as their total luminosity, the relative importance of the bulge and the disk components and the morphological parameters. Here we describe the technique that we have developed for this purpose. For the interested reader, additional details can be found in Granato 1988.

2.2.2 Model

To separate the nuclear from the galactic fluxes, a model for the profile of the host galaxies is needed. A first general assumption we make is that the host galaxies are *regular* galaxies, with bulge and disk. Of course this is an oversimplification of the real situation. In the CCD frames of our objects complex structures like rings or disturbances frequently show up. Similar features have been noticed also by other authors (Dahari, 1985; MacKenty, 1990). However it is reasonable to assume that these structures do not contribute significantly to the total luminosity of the host galaxies. Moreover, as we will see in a moment, we have adopted the procedure of averaging the surface brightness over concentric rings, and this largely smooths out irregularities and weakens their influence in the determination of the fluxes of galaxies and nuclei. The most intriguing possibility is the presence of a bar, although Kent (1985) has cast some doubt on the possibility of discriminating between the presence of a bar or of a bulge on the basis of the intensity profiles even of non active galaxies.

α (1950)	δ (1950)	Name	Type	z
00 03 45.1	19 55 27	Mkn 335	1	.025
00 48 53.0	29 07 46	0048+29	1	.036
00 50 57.8	12 25 19	IZw 1	1	.061
00 57 08.6	31 33 27	Mkn 352	1	.015
01 11 12.7	13 00 27	Mkn 975	1	.050
01 19 26.5	-01 18 05	II Zw 1	1	.054
01 24 50.1	18 55 07	Mkn 359	1	.017
01 57 51.1	02 25 49	Mkn 584	1	.078
02 12 00.5	00 59 57	Mkn 590	1.5	.027
02 38 55.8	06 58 27	Mkn 595	1	.028
04 33 59.7	-10 28 40	Mkn 618	1	.034
06 45 43.4	74 29 07	Mkn 6	1.5	.018
06 55 33.9	54 15 53	Mkn 374	1	.044
07 10 35.8	45 47 07	Mkn 376	1	.056
07 32 42.0	58 53 00	Mkn 9	1	.040
07 38 46.9	49 55 47	Mkn 79	1.5	.022
07 43 07.4	61 03 23	Mkn 10	1	.029
07 52 03.2	39 19 07	Mkn 382	1	.034
09 15 39.5	16 30 59	Mkn 704	1.5	.029
09 21 44.4	52 30 14	Mkn 110	1	.036
09 23 20.0	12 57 03	Mkn 705	1	.028
09 45 24.3	50 43 26	Mkn 124	1	.057
10 15 38.7	64 13 14	Mkn 141	1	.039
10 22 23.1	51 55 40	Mkn 142	1	.045
10 55 20.6	20 45 03	Mkn 634	1	.066
10 59 21.0	10 33 48	Tol 1059+105	1	.034
11 03 23.0	72 50 24	NGC 3516	1	.009
11 19 10.9	12 00 47	Mkn 734	1	.050
11 33 48.0	21 52 00	Mkn 739E	1	.030
12 15 55.5	30 05 27	Mkn 766	1	.013
12 19 31.8	75 35 10	Mkn 205	1	.070
12 29 33.1	20 26 03	Mkn 771	1	.064
12 58 18.0	61 55 27	Mkn 236	1	.052
13 00 30.4	16 40 34	Mkn 783	1	.067
13 51 51.9	69 33 13	Mkn 279	1.5	.031
13 53 45.1	38 48 54	Mkn 464	1	.051
14 15 42.0	25 22 00	NGC 5548	1.5	.019
14 34 58.0	59 00 40	Mkn 817	1.5	.032
14 40 04.6	35 38 53	Mkn 478	1	.079
15 01 36.4	10 37 59	Mkn 841	1.5	.036
15 06 12.5	51 38 41	Mkn 845	1	.046
15 28 51.0	07 37 38	NGC 5940	1	.034
15 34 45.4	58 04 00	Mkn 290	1	.031
15 35 21.5	54 43 04	Mkn 486	1	.039
15 57 16.6	35 10 13	Mkn 493	1	.031
16 06 15.6	12 27 41	Mkn 871	1	.034
16 29 43.1	67 29 06	Mkn 885	1	.025
16 59 10.4	29 28 47	Mkn 504	1	.036
17 20 45.6	30 55 30	Mkn 506	1.5	.043
20 41 26.4	-10 54 16	Mkn 509	1	.036
21 30 01.3	09 54 59	II Zw 136	1	.062
22 14 45.2	13 59 27	Mkn 304	1	.039
22 37 47.0	07 47 33	2237+07	1	.025
23 00 44.0	08 36 18	NGC 7469	1.5	.017
23 16 22.7	00 01 48	Mkn 530	1	.029
23 59 52.9	03 04 26	Mkn 543	1	.026

Table 2.1: The homogeneous sample defined by Cheng et al. 1985.

A second assumption is that the thickness of the galaxies is negligible and that the surface brightness is symmetric with respect to the central axis perpendicular to the galactic plane. This is equivalent to assume that the isophotes are concentric circles on the galactic plane. The isophotes of a galaxy whose fundamental plane is tilted by an angle i with respect to the line of sight become concentric ellipses with axial ratio $\epsilon = b/a = sin\ i$. Therefore by measuring the isophotal axial ratio we can estimate the galaxy inclination on the plane of the sky.

We have represented the intrinsic intensity profile of the host galaxies as the sum a bulge following the $r^{1/4}$ law and an exponential disk:

$$I_b(r) = I_e \exp\left[-3.33\left(\left(\frac{r}{r_e}\right)^{1/4} - 1\right)\right] \tag{2.1}$$

$$I_D(r) = I_D \exp\left(-\frac{r}{r_D}\right) \tag{2.2}$$

where r_e is the effective radius, which encloses half of the total light of the bulge, I_e is the surface brightness at r_e, r_D is the scale length of the disk, and I_D its central surface brightness. By adding up a nuclear pointlike component we get a model for Seyfert galaxies.

Therefore the brightness distribution on the plane of the sky has been modelled as the sum of three components: (i) a point like nucleus, (ii) a $r^{1/4}$ bulge and (iii) an exponential disk. We have taken into account the effects of the PSF (atmospheric seeing plus instrumental effects) and of the galaxy inclination on each component. In order to choose a proper functional form for the PSF, we considered, under many different seeing conditions, the CCD profiles of some stars, having magnitude comparable to those of typical nuclei of our sample. We found, inspired by Capaccioli and De Vaucouleurs (1983), that the best representation for our purposes is given by the sum of two gaussians:

$$I(r) = \frac{F_T}{2\pi\sigma^2(1+as^2)}\left[\exp\left(\frac{-r^2}{2\sigma^2}\right) + a\exp\left(\frac{-r^2}{2s^2\sigma^2}\right)\right] \tag{2.3}$$

where F_T is the total flux of the star, σ is the s.d. of the main gaussian and a and s are the ratios of the central peaks and of the standard deviations of the two gaussians respectively. While σ is of course a variable parameter depending on the seeing conditions, we have found that a and s can be considered as constants, fixed to the values of 0.05 and 2.2 respectively. The only adjustable seeing parameter is therefore σ, which, when possible, was determined for each frame by considering the profiles of two of three field stars in the same frame. While in CCD images this was almost always possible, IRCAM frames are usually too small to include field stars,

and therefore for infrared frames we used images of standard stars taken during the same night, and as close in time as possible.

The seeing profile of the nucleus is then given by eq. 2.3, where F_T must be replaced by F_n, the total flux of the nucleus. For the hosting galaxy, it is much more complex to take into account the effects of seeing and of inclination of the galaxian planes with respect to the line of sight. Using the PSF given by eq. 2.3 and introducing a cartesian reference frame with x axis defined by the intersection of the plane of the sky with that of the galaxy, z axis directed along the line of sight and y axis in the plane of the sky, it can be shown (see Granato 1988) that the expected surface brightness of a hosting galaxy at a point (x, y) in the sky is given by

$$I_{obs}(x,y) = \frac{1}{2\pi\sigma^2(1+as^2)\epsilon} \times \tag{2.4}$$

$$\times \int\int_{-\infty}^{\infty} I(r') \left[exp\left(-\frac{\rho'^2}{2\sigma^2}\right) + a\ exp\left(-\frac{\rho'^2}{2s^2\sigma^2}\right)\right] dx'dy' \tag{2.5}$$

where $\rho'^2 = (x-x')^2 + (y-y')^2$, and $r' = \left(x'^2 + \frac{y'^2}{\epsilon^2}\right)^{1/2}$.

Thus the model depends on a total of five parameters to be determined by matching it to the observed images: the total flux of the nucleus F_n, the effective radius r_e which encloses half of the total light of the bulge, the surface brightness I_e at r_e, and the two parameters modelling the disk, namely the scale length r_D and the central surface brightness I_D. The two additional parameters σ and i are instead independently determined as described above.

2.2.3 Fitting Procedure

Since we have assumed an axially symmetric model, it is useless (and rather impractical) to fit it directly to two dimensional images. Thus, before performing the fit, we reduced the observed images to intensity profiles properly averaging the surface brightness in annular concentric rings, with the aim of increasing the signal to noise ratio in the outer regions and to smooth out the small scale irregularities. In such a way we reduce the dimensionality of the problem, significantly decreasing the required computing time, but we do this without squandering the bidimensional information, at least for the purposes of fitting it to our intrinsically unidimensional model.

To determine the background level, we have usually chosen 4 boxes of at least 20 pixels in regions of the frames free from contaminations by the galaxy or other field objects. The error bars associated to the points of the profile are comprehensive of photon noise of the source, of the uncertainty in the background subtraction, and

of the read-out noise of the detectors:

$$\frac{\sigma^2_{<I>}}{< I >^2_{ring}} = \frac{\sigma_f^2}{f^2} + \frac{\bar{n}_e + \sigma^2_{ron}}{N_{ring}\left(\bar{n}_e - \bar{n}_{bk}\right)^2} + \frac{\bar{n}_{bk} + \sigma^2_{ron}}{N_{bk}\left(\bar{n}_e - \bar{n}_{bk}\right)^2} + \frac{\sigma^2_{bk}}{\left(\bar{n}_e - \bar{n}_{bk}\right)^2} \tag{2.6}$$

where $f \pm \sigma_f$ is the multiplicative constant needed to convert from electronic counts to fluxes, N_{ring} and N_{bk} are the number of pixel in the ring and in the region used for the background determination respectively, $\bar{n}_e$ is the mean number of electrons counted in the pixels of the ring, $\bar{n}_{bk}$ is the mean number of electrons per pixel due to the background and σ_{ron} is the read-out noise.

The center of the galaxy is determined by the use of the first moment of the brightness distribution on a 20x20 pixels region around the brightest one. The concentric annular rings are spaced by 1 pixel. The brightness in a ring is the sum of the contributions by the individual pixels weighted by the area in common between the ring and the pixels. This procedure is extremely relevant in the central regions of the objects, where the pixel size is comparable to the scale of a significant variation of the intensity profile. The binned nature of the images is quite relevant in the central pixels of the frames. Thus when fitting the model to the observed profile, in the central 20x20 pixels we computed the flux expected from the model in each pixel, taking into account the offset of the center of the observed image, as determined from the first moment of the brightness distribution, with respect to the center of the central pixel. Then we constructed the model intensity profiles averaged over concentric rings with the same technique used for the real data and described above. In more external regions, the model intensity profile can be instead directly averaged over circular rings.

In spite of the simplification introduced by the circular averaging, the computing time needed to take into account everywhere for the seeing effect would still be huge for fitting purposes, since the computation of the model flux in each ring implies an integration of eq. 2.5 over the ring, and therefore a 4–dimensional numerical integral. But the relevance of the convolutory effect strongly decreases in regions with relatively shallow gradient of the surface brightness. We have checked that with our typical observational conditions, the seeing effect on the galactic component is negligible at distances from the centre $r \geq 8\sigma$. Exterior to this radius we have neglected the seeing convolution, and this greatly simplifies the numerical task of computing the total model flux in a ring: in this case we have a bidimensional integral, but since the radial part becomes analytical, we are left simply with a numerical integration in one variable. For the flux of the disk and of the bulge in a ring between ρ_1 and ρ_2 and ignoring the PSF we have therefore:

$$F_D(\rho_1,\rho_2) = \frac{4I_D}{\epsilon} r_D^2 \int_0^{\pi/2} \frac{\beta(\phi)}{\alpha(\phi)}\, d\phi \tag{2.7}$$

$$F_b(\rho_1,\rho_2) = \frac{16 I_b r_b^2 \exp b}{\epsilon} \int_0^{\pi/2} \exp(kx)\gamma(\phi)\, d\phi \tag{2.8}$$

where

$$\alpha(\phi) = \left[\cos^2\phi + \frac{\sin^2\phi}{\epsilon^2}\right]^{1/2} \tag{2.9}$$

$$\beta(\phi) = \exp\left[-\frac{\alpha(\phi)}{r_D}\rho_2\right]\left[-\frac{\alpha(\phi)}{r_D}\rho_2 - 1\right] - \exp\left[-\frac{\alpha(\phi)}{r_D}\rho_1\right]\left[-\frac{\alpha(\phi)}{r_D}\rho_1 - 1\right] \tag{2.10}$$

$$k = k(\phi) = -b\,(\alpha(\phi))^{1/4} \qquad x = \left(\frac{\rho}{r_b}\right)^{1/4} \qquad b = 3.33 \ln 10 \tag{2.11}$$

As for the inner regions, we computed the surface brightness in 100 points of the quadrant, distributed in appropriate way, and used this 10 by 10 array in the x–y plane to interpolate the values required to calculate the intensity profile of the galaxy. Finally the nuclear and galaxian profiles are added together to obtain the expected global intensity profile.

The best fit parameters have been obtained by χ^2 minimizations, using the routine MRQMIN described in Press et al. 1986, with a typical computing time of about half an hour per fit on a VAX 8530. The initial values of the parameters have been selected using tentative fits by eye. The problem of the uniqueness of fitting solution is addressed in Chapter 4.

Chapter 3

Discussion of the Near-IR Data

Summary. We present and analyze IR observations of the homogeneous sample of Seyfert 1 galaxies defined in the previous chapter, that we also observed with CCDs in optical bands (chapter 4). For 41 objects we have got K band frames and photoelectric photometry in J, H, K and L with the UK Infrared Telescope. The methods of separating the galaxian and nuclear fluxes are presented and discussed. The nuclear and galaxian K magnitudes are derived with their errors. The K band luminosity distribution of the galaxies hosting the active nuclei have been derived and the comparison with the local luminosity function of the spirals leads to the conclusion that the probability of a spiral galaxy hosting bright AGN increases with the luminosity. The colors of the galaxies are similar to those of spirals with moderately enhanced star formation rates. The analysis of the correlation of the K band to the IRAS fluxes demonstrates that the nuclei largely dominate the 12 μm emissions, whereas the galaxies are the major contributors at $\lambda \geq 60\mu$m. It is also shown that galaxies with slope between 12 and 60 μm flatter than -1.5 are likely hosting an active nucleus. The IR spectral data of the nuclei as well as the correlation of the X-ray to the IR emissions are briefly discussed. The conclusion is that the IR emission of the nuclei are probably dominated at $\lambda \geq 2.2\mu$m by thermal dust radiation.

3.1 Introduction

In the last few years the astronomical detectors in the near IR bands have been remarkably improving both in sensitivity as well in spatial resolution, approaching the performances of the optical CCDs. As for the studies of AGNs, these improvements allow for much better measurements of the IR nuclear fluxes after reliable subtraction of the galaxy contributions. Nevertheless, as we have seen in chapter 1, the origin of the IR emission of the AGNs is still debated. In particular the importance of the thermal dust reradiation is still an open question.

In many studies the contribution to the IR emission from the host galaxies is either neglected, or it enters as a free parameter in fitting the SEDs. However in the IR band the contributions of the host galaxies are often relevant, even in the case of QSOs observed with small apertures. The determination of truly nuclear fluxes of a well defined and statistically significant sample of AGNs is extremely important, when discussing the possible emission mechanisms operating in the IR bands.

It is therefore quite informative to investigate the IR properties of our sample of faint active galactic nuclei harbored in Seyfert 1 galaxies with techniques which allow a reliable separation of the emissions of the nuclei and of the galaxies.

In this chapter we will present the observations obtained with the UK Infrared Telescope (UKIRT) using both photoelectric photometer and imaging camera. We present the observational data in Section 3.2; Section 3.3 is devoted to data analysis; in Section 3.4 the results are discussed and the conclusions are summarized in Section 3.5. The material presented in this chapter constitutes the body of two papers already submitted for pubblication (Zitelli et al. 1991; Danese et al. 1991).

3.2 Observations

We observed 45 objects with the photoelectric photometer and/or with the IR camera on the 3.8 m UK Infrared Telescope at Mauna Kea. One of these (Tol 1059+105), however, does not belong to the homogeneous sample defined in chapter 2. The images of two objects (Mkn 124 and Mkn 595) could not be calibrated because of lack of photometric data. In the following analysis, we will deal with the remaining 41 objects, for all of which we got a K-band image.

3.2.1 IR photometry

Our photoelectric data were obtained using the photometers UKT9 in two nights in April and UKT6 in two nights in August 1987. In order to avoid contributions from the galaxy to the sky-observation we used a focal-plane chopper giving a beam

throw of 40 arcsec in R.A. We observed the objects in the J H K L' bands using 5″ and 7.8″ apertures in order to minimize the contamination of the nuclear radiation by the underlying galaxies. Each observation was stopped at values of S/N ratio of about 20–25. The observed standards were selected from the available lists defined on the UKIRT system. The photoelectric data were reduced in Edinburgh using the local facilities.

We observed 27 objects from the sample of Cheng et al. (1985), plus Tol 1059+105. For all but one of them (Mkn 142), we have got also K band image (Section 3.2.2).

The data, corrected for galactic extinction, using the values of $E(B-V)$ listed by Cheng et al. (1985), are reported in Table 3.1. We have obtained JHKL photometry within at least one aperture for all objects except Mkn 486 which is lacking only L-band observations; 15 galaxies were observed with two apertures at least in JHK bands, and 11 of them also in the L band; one galaxy has two-aperture photometry in J and K bands; 8 galaxies only in the K band. Typical internal photometric errors are about 0.03 magnitudes in each band. We have used the absolute calibrations proposed by Campins et al. (1985) and have reduced other authors' data to the same system whenever possible.

One object (Mkn 478) has been observed twice in different nights; the results showed typical differences of 0.1 mag (i.e. about 10% in fluxes). This may be indicative of the true uncertainty, which is expected to be significantly larger than the internal error quoted above because of seeing fluctuations, uncertainties in the telescope pointing, which affect the observations with small apertures, and focus variations (see e.g. McAlary et al. 1983).

The comparison with other authors' data is hampered not only by the variations of the seeing conditions, but also by the use of different photometric systems, and by the fact that the apertures are different. Moreover the time variability of the nuclei may affect the conclusions. Of course a detailed comparison would involve the standards of the calibration, which often are different from author to author and often are not mentioned in the papers. However the discrepancies generated by the use of different standards are of the order of few percent. More sensitive is the conversion of magnitudes to fluxes, or viceversa. In this case discrepancies of about 10% may be found. When dealing with observations performed with different apertures, we took into account the host galaxy contribution, by the use of the mean growth curves for early type spirals proposed by Griersmith et al. (1982). The corrections amount to few hundredths of magnitude, if we limit the comparison to data taken with small apertures.

We have found in the literature JHK photometry with apertures ranging from 7.5″ to 9″ for of 10 of our objects. The average magnitude difference in the K band is $\Delta K = 0.03 \pm 0.13$ (s.d.) and similar values are obtained for ΔJ and ΔH.

Name	z	E_{B-V}	J(5″)	H(5″)	K(5″)	L(5″)	J(7.8″)	H(7.8″)	K(7.8″)	L(7.8″)	Date (87)
0048+29	.036	.00	12.99	12.16	11.61	10.90	12.74	11.98	11.48	10.70	Aug 16
2237+07	.025	.00	13.05	12.12	11.44	10.35	12.70	11.91	11.32	10.24	Aug 16
II Zw 1	.054	.01	14.25	13.45	12.69	11.34	13.85	13.05	12.40	11.09	Aug 16
II Zw 136	.062	.03	13.38	12.42	11.27	9.57	13.22	12.25	11.14	9.34	Aug 15
Mkn 9	.040	.03	12.95	12.00	10.86	8.77	12.87	11.93	10.81	...	Apr 5
Mkn 110	.036	.01	13.67	13.02	11.93	10.10	13.48	12.68	11.72	9.97	Apr 4
Mkn 142	.045	.00	14.16	13.31	12.49	11.39	...	...	...	...	Apr 5
Mkn 290	.031	.01	13.26	12.56	11.76	10.04	13.16	12.45	11.62	...	Apr 4
Mkn 304	.067	.05	13.39	12.60	11.68	10.09	13.20	12.42	11.55	10.11	Aug 16
Mkn 374	.044	.08	13.31	12.61	11.94	10.44	...	...	...	...	Apr 5
Mkn 376	.056	.09	12.84	11.95	10.76	8.85	...	...	10.76	...	Apr 5
Mkn 382	.034	.04	13.85	13.29	12.77	11.91	13.81	13.11	12.65	11.64	Apr 4
Mkn 464	.051	.00	14.31	13.65	12.94	11.12	...	13.59	12.69	...	Apr 4
Mkn 478	.079	.00	12.84	11.90	10.88	9.37	...	...	10.94	...	Apr 5
Mkn 478	.079	.00	12.93	12.05	10.98	9.42	...	...	10.93	...	Apr 4
Mkn 486	.039	.01	13.05	12.25	11.16	...	...	...	...	...	Apr 4
Mkn 506	.043	.03	13.58	12.71	11.97	10.52	13.26	12.44	11.79	10.52	Aug 15
Mkn 509	.036	.04	12.03	11.15	10.20	8.58	11.89	11.05	10.14	8.52	Aug 15
Mkn 530	.029	.03	12.46	11.61	10.89	9.35	12.12	11.29	10.63	9.29	Aug 15
Mkn 584	.078	.00	...	...	...	...	13.92	13.19	12.60	12.33	Aug 16
Mkn 634	.066	.00	14.30	13.37	12.65	11.35	...	...	12.55	...	Apr 5
Mkn 704	.029	.01	12.95	12.10	10.91	8.91	12.68	11.80	10.76	...	Apr 4
Mkn 705	.028	.01	12.77	11.95	11.23	9.84	...	...	11.15	...	Apr 5
Mkn 739	.030	.00	13.46	12.41	11.38	...	12.88	12.02	11.13	9.52	Apr 4
Mkn 783	.067	.01	...	...	13.68	...	14.73	14.04	13.40	13.04	Apr 4
Mkn 845	.046	.01	13.59	12.87	12.38	11.49	...	...	12.01	...	Apr 5
Mkn 975	.050	.04	13.38	12.33	11.34	9.54	13.07	12.12	11.20	9.56	Aug 15
NGC 5940	.034	.00	13.44	12.66	11.88	10.65	...	...	11.75	...	Apr 5
Tol 1059+105	.034	.00	14.50	13.84	13.39	12.18	...	...	13.19	...	Apr 5

Table 3.1: Our new photometric data.

A more direct comparison is possible for 4 object which are in common with the sample of PG QSOs observed by Neugebauer et al. (1987) in the near IR with a 5.5″ aperture. Again, the rms difference is $\Delta m \simeq 0.15$.

We conclude that a conservative estimate of the uncertainty of our photometric data is $\simeq$ 0.1–0.15 mag; this estimate may really be an upper limit in the present of a significant variability.

3.2.2 K-band imaging with IRCAM

As already mentioned, high resolution K band images have been obtained on January and on July 1988 with the IRCAM system (McLean et al. 1986) for 43 galaxies from the Cheng et al. (1985) sample; two of them, however, could not be calibrated and will not be considered further. We selected the high resolution mode with a scale of 0.62″/pixel, to obtain detailed maps of the innermost regions. This choice has the drawback that the images of the nearest objects extend over a large fraction of the available pixels (62x58), complicating the background subtraction, which is particularly subject to errors in the outer regions.

The data on individual pixels have been reduced to intensity profiles as described in chapter 2. We stated there that to determine the background level, we usually chose 4 boxes of at least 20 pixels each in regions away from the galaxy, but possibly not just in the outermost areas of the detector. However this prescription is not easy to fulfill in our IR frames. This difficulty entails large uncertainties in the profiles at radii larger than 10″, where the surface brightness usually drops down to less than 1% of the central value. The errors quoted in Table 2 are comprehensive of the photon noise, of the uncertainty in the background subtraction, and of the read-out noise of the detectors.

In figure 3.1 we have reported some examples of the surface brightness intensity profiles with the computed errors. It is apparent that the seeing is a major problem in our observations. In fact, despite of the widely recognized good atmospheric seeing on Mauna Kea, the average *total* seeing during our observations was about 1.6″ (FWHM) mainly due to the optical alignment of the telescope at the time of the observations.

3.3 Data Analysis

Our primary aim in analizing the K-band imaging data is to obtain reliable nuclear fluxes. Secondarily we are interested in the main characteristics of the galaxies hosting the AGNs, such as their total luminosity, and, possibly, the relative importance of the bulge and the disk components. The analysis of the photometric data is aimed

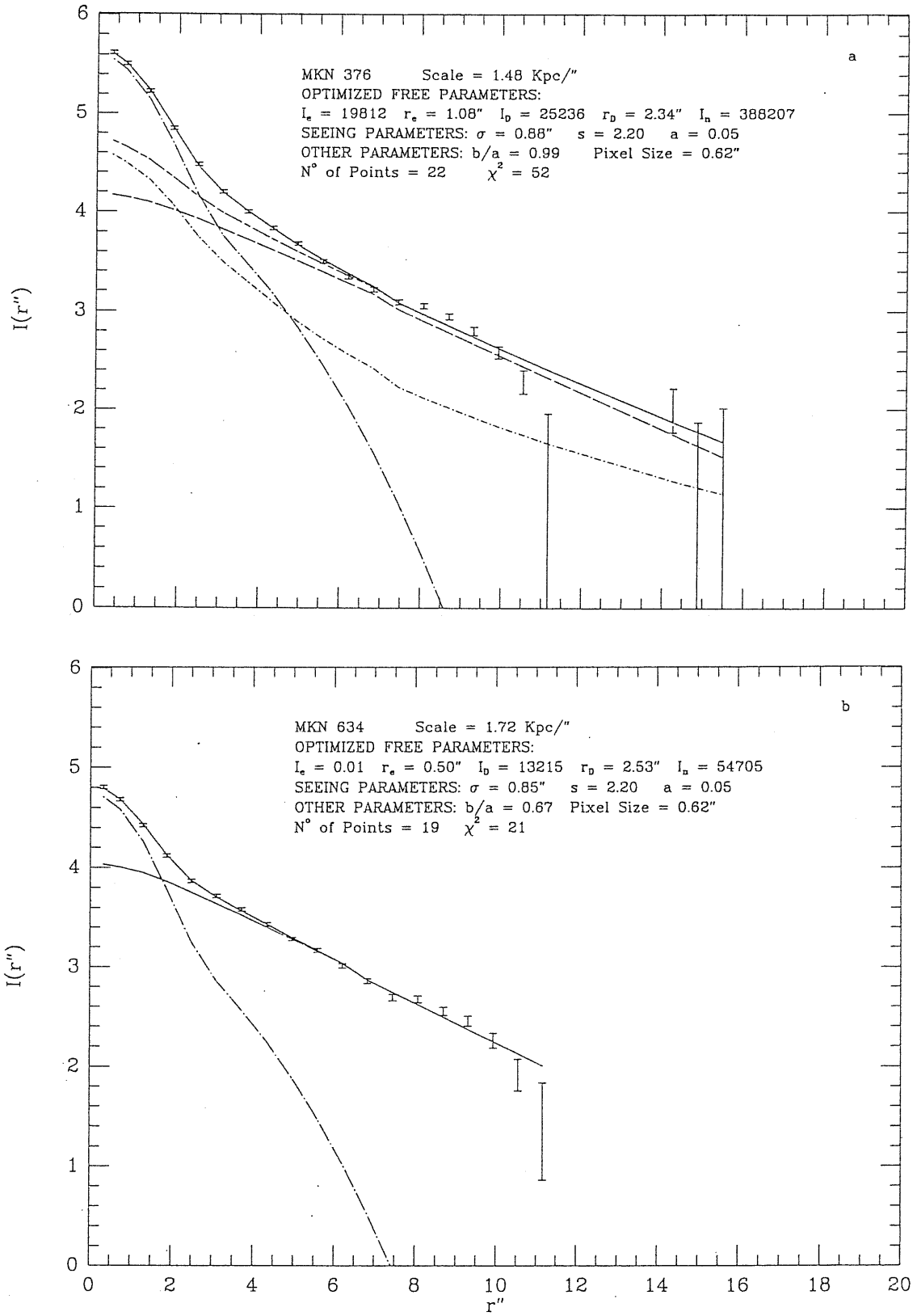

Figure 3.1: Intensity profile data (arbitrary units) and fits for two objects. The relevant parameters are shown in the panels. The global best fits (solid lines), the nuclear (dotted long dashed), the bulge (dotted dashed), and disc profiles (dashed) are reported.

at determining the main characteristics of the nuclei and of the underlying galaxies in the J, H and L bands, using the K band as pivotal.

3.3.1 Analysis of the Imaging Data

To separate the nuclear from the galactic fluxes we used the procedure depicted in chapter 2. Here we add some considerations specific to our IR data. In Table 3.2 we have reported for each observed object the best fit values of the parameters, the seeing during the observing time and the axial ratio b/a.

To accurately determine the luminosities of the nuclei and of the galactic bulges it is essential to have a good seeing and a good sampling of the PSF. A reliable determination of the background is necessary to derive the disc parameters. These conditions are not all always fulfilled by our data. When the intensity profile at small radii is strongly dominated by the PSF of the nucleus, we usually can get a good determination of the nuclear flux, but the information on the bulge is poor. For these reasons the values of the galactic parameters reported in Table 3.2 must be considered with some caution. In particular in the K band the disc profiles look steeper than in B band; the disc central brightness I_D is on average brighter than the corresponding value in B band (Chapter 4), adopting (B-K)=4.2 (Griersmith et al. 1982), whereas the disc scale is on average larger in B. The effect is likely connected to an overestimate of the background, whose evaluation is hampered by the small extent of the K frames. Moreover the formal uncertainties of best fit parameters of the galaxies are often large. However it is worth to notice that the correlations among the disc and bulge parameters are such that the total magnitudes are estimated more precisely than the individual parameters (Malkan 1984; Kent 1985; Veron-Cetty and Woltjer 1990).

All in all, the uncertainties in the estimated nuclear fluxes derived from the fits range from 2 to 40%, apart from 2 objects (MKN 504 and MKN 584) for which uncertainties amount to a factor of 1.8 and of 1.9, respectively. The estimated errors on nuclear fluxes listed in the third column of Tables 3.3 and 3.4 include, added in quadrature, the calibration uncertainties.

In these tables we have also reported the magnitudes of the host galaxies. They have been computed by integrating the intensity profiles of bulge and disc, as they resulted from the best fitting procedure, within $r \leq 60$ kpc. For each objects we have also computed the total galactic magnitudes. The differences between the two computations are usually less than 0.1. The values of galactic magnitude for 6 objects have not been reported in the tables, which showed discrepancies larger than 0.1 magnitudes. In the cases of MKN 110, MKN 376 and MKN 464 the differences stem from the fact that the best fit values of the disc scale length r_D is very large,

Name	z	E_{B-V}	b/a	σ sec	μ_e $\frac{mag}{sec^2}$	r_e kpc	μ_D $\frac{mag}{sec^2}$	r_D kpc	μ_n $\frac{mag}{sec^2}$	Date 1988
0048+29	.036	.00	.80	.93	17.90	3.33	16.79	2.68	14.09	Jul 1
2237+07	.025	.00	.90	.72	18.84	3.65	16.58	2.24	13.27	Jul 2
I Zw 1	.061	.03	.88	.65	16.82	4.83	16.91	3.18	11.35	Jul 1
II Zw 1	.054	.01	.67	.60	17.19	1.99	17.50	6.35	14.88	Jul 3
II Zw 136	.062	.03	.50	.63	19.40	7.13	16.44	3.40	12.55	Jul 1
Mkn 009	.040	.03	.90	.93	...	...	15.82	3.42	13.00	Jan 27
Mkn 079	.022	.06	.57	.95	17.75	2.41	18.24	6.27	13.23	Jan 27
Mkn 110	.036	.01	.83	.85	17.75	2.39	18.98	27.06	14.17	Jan 27
Mkn 290	.031	.01	.99	.65	16.25	.89	17.95	4.98	13.35	Jul 3
Mkn 304	.067	.05	.95	.80	17.12	3.15	17.81	5.93	13.55	Jul 1
Mkn 335	.025	.03	.90	.75	13.56	.35	16.36	2.31	11.54	Jul 1
Mkn 352	.025	.03	.65	.66	17.70	.67	16.99	1.65	13.64	Jul 3
Mkn 359	.017	.01	.68	.65	17.20	1.35	16.41	2.03	13.53	Jul 3
Mkn 374	.044	.08	.64	.95	23.56	.60	16.16	4.07	14.34	Jan 27
Mkn 376	.056	.09	.99	.88	15.97	1.60	15.70	3.46	12.74	Jan 27
Mkn 382	.034	.04	.86	.97	...	...	16.63	2.16	15.16	Jan 27
Mkn 464	.051	.00	.79	.60	17.01	1.32	21.26	19.44	14.49	Jul 3
Mkn 478	.079	.00	.85	.68	16.52	3.58	17.86	6.17	12.40	Jul 1
Mkn 486	.039	.01	.63	.60	20.64	9.93	13.75	.53	12.46	Jul 3
Mkn 493	.031	.00	.83	.60	16.98	1.83	18.23	5.53	13.69	Jul 2
Mkn 504	.036	.03	.44	.60	17.99	2.64	18.46	5.64	15.28	Jul 3
Mkn 506	.043	.03	.95	.62	17.19	2.04	17.25	8.57	13.56	Jul 2
Mkn 509	.036	.04	.85	.78	16.15	1.96	17.40	11.69	12.08	Jul 1
Mkn 530	.029	.03	.80	.85	15.59	1.34	15.57	2.91	13.77	Jul 1
Mkn 584	.078	.00	.80	.60	16.66	1.73	16.80	6.61	15.76	Jul 3
Mkn 618	.034	.05	.60	1.00	19.93	1.50	17.15	5.35	13.69	Jan 27
Mkn 634	.066	.00	.67	.85	...	...	16.54	4.35	14.99	Jan 27
Mkn 704	.029	.01	.57	.90	19.16	2.86	16.48	2.77	13.02	Jan 27
Mkn 705	.028	.01	.74	.85	24.93	78	15.00	1.31	13.34	Jan 27
Mkn 734	.050	.01	.80	.85	26.78	99.80	15.88	2.62	13.77	Jan 27
Mkn 739	.030	.00	.58	.90	...	...	15.83	3.61	13.76	Jan 27
Mkn 766	.013	.01	.80	.70	17.67	1.26	15.42	1.12	12.66	Jul 1
Mkn 771	.064	.02	.70	.80	16.77	3.82	18.34	6.76	14.40	Jul 1
Mkn 783	.067	.01	.75	.65	20.53	5.41	16.51	1.62	15.27	Jul 2
Mkn 817	.032	.01	.80	.60	13.04	.44	16.16	4.10	12.18	Jul 3
Mkn 841	.036	.00	.95	.64	18.24	5.86	14.43	.49	12.71	Jul 2
Mkn 845	.046	.01	.14	.65	20.33	3.17	16.85	6.30	14.71	Jul 2
Mkn 871	.034	.03	.57	.68	15.09	.74	16.14	4.00	13.80	Jul 1
Mkn 975	.050	.04	.61	.67	17.72	3.06	17.40	6.56	12.92	Jul 3
NGC 5548	.019	.00	.90	.65	16.12	.97	15.28	1.89	11.82	Jul 3
NGC 5940	.034	.00	1.00	.68	20.94	36.93	17.42	2.46	13.68	Jul 3

Table 3.2: Fitting parameters for brightness profiles.

Name	K_n	δK_n	$(J-K)_n$	$(H-K)_n$	$(K-L)_n$	K_g	δK_g	$(J-K)_g$	$(H-K)_g$	$(K-L)_g$	C1[a]	Ref[b]
0048+29	12.07	.22	1.94	.63	.44	11.42	.24	.85	.43	1.02	a	1
2237+07	11.80	.17	2.89	.99	1.14	11.25	.21	.59	.20	.99	a	1
II Zw 1	13.74	.28	2.76	1.83	1.58	11.85	.30	1.21	.42	1.20	a	1
II Zw 136	11.38	.17	2.22	1.30	1.35	12.08	.19	1.76	.71	2.58	a	1
Mkn 9	11.00	.15	2.29	1.28	2.19	11.33	.16	1.39	.58	...	a	1
Mkn 110	12.35	.19	1.63	1.97	2.11*	...	...	...	...	...	a	1
Mkn 290	12.04	.25	1.36	.67	1.98*	11.64	.32	1.87	1.13	...	a	1
Mkn 304	11.86	.19	1.96	1.16	1.80*	11.97	.20	1.32	.52	...	a	1
Mkn 382	13.07	.25	.82	.81	.02	12.80	.25	2.44	.05	1.78	a	1
Mkn 506	12.42	.24	2.71	1.27	2.00	10.69	.49	.94	.28	-1.23	a	1
Mkn 509	10.45	.17	2.27	1.09	1.65	9.74	.75	1.08	.61	1.54	a	1
Mkn 530	11.94	.31	2.80	1.39	2.53	10.15	.32	1.25	.48	-.20	a	1
Mkn 704	11.07	.17	2.29	1.49	2.07*	11.49	.19	1.27	.31	...	a	1
Mkn 739	11.81	.19	3.85	1.50	2.04*	11.64	.29	1.04	.47	...	a	1
Mkn 975	11.61	.22	2.70	1.16	2.02*	11.43	.28	1.17	.62	...	a	1
Mkn 335	9.98	.26	2.15	.80	...	10.96	.26	2.15	...	...	b	8
Mkn 359	12.28	.19	3.10	.62	1.47	10.67	.23	.98	.51	.94	b	11
Mkn 766	11.26	.16	.94	...	...	10.52	.18	3.36	...	...	b	5,6
Mkn 841	11.50	.18	2.11	1.13	...	10.94	.31	1.21	.72	...	b	6,12
Mkn 845	13.46	.38	1.59	.23	1.05*	11.29	.43	1.06	.65	...	b	1,6
NGC 5548	10.58	.18	1.17	.42	...	10.13	.19	2.54	1.57	...	b	5,9

[a] C1 describes the data used in deriving the nuclear magnitudes: (a) Our photometry within two apertures (5″ and 7.8″) in all the four bands plus frame K; (b) Photometry within two apertures in all the four bands, but taken in part from the literature, plus frame K; (c) Photometry (taken in part from the literature) within only one aperture, plus frame K; (d) Photometry from the literature;

[b] References for the photometry: (1) Our data; (2) Stein and Weedman 1976; (3) Rieke 1978; (4) McAlary et al. 1979; (5) Balzano and Weedman 1981; (6) Rudy et al. 1982b (AJ); (7) Ward et al. 1982; (8) Rudy et al. 1982a (ApJ); (9) McAlary et al. 1983; (10) Worral et al. 1984; (11) Lawrence et al. 1985; (12) Neugebauer et al. 1985; (13) Ward et al. 1987;

* $(K-L)_n$ derived assuming the colour of the host galaxy $(K-L)_g$=0.8.

Table 3.3: Resulting magnitudes and colors of the nuclear and galactic components. For the objects listed in this table, it has been possible to derive the colors also for the galactic component (see text and also the next table).

probably because of underestimation of the background in the respective frames. In other 3 cases (MKN 705, Mkn 734 and NGC 5940) the best fits require extreme values of the effective radius r_e. The uncertainties of the galactic magnitudes are difficult to evaluate. As a first step we have computed the difference between the galactic flux within the last observed point of the profile and the total galactic flux. This quantity is assumed to be a generous evaluation of the uncertainty of the galactic flux from the outer regions. Then we added it in quadrature to the total error on the nuclear flux (column 3 of Tables). The resulting errors expressed in magnitudes have been reported besides of galactic magnitude.

Using the K band frames we have determined the ratios between the nuclear flux F_{Kn} and the galactic flux F_{Kg} within the 5″ and 7.8″ apertures of the photometric observations. The ratios in the 5″ aperture range from .5 to 7.2 with a median value of 2.1; thus, neglecting the galaxy contribution within this small aperture would lead to overestimate the nuclear flux of half of the objects by more than 50%. The median value for the ratios within 7.8″ aperture is 1.4.

3.3.2 Analysis of the Photometric Data

With the multiaperture and multicolor photometry we can exploit two further methods for separating the nuclear and the galaxy contributions. The *color given* method (Sandage 1973) is based on the assumption that the intrisic colors of both the nuclei and the galaxies have very narrow distributions. However, the correlation of the IR colors observed with the small apertures with the ratios of the nuclear to the galactic flux derived on the basis of the K frames turns out to be weak. Moreover, the $J-K$ colors of objects where the nuclear emission dominates ($F_{Kn}/F_{Kg} > 2$) show a considerable spread: they range from 1.4 to 2.1. Therefore the *color given* method is quite unreliable in the near IR.

The second method, the *template profile method*, is based on the assumption of a standard profile for the underlying galaxies. The adopted template intensity profile is described by 3 parameters: the disc radial scale r_D, the effective radius of the bulge r_e and the ratio I_e/I_D. We have used the median values of these parameters for a sample of about 30 early spiral galaxies studied by Kent (1985) using accurate surface photometry from CCD images in the J and F optical bands. The adopted values are $r_D = 5.2$ kpc, $r_e = 3.2$ kpc and $I_e/I_D = 0.38$.

As a check on whether such parameter values are appropriate also for the K band, we have compared the growth curve in this band, corresponding to the adopted profile, with that derived by Griersmith et al. (1982) from multiaperture J, H, K photometry of 65 early-type spirals (see Fig. 3.2). It is apparent that the two curves match well; the discrepancies are less than few hundreths of a magnitude in the

Name	K_n	δK_n	$(J-K)_n$	$(H-K)_n$	$(K-L)_n$	K_g	δK_g	C1[a]	Ref[b]
I Zw 1	10.11	.16	2.73	1.36	1.53	10.93	.19	c	5
Mkn 79	11.16	.17	2.16	1.08	1.66	10.54	.55	c	4,13
Mkn 352	12.36	.25	1.27	.63	1.39	11.71	.27	c	2,5
Mkn 374	12.27	.18	1.49	1.75	1.73	11.47	.20	c	1
Mkn 376	10.84	.19	2.58	1.52	2.11	...	...	c	1
Mkn 464	13.42	.22	1.46	.89	2.22	...	...	c	1
Mkn 478	11.06	.17	2.30	1.32	1.72	11.66	.17	c	1
Mkn 486	11.39	.18	2.15	1.32	...	11.98	.36	c	7,12
Mkn 493	12.62	.22	1.56	1.51	1.31	11.29	.30	c	6
Mkn 504	14.21	.66	1.19	.62	2.18	11.80	.68	c	3,5
Mkn 584	14.69	.72	1.89	1.42	...	11.92	.72	c	1
Mkn 618	11.51	.16	2.15	1.11	...	11.31	.37	c	7
Mkn 634	13.17	.27	1.97	.87	1.51	12.53	.27	c	1
Mkn 705	11.52	.16	1.64	.81	1.55	...	...	c	1
Mkn 734	11.94	.16	1.66	.93	...	...	...	c	6
Mkn 771	12.71	.28	2.89	.56	1.60	11.39	.29	c	7,10
Mkn 783	14.03	.38	1.40	.77	1.80	13.94	.38	c	1
Mkn 817	11.12	.28	2.99	1.79	1.34	10.22	.30	c	6
Mkn 871	12.46	.20	1.62	1.51	...	10.66	.23	c	6
NGC 5940	12.34	.18	1.80	1.00	1.43	...	...	c	1
Mkn 6	10.71	...	2.08	1.04	...	...	...	d	3,4

[a],[b] See table 3.3

Table 3.4: Resulting magnitudes and colors of the nuclear and galactic components. For the objects listed in this table, it has not been possible to derive the colors for the galactic component, which are instead *assumed* in order to get the nuclear colors (see text and also the previous table).

range of A/D_1 values, which correspond to apertures of 5″ to 15″ at the median redshift of the Seyferts in our sample ($z = 0.035$).

The total flux, $F_c(r)$, within an apertures r can be written as

$$F_c(r) = f_n(r)F_n + f_g(r)F_g \tag{3.1}$$

where F_g and F_n are the total fluxes of the host galaxy and the nucleus, respectively, and $f_g(r)$ and $f_n(r)$ are the fractions comprised within the aperture r. If photometric data with two apertures are available, the total nuclear flux F_n can be derived from the observed fluxes $F_c(r_{1,2})$:

$$F_n = F_c(r_2)\frac{F_c(r_1)/F_c(r_2) - f_g(r_1;r_2)}{f_n(r_1) - f_g(r_1;r_2)f_n(r_2)} \tag{3.2}$$

where $f_g(r_1;r_2) = f_g(r_1)/f_g(r_2)$ can be derived from the assumed galaxy profile, taking into account the PSF; $f_n(r_1)$ and $f_n(r_2)$ are determined only by the PSF.

We applied the *template profile method* whenever photometry with at least two apertures was available. In the K band, the method could be applied using only our own data for 22 sources (we have photometry with two apertures for one more, Mkn 739, but for it $K(7.8'') < K(5'')$). By searching the literature we have brought together K-band photometry with two apertures for 5 additional objects. For 27 objects we could thus compare nuclear magnitudes estimated with the *template profile method* with those derived from IRCAM frames. The histogram of the magnitude differences is shown in Fig. 3.3. In about 85% of the cases the absolute value of the difference is less than 0.25 magnitudes.

Thus a reassuring consistency is found between results based on IRCAM frames and those based on photometric data. The random errors in the nuclear magnitudes derived using the *template profile method* can be conservatively estimated as $\simeq$ 0.25 mag. We can conclude that this method can be used to derive the nuclear magnitudes of objects, for which multiaperture photometry is available. In the near IR it works much better than the *color given* method does.

For the 21 galaxies listed in Table 3.3, in addition to K-band frames we have JHK photometry with two apertures (our own data for the first 15 objects in the Table, partly collected from the literature for the remaining 6). These data can be combined to estimate the colors of the nuclei and of the surrounding galaxies. Assuming that the colors of the latter are aperture-independent (cf. Griersmith et al. 1982) and that the seeing is essentially the same both for K-band frames and for aperture photometry, we can write for, e.g., $(J-K)$ colors:

$$(J-K)_n = -2.5\log\left[\frac{(a_K(r_1)+1)\,10^{-0.4c(r_1)} - (a_K(r_2)+1)\,10^{-0.4c(r_2)}}{a_K(r_1) - a_K(r_2)}\right] \tag{3.3}$$

$$(J-K)_g = -2.5\log\left[(a_K(r_2)+1)\,10^{-0.4c(r_2)} - a_K(r_2)10^{-0.4(J-K)_n}\right] \tag{3.4}$$

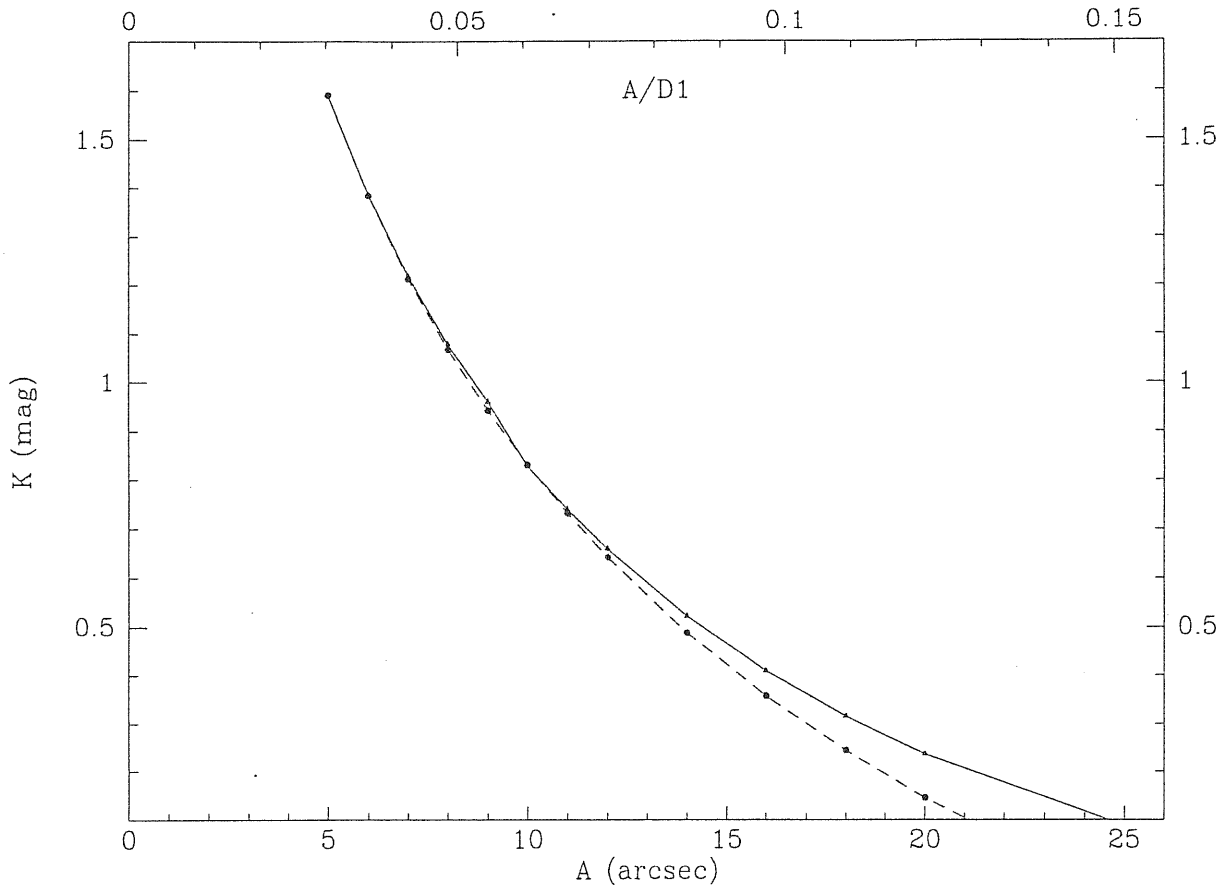

Figure 3.2: Comparison between the K-band growth curve corresponding to our template profile (solid line) and that determined by Griersmith et al. (1982) (dashed line). A is the aperture and D_1 is the angular diameter of the reference isophote at $\mu_B = 25\,\mathrm{mag\,arcsec^{-2}}$. The curve of Griersmith et al. (1982) refers to $D_1 = 165''$, the median value for their galaxies; the solid line refers to a galaxy at z=0.035, the median redshift of our sample.

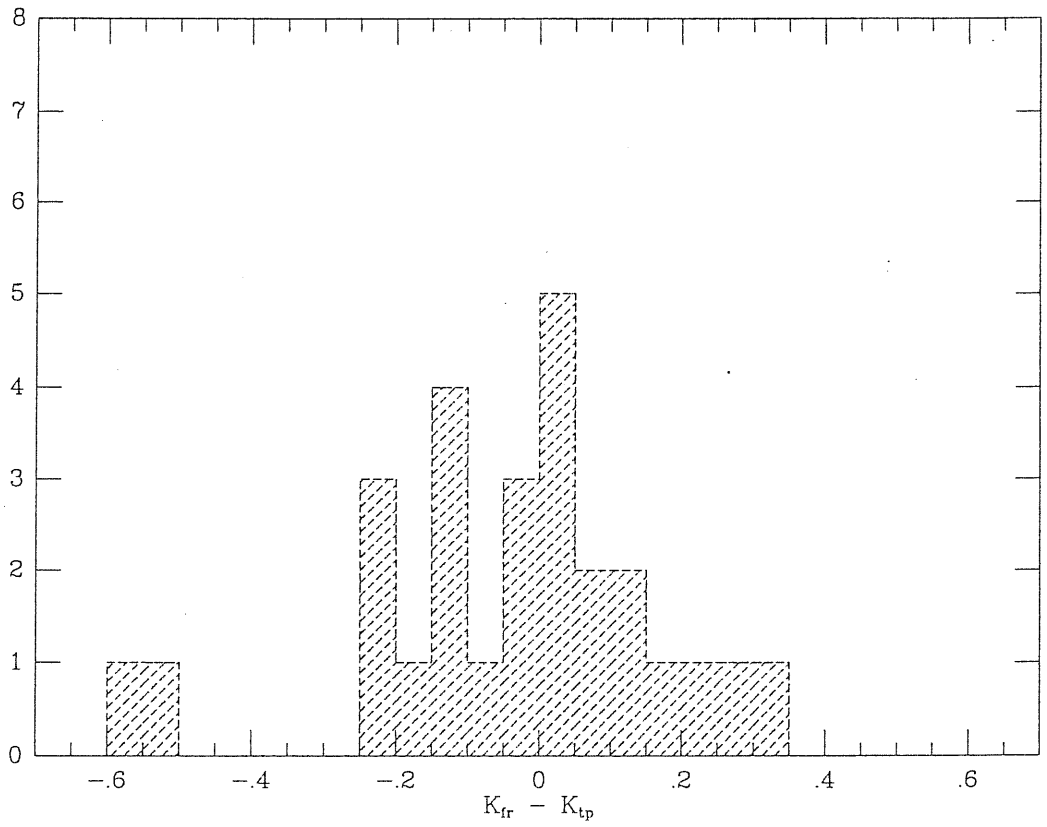

Figure 3.3: Distribution of the differences between the nuclear magnitudes derived from the best fit of the intensity profiles, K_{fr}, and those computed with the *template profile method*, K_{tp}.

where $a_K(r) = F_n f_n(r)/F_g f_g(r)$ can be derived from the analysis of K-band frames, and the color within the aperture r, $c(r)$ is obtained from aperture photometry. Analogous relationships hold for the $(H-K)$ and $(K-L)$ colors. The uncertainties on fluxes obtained with the above method can be estimated by adding in quadrature to the fractional error on K-band fluxes, a fractional contribution of about 0.15 due to uncertainties in the ratio $a_K(r)$ and on the observed colors.

A straightforward check of the validity of the method is possible in the case of MKN 704, for which we have also obtained a J frame with IRCAM. The analysis of the frame has given $J_n = 13.36$ to be compared with $J_n = 13.45$ obtained using the above equations.

For the same 21 objects we could also derive nuclear J and H magnitudes with the template profile method. The average differences with those obtained from eq. 3.4 are $\Delta J = 0.08 \pm 0.35$ (s.d.) and $\Delta H = 0.04 \pm 0.25$ (s.d.). Only MKN 530 shows large discrepancies (about 1 magnitude in J and 0.7 mag in H).

Using eq. 3.4 we can also compute the colors of the underlying galaxies. The results were compared with the colors of the rings between the two angular radii of 2.5″ and 3.9″ (obtained subtracting out the observed flux within the 5″ aperture from that measured within 7.8″), which, at the median redshift of the sample ($z \simeq 0.035$), correspond to $r \simeq 2.1$ kpc and $r \simeq 4$ kpc, respectively. For the 15 objects we observed both with the photometer and IRCAM at UKIRT, we found very good agreement, differences being less than 0.1 magnitudes except in one case. The distribution of the $(J-K)_g$ galactic colors is quite broad, ranging from 0.5 to 2.4 with a median value of 1.25. The distribution of $(H-K)_g$ colors has a smaller dispersion: it ranges from 0.05 to 1.6, with a median of 0.5. These values are redder than observed in normal early-type spirals ($\langle J-K \rangle \simeq 1.0$, $\langle H-K \rangle \simeq 0.25$; Griersmith et al. 1982; Devereux et al. 1987). Unfortunately only for nine objects we have got good enough data to allow reliable computations of the $(K-L)_g$ color of the host galaxies. Seven of them are quite red $[(K-L)_g \geq 1]$ and two have negative colors.

The median colors of the underlying galaxies ($(J-K)_g \simeq 1.25$, $(H-K)_g \simeq 0.5$) have been used to derive nuclear magnitudes, through eq. 3.4, when only single aperture photometry (in addition to K-band images) was available. This is the case for objects listed in Table 3.4. The present data are insufficient to reliably estimate $(K-L)_g$; based on indications that the colors of the host galaxies are close to those of starburst galaxies (cfr. § 4.1) we have assumed $(K-L)_g = 0.8$. We have checked that the derived L_n vary by no more than 0.15 mag when $(K-L)_g$ is increased or decreased by 0.1 mag. Of course, the uncertanties in the fluxes derived in this way are larger than those derived with the previous methods and the evaluation of the errors is not easy. It is clear that the uncertanties are smaller when the underlying

galaxy gives only a small contribution to the observed flux, as is usually the case in the L band.

The nuclear magnitudes of Mkn 6, the last object in Table 3.4, have been computed using the *template profile method* only.

Note that no K-corrections have been applied, so that the results refer to the observer's frame. On the other hand, owing to the relatively low redshifts of the galaxies, such corrections are bound to be small.

3.4 Discussion

3.4.1 Characteristics of the host galaxies

The morphologies of Seyfert galaxies have been studied by many authors (Adams 1977; Simkin et al. 1980; Yee 1983; MacKenty 1990) who concluded that the large majority of the Seyfert nuclei reside in early type spiral or S0 galaxies. More recently these studies have been extended to galaxies hosting QSOs and have found evidence of a rather generalized presence of disturbed morphologies and/or bars (see MacKenty 1990 and references therein).

The problems generated by the effective seeing and by the subtraction of the background in our K frames do not allow a detailed discussion of morphological properties. However it is worth noticing that our results support previous conclusions. A significant contribution from a bulge is not required by the fit of K-band intensity profiles in only 6 cases out of 41; for only one galaxy there is no evidence for a significant discs.

The optical luminosity distribution function of galaxies hosting AGNs has been investigated by Yee (1983), Malkan (1984), and MacKenty (1990) for optically selected samples; by Kruper and Canizares (1989) for a X-ray selected sample. Similar investigations have also been performed on galaxies harboring radio-quiet and radio-loud QSOs (Hutchings et al. 1984; Geheren et al. 1984; Smith et al. 1986; Veron-Cetty and Woltjer 1990).

In Fig. 3.4 we present the K-band luminosity distribution of host galaxies in our sample. Our results are particularly interesting because in the near IR we are looking at the emission of the stars comprising most of the luminous mass of a galaxy. Therefore we can expect that the near IR luminosity is a good tracer of the total galactic mass.

We have obtained a reliable determination of the absolute magnitude (M_{Kg}) for 35 objects. The median (which happens to coincide with the mean) value is $M_{Kg} = -25.5$. This value falls in the exponentially decreasing tail of the K-band local luminosity function of spiral galaxies computed by Franceschini et al. (1990).

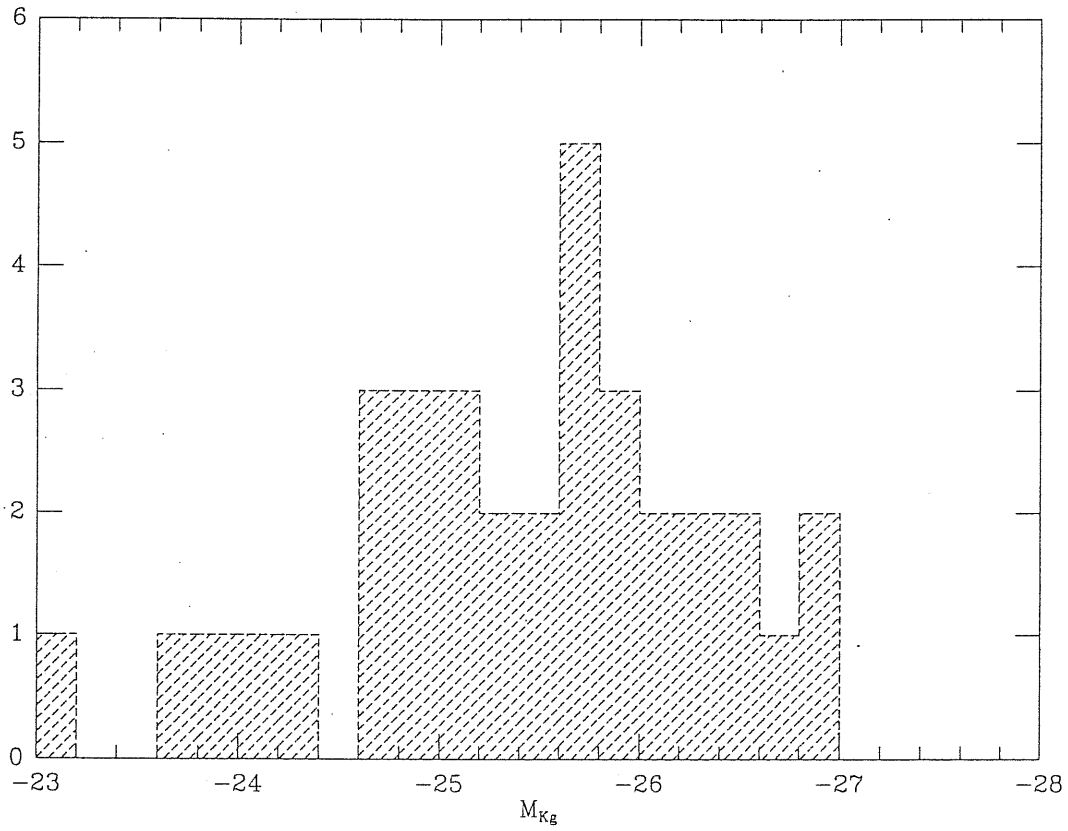

Figure 3.4: Distribution of the total K-band absolute magnitudes of the host galaxies.

Six out of these 35 objects are PG QSOs (Schmidt and Green 1983); for them we find $< M_{Kg} >= -25.8 \pm 0.24$ (again the median is equal to the mean). For the remaining 26 objects ("Seyferts") we get $< M_{Kg} >= -25.3 \pm 0.18$ (median $M_{Kg} = -25.4$).

If the colors of galaxies hosting an active nucleus are similar to those of normal early type spirals ($B - K = 4.15$, $V - K = 3.2$, Griersmith et al. 1982) the average $< M_{Kg} >$ corresponds to $< M_{Bg} >= -21.65$ and to $< M_{Vg} >= -22.6$ in the case of galaxies hosting PG QSOs; to $< M_{Bg} >= -21.20$ and to $< M_{Vg} >= -22.15$ for "Seyfert" nuclei.

In Fig. 3.5 we have plotted the monochromatic luminosities at 2.2μm of the host galaxies against those of the nuclei; there is a clear correlation, significant at the 99.9% confidence level, which, however, might be, at least partly, accounted for by selection effects. In particular, bright galaxies with low luminosity nuclei, which would populate the upper left hand corner, are likely to be under-represented in our sample of UV excess objects. On the other hand, there the correlation is still significant if we confine ourselves to bright nuclei. Using the K-band local luminosity function of spiral galaxies (Franceschini et al. 1990) we find that the fraction of such galaxies hosting a nucleus brighter than $M_{Kn} = -25$ (corresponding to $M_{Bn} \approx -22.5$) strongly decreases with galactic luminosity: it is $\simeq 3 \times 10^{-3}$ for $-27 < M_{Kg} < -26$, it falls to $P \simeq 3 \times 10^{-4}$, for $-26 < M_{Kg} < -25$, and becomes very small for galaxies fainter than $M_{Kg} = -25$.

It thus appears that bright AGNs tend to live in bright galaxies, whereas low luminosity nuclei may reside in galaxies of any luminosity.

As mentioned above, the $J - K$ and $H - K$ colors of galaxies in our sample are redder than those of the normal galaxies. On the other hand, they turn out to be essentially identical to those of starburst and HII galaxies: based on the samples of such galaxies observed by Lawrence et al. (1985) and Glass & Moorwood (1985) we find: $< J - K >= 1.25$, $< H - K >= 0.5$ and $< K - L >= 0.8$. Similar results have been derived by Joseph et al. (1984) for a sample of interacting galaxies. Given the close similarity of $J - H$ and $H - K$ colors we have assumed that also the mean $K - L$ color of galaxies hosting an active nucleus is similar to that of starburst galaxies, i.e. significantly redder than for normal spirals, for which $< (K - L) >\simeq 0.30$ (see e.g. Glass 1973; Allen 1976).

It is also interesting to note that the average values of $(J - H)_g$ and $(H - K)_g$ of the host galaxies are close to the values measured along the major axis of NGC 253 at distance of 1 to 3 kpc by Scoville et al. (1985), who argued that the colors are probably due to reradiation by hot dust associated with star forming regions.

Recent observations of CO emission in Seyfert galaxies detected molecular gas in the circumnuclear regions that could fuel both the nuclear activity as well as a moderate star forming activity. Heckman et al. (1989) have shown that Seyfert

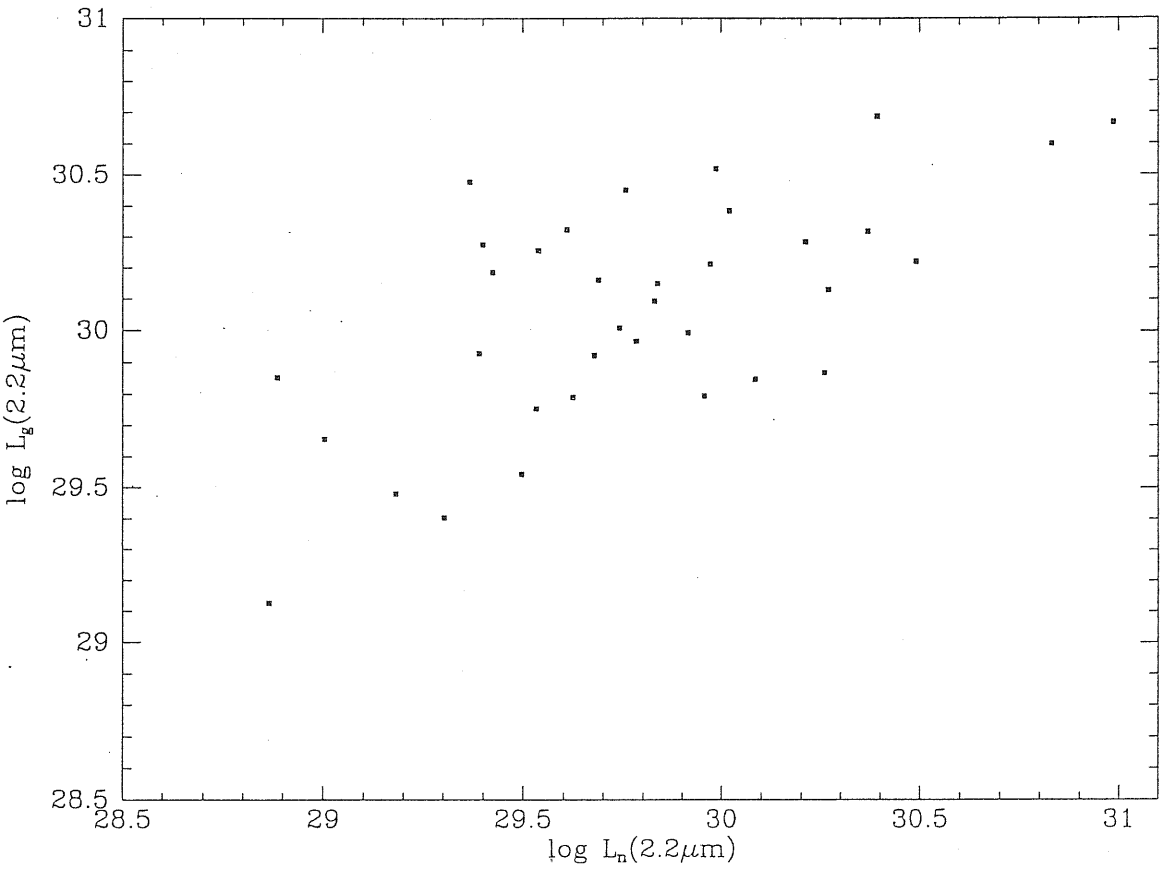

Figure 3.5: Galactic versus nuclear luminosities (erg/s/cm^2/Hz) at 2.2 μm.

galaxies of both types exhibit a well defined correlation between the CO and far-infrared luminosity, as normal and starburst galaxies do. They also pointed out that Seyfert 1 galaxies look relatively normal in the overall abundance of CO. Meixner et al. (1990) observed three nearby Seyfert 1 galaxies at high resolution and found that a large portion of their CO emissions come from regions within a few kpcs of the nucleus. Taniguchi et al. (1990) found that there is no significant difference in circumnuclear molecular gas densities between Seyferts and starburst nuclei.

We can conclude that in the central regions (less than few kiloparsecs away from the nucleus) starburst activity, though not spectacular, is rather common in galaxies hosting an active nucleus.

3.4.2 The emission at IRAS wavelengths

Using the IR luminosities of the nuclei and underlying galaxies, we can explore the problem of the respective contributions also in the far IR. More than half of the objects we observed in IR have been detected by IRAS and for the others reliable upper limits are often available.

In Figs. 3.6, 3.7, 3.8, 3.9a,b we have reported the luminosities (and upper limits) in the IRAS bands against the nuclear and the galactic luminosities at 2.2μm. It is apparent that the correlation between the 2.2μm nuclear and IRAS luminosities tends to weaken with increasing wavelength, whereas the opposite holds for the galactic luminosities $L_g(2.2\mu\mathrm{m})$. Of course in analizing the correlations it should be kept in mind that nuclear and galactic luminosities are correlated (see above).

We have investigated the correlations using various statistics: Kendall's coefficient of concordance W, Kendall's rank correlation coefficient τ, Kendall's rank partial correlation coefficient $\tau_{xy;z}$, Spearman partial rank correlation coefficient (Macklin 1982) and the usual correlation coefficient. In particular we used a generalized version of Kendall's rank correlation and of the usual correlation coefficient statistics which take into account also the upper limits in the observations (see Schmitt 1985; Isobe et al. 1986). In Table 3.5 we have reported the results.

All the tests indicate that the strongest correlation is between the nuclear luminosities $L_n(2.2\mu\mathrm{m})$ and 12 μm luminosities $L(12\mu\mathrm{m})$. For example the probability of reproducing the correlation by chance is $P_k \leq 10^{-5}$ both for W and τ statistics, and the correlation coefficient is high ($r = 0.8$). The analysis with the partial correlation coefficient confirms that the correlation between $L_n(2.2\mu\mathrm{m})$ and $L(12\mu\mathrm{m})$ is relatively independent of the galactic K luminosities: keeping $L_g(2.2\mu\mathrm{m})$ constant the correlation coefficient changes from 0.67 to 0.51 and the probability (computed using the Spearman partial rank correlation coefficient) that the correlation enterely arises from the $L_n(2.2\mu\mathrm{m})$–$L_g(2.2\mu\mathrm{m})$ and $L_g(2.2\mu\mathrm{m})$–$L(12\mu\mathrm{m})$ ones sep-

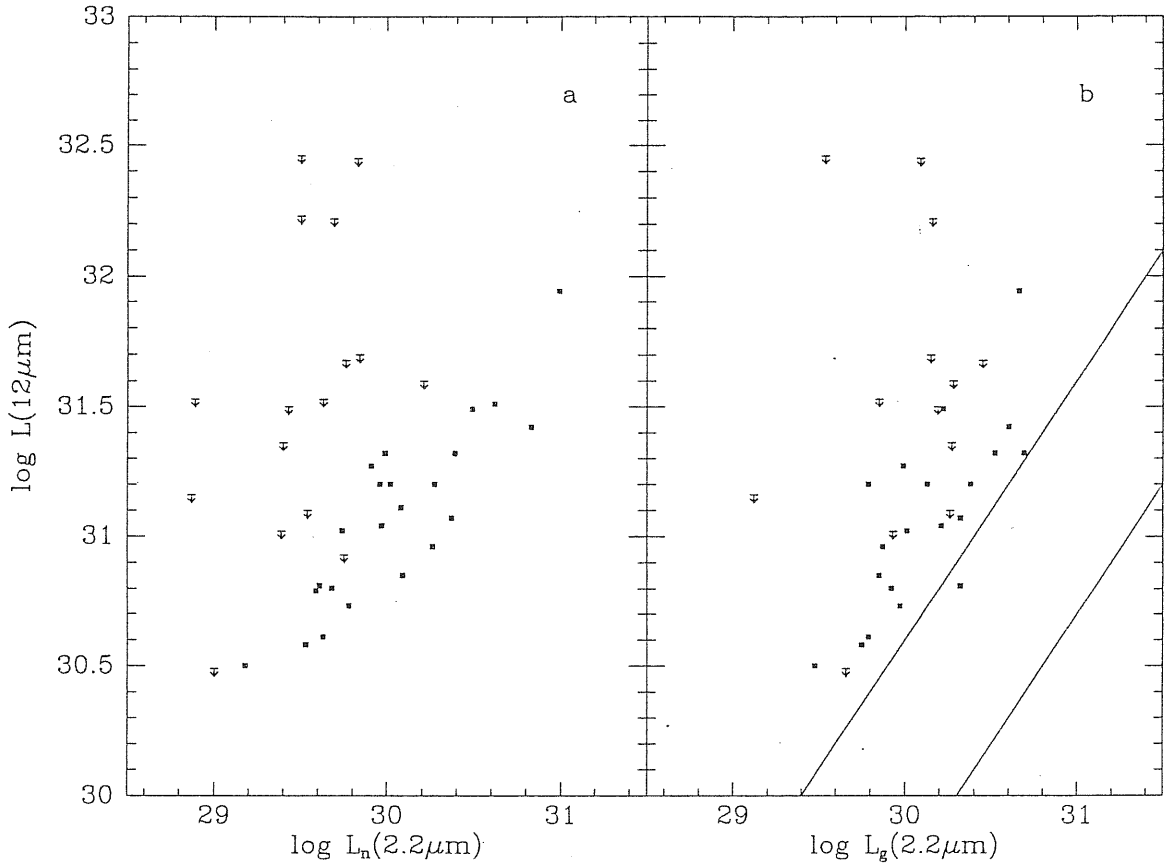

Figure 3.6: IRAS 12 μm luminosities versus nuclear (panel a) or galactic (panel b) luminosities at 2.2 μm. The upper and lower lines bound the range of galaxian contributions inferred from the distribution of 2.2 μm to 12 μm luminosity ratios for a sample of normal spiral galaxies (see text).

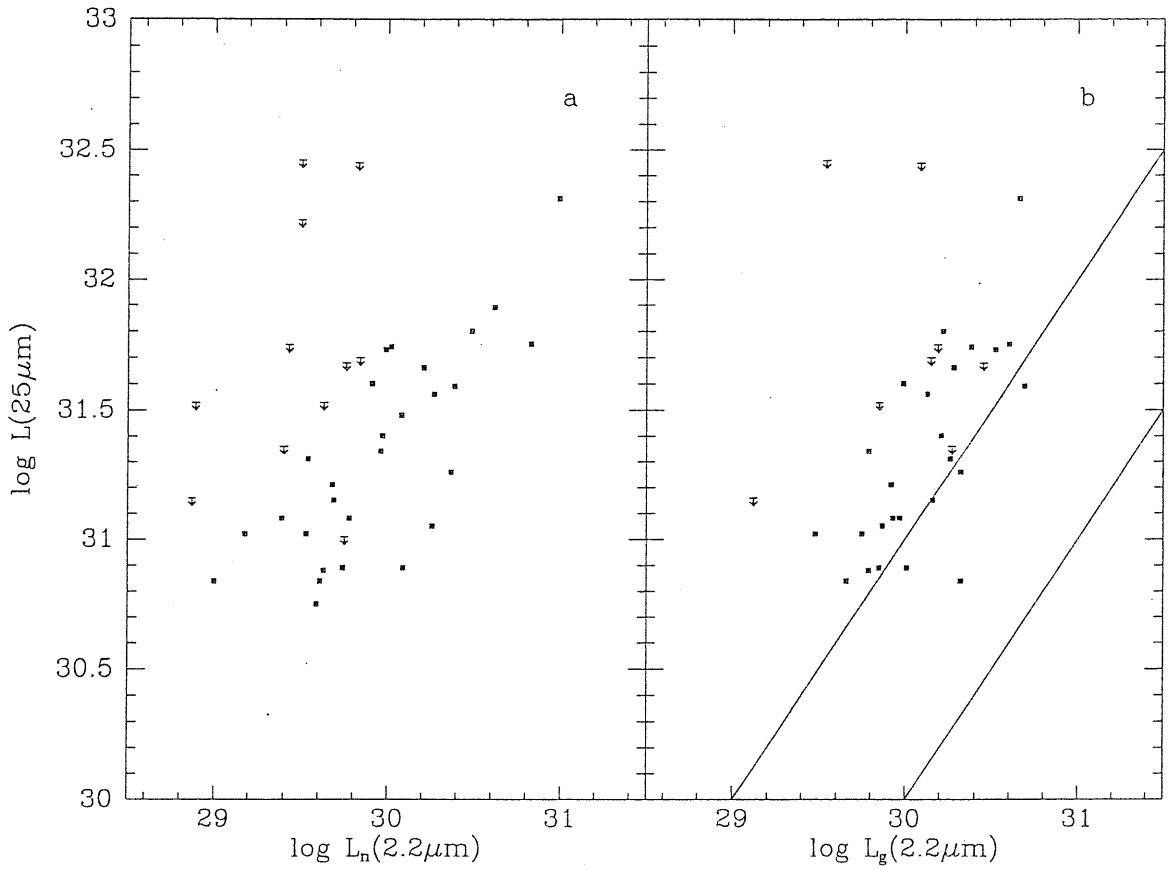

Figure 3.7: Same as the previous Figure but for 25 μm luminosities.

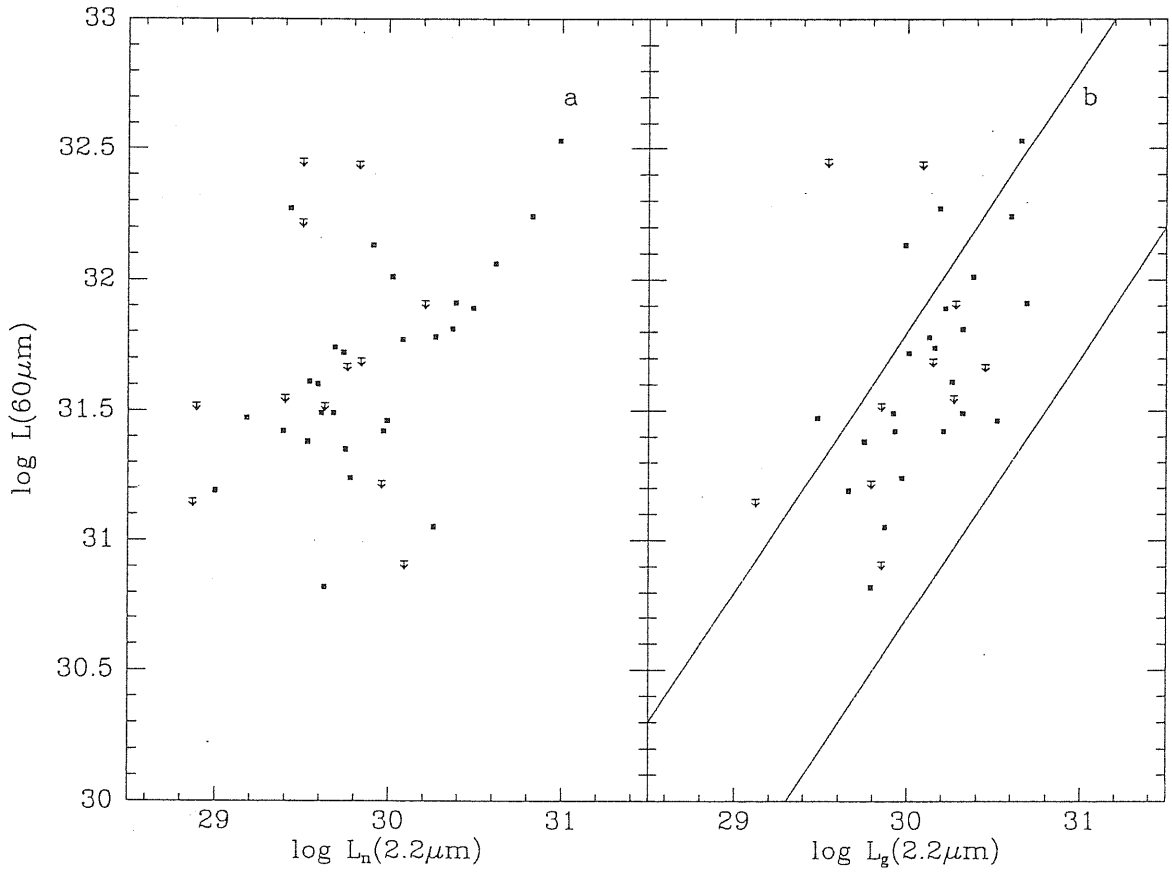

Figure 3.8: Same as the previous Figure but for 60 μm luminosities.

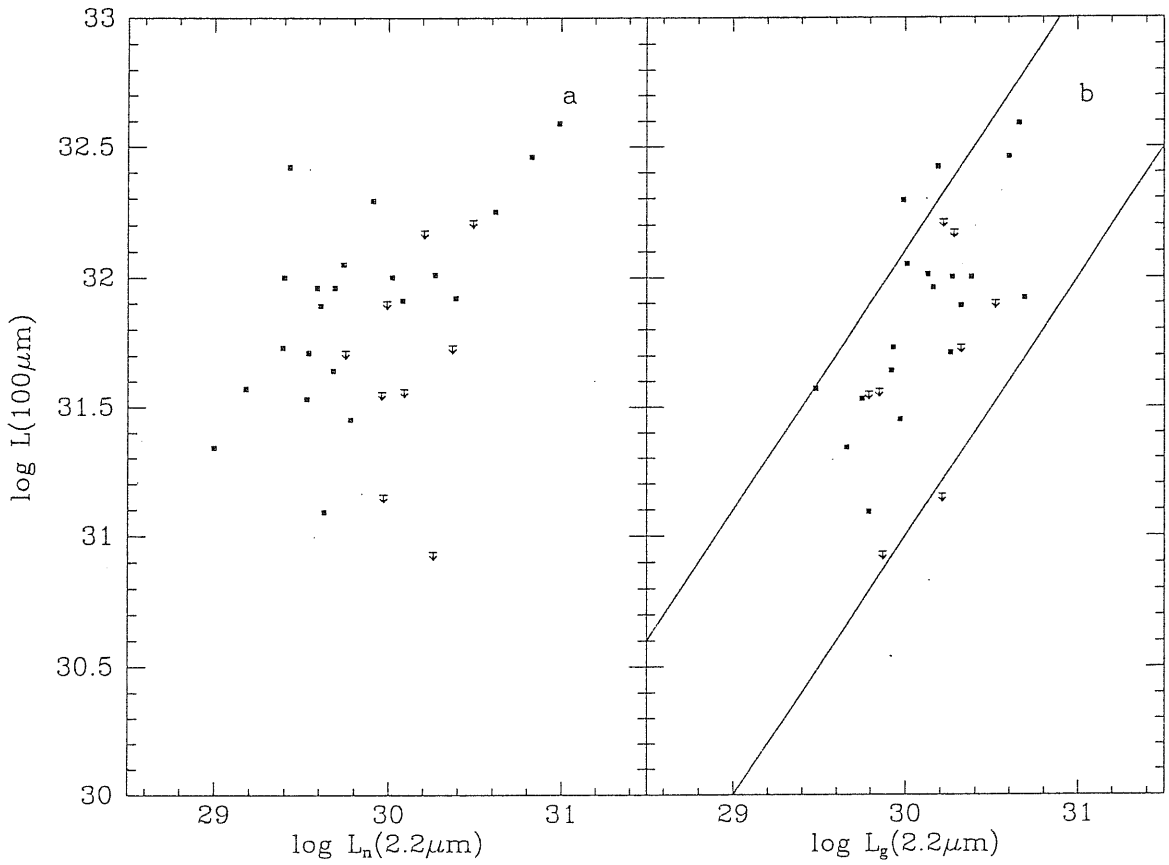

Figure 3.9: Same as the previous Figure but for 100 μm luminosities.

	Detections and Limits		Detections only		
Values Correlated	P_k	r	τ	$\tau_{x,y;z}$	$P_{x,y;z}$
$L_{2.2,n}$—L_{12}	8×10^{-6}	0.82	0.67	0.51	1.3×10^{-3}
$L_{2.2,g}$—L_{12}	7×10^{-4}	0.68	0.60	0.39	3.0×10^{-2}
$L_{2.2,n}$—L_{25}	7×10^{-6}	0.80	0.59	0.41	1.3×10^{-2}
$L_{2.2,g}$—L_{25}	3×10^{-4}	0.71	0.53	0.35	3.0×10^{-2}
$L_{2.2,n}$—L_{60}	4×10^{-3}	0.46	0.40	0.19	0.63
$L_{2.2,g}$—L_{60}	1×10^{-3}	0.71	0.48	0.36	1.3×10^{-2}
$L_{2.2,n}$—L_{100}	0.22	0.23	0.43	0.25	0.35
$L_{2.2,g}$—L_{100}	1×10^{-2}	0.47	0.49	0.37	2.5×10^{-2}

Table 3.5: 2.2μm-IRAS correlations.

arately is $P_{xy;z} \simeq 1.3 \times 10^{-3}$. The correlation between $L_g(2.2\mu\text{m})$ and $L(12\mu\text{m})$ is a little less significant ($\tau = 0.60$ and $r = 0.68$) and decreases substantially ($\tau = 0.39$) at constant $L_n(2.2\mu\text{m})$. The statistical predominance of the nuclear emission is confirmed even at 25 μm, whereas at 60 μm a clear change occurs. The correlation coefficient between $L_n(2.2\mu\text{m})$ and $L(60\mu\text{m})$ is $\tau = 0.41$, smaller than that between $L_g(2.2\mu\text{m})$ and $L(60\mu\text{m})$ ($\tau = 0.48$). Moreover the partial correlation coefficient between $L_n(2.2\mu\text{m})$ and $L(60\mu\text{m})$, at constant $L_g(2.2\mu\text{m})$, is only $\tau = 0.19$. The probability that the correlation $L_n(2.2\mu\text{m})$ and $L(60\mu\text{m})$ entirely arises from the $L_n(2.2\mu\text{m})$- $L_g(2.2\mu\text{m})$ and $L_g(2.2\mu\text{m})$-$L(60\mu\text{m})$ ones separately is high ($P_{xy;z} \simeq 0.63$), whereas in the case of $L_g(2.2\mu\text{m})$ and $L(60\mu\text{m})$ the probability of a completely induced correlation drops to $P_{xy;z} \simeq 1.3 \times 10^{-2}$. The indications of an increasing statistical relevance of the galactic contribution to the far IR emission with increasing wavelengths is confirmed by the 100 μm data. In this case the correlation coefficient of $L(100\mu\text{m})$ with $L_g(2.2\mu\text{m})$ is $r = 0.47$, but is only $r = 0.23$ in the case of $L(100\mu\text{m})$ versus $L_n(2.2\mu\text{m})$.

We conclude that the nuclear contribution to the far IR emission of Seyfert galaxies is definetely decreasing with increasing wavelength. As a further test of this conclusion we have examined the distribution of the ratios of the IRAS to the K-band luminosities of a sample of normal early type spirals. From a sample of normal spiral galaxies collected by Devereux (1987, 1989) we chose the objects observed in the K band with apertures large enough to allow for a reliable determination of their total luminosities. The ratios $L(12\mu\text{m})/L(2.2\mu\text{m})$ range from 0.5 to 4.5 with a median $r_{12-2.2} \simeq 2$; the $L(25\mu\text{m})/L(2.2\mu\text{m})$ ratios vary from 1 to 10 with a median value $r_{25-2.2} \simeq 4$; at 60 μm the ratios fall between 5 to 65 and the median value

is $r_{60-2.2} \simeq 22$; finally, the ratios $L(100\mu\text{m})/L(2.2\mu\text{m})$ are in the interval 10 to 120 with a median value $r_{100-2.2} \simeq 50$. For sake of comparison we notice that a small subsample of IRAS selected luminous bright galaxies observed by Carico et al (1988) have $100 \leq r_{60-2.2} \leq 700$. Using these results we have reported in Figs. 3.6, 3.7, 3.8, 3.9a,b the the maximum and minimum possible contribution (upper and lower curves) of the host galaxies to the total luminosities. While the observed luminosities at 12 and 25 μm are mostly above the maximum, at 60 and 100 μm they are well within the possible contributions of the host galaxies.

Rodriguez Espinosa et al. (1986,1987) pointed out that the spectral indices between 60 and 100 μm, α_{60-100}, ($f_\nu \propto \nu^\alpha$) of Seyfert and starburst galaxies are quite similar. We confirm their result for our sample of Seyferts, which has a α_{60-100} distribution similar to that of the starburst galaxies of the optically selected sample investigated by Sekiguchi (1987). However their claim that 75% of the Seyfert galaxies in their sample have *massive* starburt episodes, is based on a rather arbitrary choice for the lower limit of the luminosities of the starburst galaxies ($L_{fir} > 10^{44}\,\text{erg}\,\text{s}^{-1}$. Actually, as we have shown above, the galaxies hosting AGNs are usually brighter that L_* (the typical luminosity where the luminosity function is falling exponentially) and the 60 and 100 μm emissions of the Seyferts are compatible with the emission from the host galaxies, with ratios between the IR (stellar) and the far-IR (dust) luminosities typical of normal or moderate starburst galaxies.

In conclusion there is statistical evidence that in Seyfert 1 galaxies the nuclear emission largely dominates at 12 μm and is still important at 25 μm, while longward of 60 μm the emission from the host galaxies is overhelming. This result is also in keeping with the fact that in a 12 μm flux-limited sample the percentage of galaxies harboring active nuclei can be higher than 20% (Spinoglio and Malkan 1989).

A similar conclusion has been drawn by Berriman (1989) on the basis of the correlation of the polarization with the luminosities at 12 and 25 μm.

If the observed IR and mid-IR spectrum is ascribed to synchrotron emission, as suggested by Band & Malkan (1989), a consequence of the galaxy dominance at 60 μm is that the turnover in the synchrotron self-absorbed power law must occur at shorter wavelengths. At longer wavelengths the spectrum of Seyfert 1 is likely to be dominated by the cold dust emission in the host galaxies, in agreement with the steep fall-off of the spectrum of Seyfert 1 galaxies and QSOs in the submillimeter regions observed by several authors (Engargiola et al. 1988; Chini et al. 1989; Lawrence et al. 1991).

As expected from the above discussion, the Seyfert 1 galaxies of our sample exhibit a slope α_{12-60} definetely flatter than those of normal and starburst galaxies. As it is apparent from Fig. 3.10 , the distributions of α_{12-60} for our sample and for an optically selected sample of normal spiral galaxies detected at 12 μm are

quite different with a negligible probability $P(F1 = F2) \leq 4 \times 10^{-5}$ that they have been drawn from the same parent population (here and in the following we will use the Gehan's test and the Peto-Prentice generalized Wilcoxon statistic in comparing distributions).

For starburst galaxies Xu & de Zotti (1989) found an average $\alpha_{12-60} \simeq -1.9$, while the median value of our Seyfert galaxies is -0.9 (for both classes we used in the statistics only objects detected at both wavelengths).

On the other hand the distribution of the slopes α_{12-60} for the Seyfert 1 galaxies in the CfA sample looks very similar to that of our Seyferts ($P(F1 = F2) \simeq 0.15$), as might be expected on the basis of the fact that about half of the objects are common to the two samples. However in the CfA sample there are five objects out of nineteen with $\alpha_{12-60} < -1.5$, the minimum value for our sample; three objects, NGC 2992, NGC 3227 and NGC 5033, have very low total luminosities ($M_B > -19.4$) and two others, MKN 231 and NGC 7469, have large starbursts (Aitken et al. 1981; Cutri et al. 1984).

The IRAS data on the hard X-ray selected AGN sample of Piccinotti et al. (1982) again confirm that the AGNs have α_{12-60} slopes flatter than normal and starburst galaxies; the statistical tests on this distribution in comparison to ours give $P(F1 = F2) \simeq 0.20$.

It is worth noticing that the Seyfert 1 galaxies selected on the basis of their 12 μm emission by Spinoglio and Malkan 1989 show a distribution of α_{12-60} quite similar to those of our optically selected sample [$P(F1 = F2) \sim 0.2$].

Seyfert 2 galaxies in the CfA sample (Edelson et al. 1987) and those selected at 12 μm (Spinoglio and Malkan 1989) exhibit distributions much broader than those of Seyfert 1 samples (the probability that they are drawn for the same parent distribution is only $P \sim 2 \times 10^{-3}$), probably because of a larger variety of luminosity ratios among different emission mechanisms. However in this context it is quite interesting to note that NGC 1068 has a slope $\alpha_{12-60} \simeq -1$, close to the average value of our sample.

In a sample of optically selected non-active spiral galaxies the objects with $\alpha_{12-60} \geq -1.5$ are only 15% of the total number; the percentage reaches 20% if the primary selection has been done at 12 μm. Contrariwise, less than 15% of Seyfert 1 galaxies have $\alpha_{12-60} \leq -1.5$, independently of the primary selection (optical or mid-IR); these objects usually possess faint nuclei or exhibit large starbursts. No non-active spiral galaxy has a slope flatter than -1.1, while more than 50% of the Seyfert 1 galaxies do. Therefore we can conclude that extragalactic objects with $\alpha_{12-60} < -1.5$ are good AGN candidates.

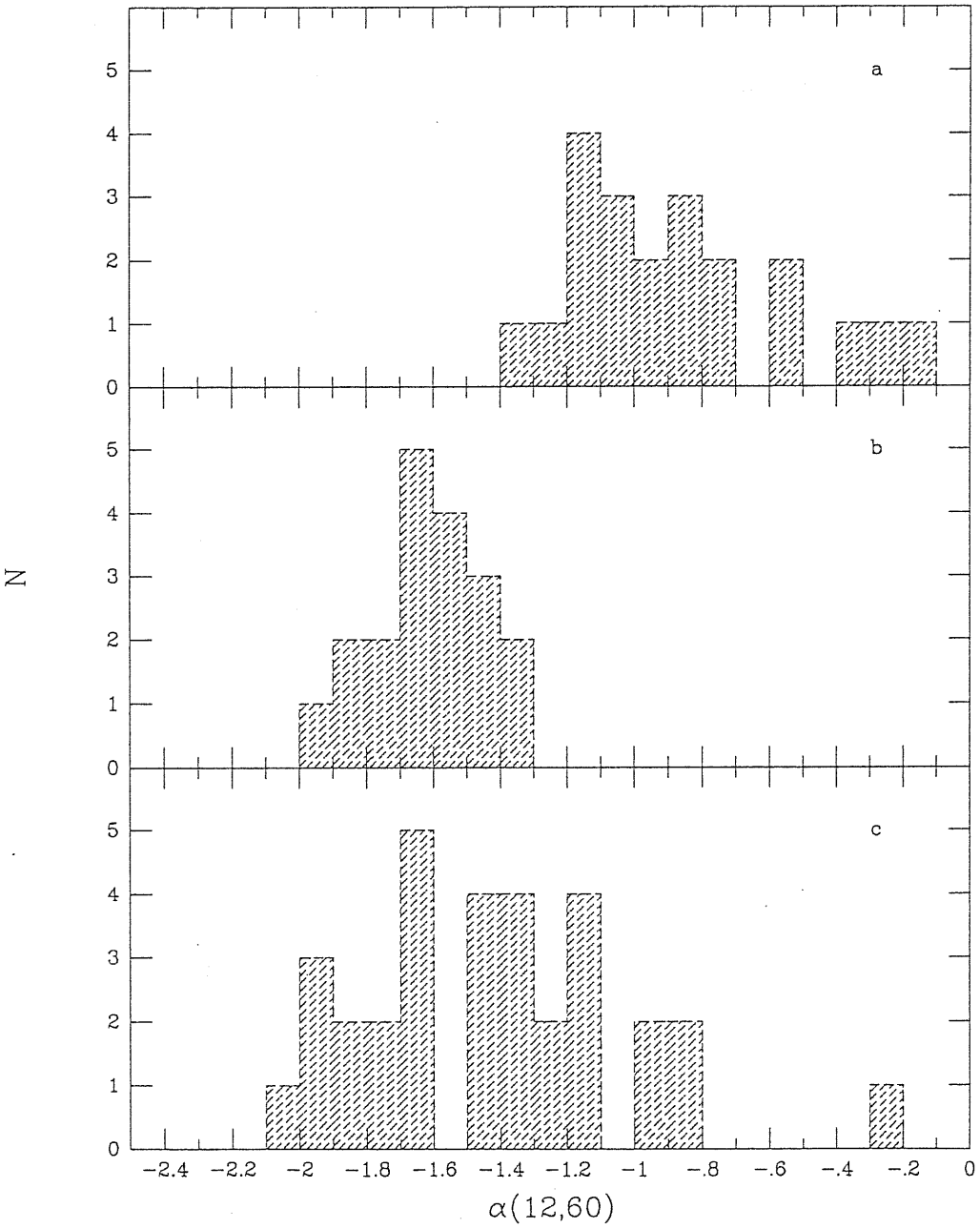

Figure 3.10: Distributions of the α_{12-60} slopes. Panel a: type 1 Seyferts in our sample; panel b: normal optically selected spirals; panel c: type 2 Seyferts selected at 12 μm (Spinoglio and Malkan 1989).

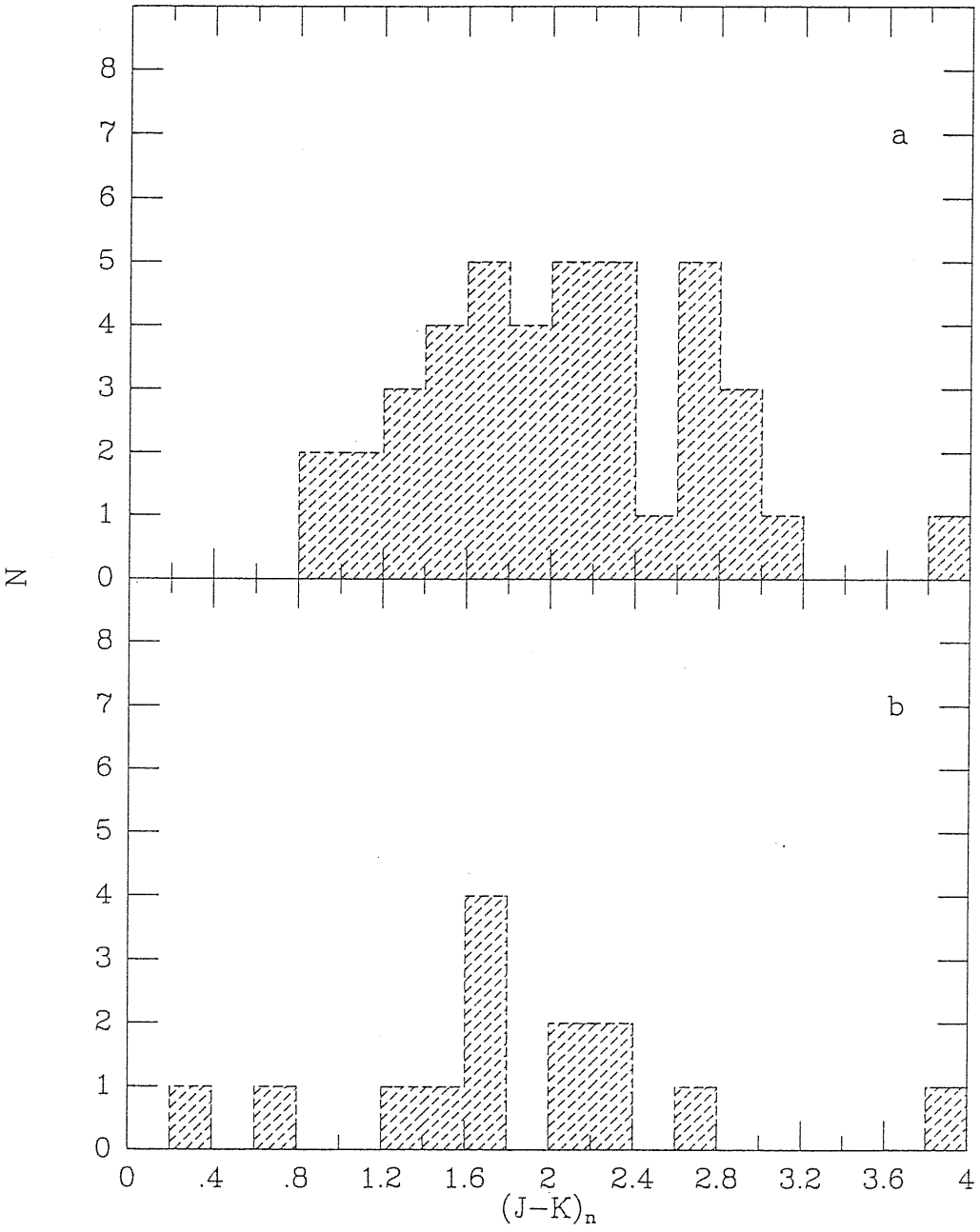

Figure 3.11: Distribution of nuclear (J-K) colors. Panel a: our sample; panel b: hard X-ray selected sample (McAlary and Rieke 1988).

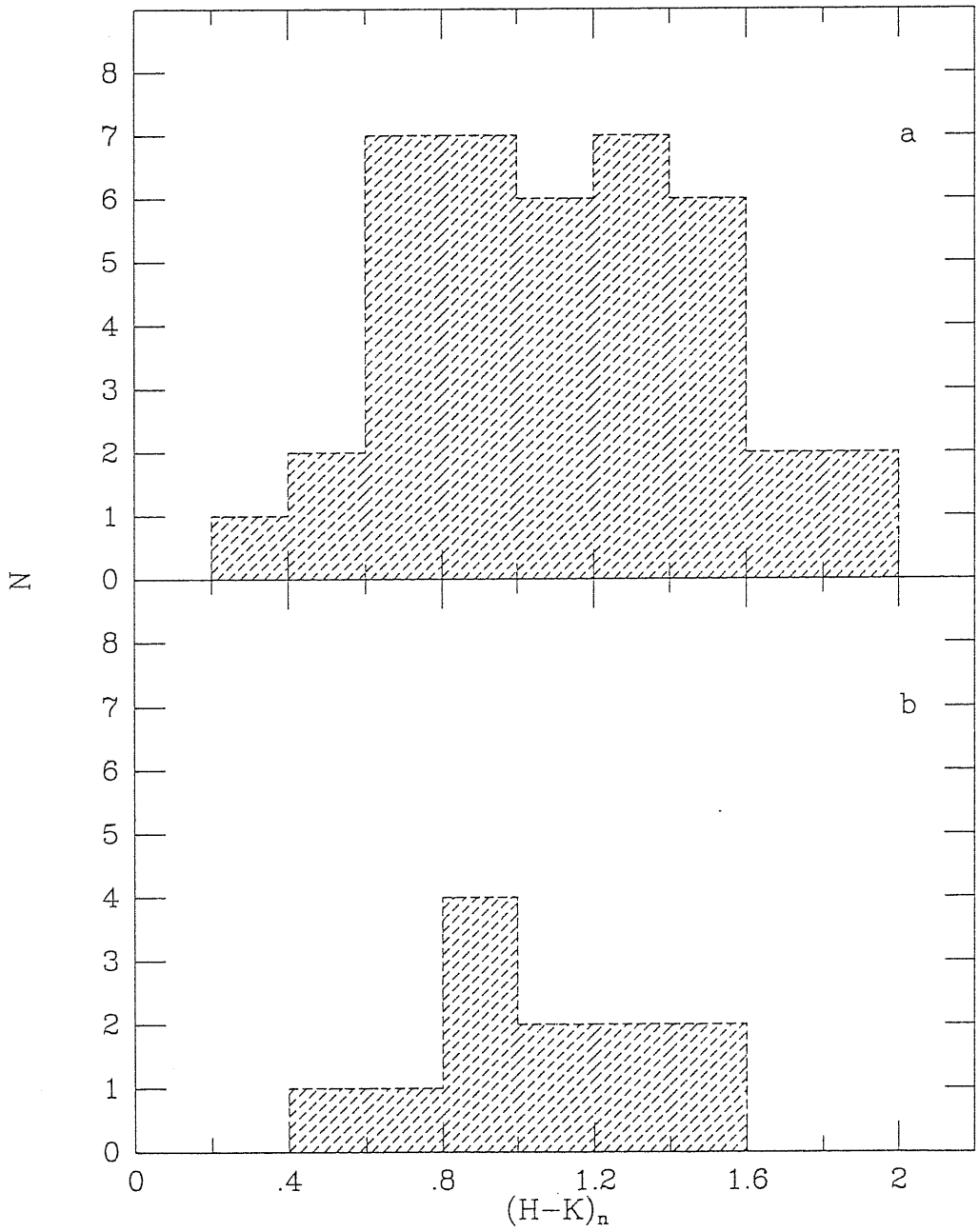

Figure 3.12: Same as the previous Figure but for (H-K).

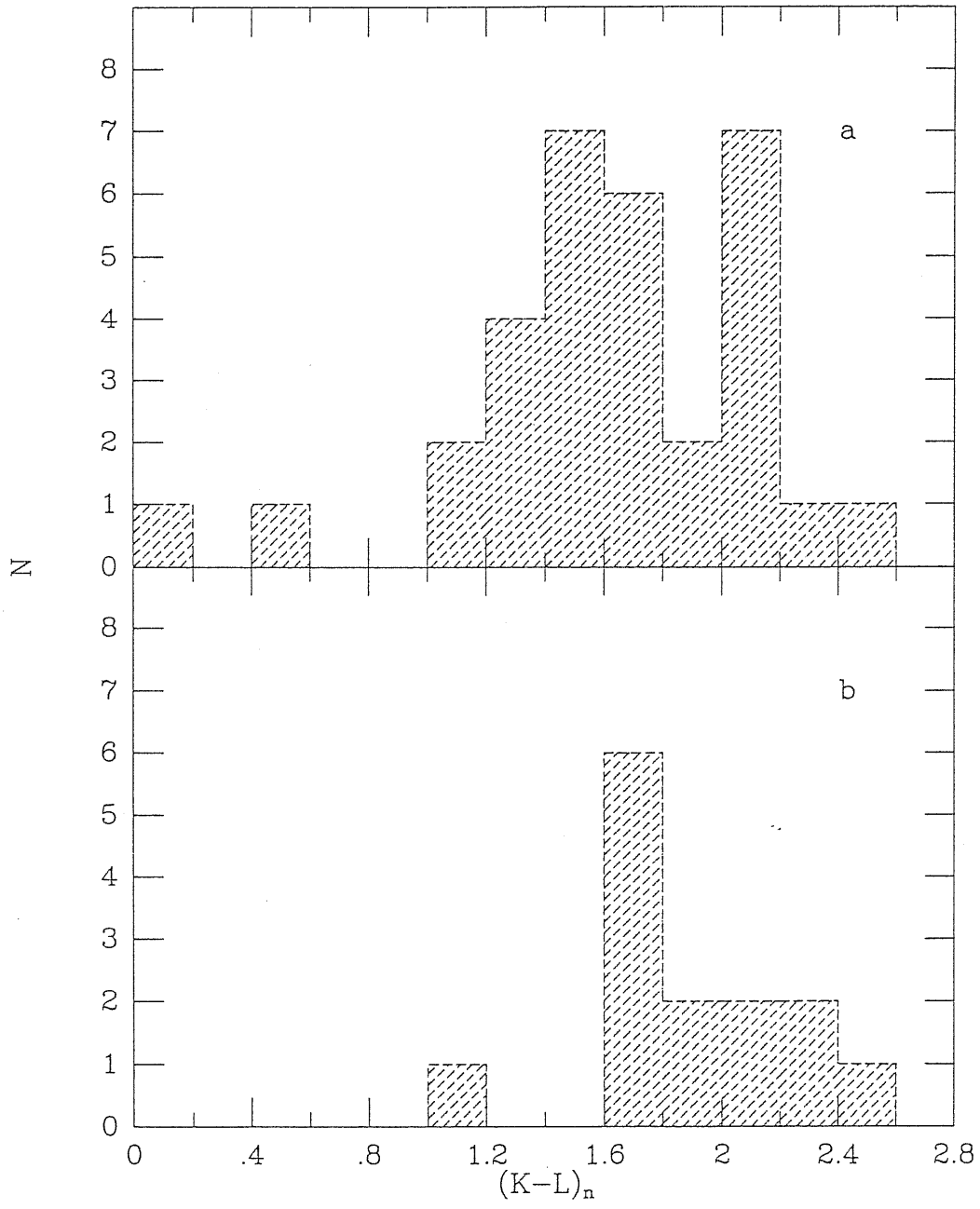

Figure 3.13: Same as the previous Figure but for (K-L).

3.4.3 Near and mid-IR colors of the nuclei

The distributions of the $(J-K)_n$, $(H-K)_n$ and $(K-L)_n$ colors of the nuclei of our sample are presented in Fig. 3.11, 3.12, and 3.13. The average values, $< J-K >= 2.06 \pm 0.1$ (rms), $< H-K >= 1.10 \pm 0.06$, $< K-L >= 1.64 \pm 0.09$, for our sample are quite close to the median values, but it is evident that there is a considerable spread. For sake of comparison we have reported in the figures the IR colors of the nuclei of the X-ray selected sample of Seyfert galaxies (McAlary and Rieke 1988). The distributions of (J-K) and (H-K) colors are very similar; as an example, for $(J-K)_n$ colors the statistical tests give $P(F1 = F2) \simeq 0.6$. However the nuclei of the X-ray selected sample have redder (K-L) colors.

The average slopes between the 2.2, 12 and 25μm are $\alpha_{2.2-12} = -1.4$ and $\alpha_{2.2-25} = -0.88$ for our sample, while for the X-ray selected sample the values are -1.76 and -1.26 respectively. This fact is suggestive of a larger amount of warm dust in the hard X-ray selected objects.

Many nuclei in the sample exhibit curved IR spectra, with an excess at 3-5 μm already noted by several authors (see e.g. Neugebauer et al. 1979). A detailed analysis of the spectra of the nuclei from the X-ray to the radio band will be presented elsewhere (Granato et al., in preparation). However our optical and IR data confirm the claim by Sanders et al. (1989) that a minimum in νf_ν around 1 μm is a common feature in AGN spectra. This minimum suggests that the emission mechanism dominating the optical part of the spectrum fades at longer wavelengths, where a different process is emerging.

If we take into account the emission by the host galaxies at $\lambda \geq 60\,\mu$m (see §4.2), the nuclear spectra are remarkably curved. Synchrotron models have many drawbacks in fitting this kind of spectra, because they require high magnetic fields (larger than hundreds Gauss), small sizes of the emitting regions (smaller than several light-days) and large ratios of the photon-to-magnetic energy density (see Band and A 1989; Lawrence et al. 1991). On the other hand, dust emission models naturally reproduce the raising in the near IR (dust grains sublimate at 1000–1500 K) and the fall off at $\lambda \geq 60\mu$m (Barvainis 1987; Barvainis 1990; Sanders et al. 1989).

In this context it is also worth noticing that the $(J-K)_n$ colors are redder while the $\alpha_{2.2-12}$ and $\alpha_{2.2-25}$ slopes are flatter for the brightest objects. Sanders et al. (1989) already noticed a flattening of the spectra of their PG QSOs with the lowest luminosities ($L_{bol} < 10^{12} L_\odot$). However they interpreted this effect as due to the contribution of the host galaxies, while in our case we have already subtracted the galactic contributions.

3.4.4 The relation of the IR to the X-ray nuclear luminosity

The correlation between near IR and X-ray luminosities of AGNs has been explored by many authors (Glass 1979; Malkan 1984; Wilkes and Elvis 1987; Carleton et al. 1987; Mushotzky and Wandel 1989; Sanders et al. 1989), to probe the relevance of the non-thermal emission in the IR band. So far no definite conclusion has been reached.

Although the objects of our sample detected in X-rays span only two decades in flux or in luminosity both at 2.2 μm and at 2 keV (Fig. 3.14a,b), a positive correlation is discernible. Kendall's rank test gives a probability of 0.03 that the correlation of the fluxes is spurious. As for the luminosities the probability of a spurious correlation falls to $P \leq 0.003$. The classical correlation coefficient is also significant ($r = 0.58$) and the fit suggests that the correlation is not linear: $L_{2\mathrm{keV}} \propto L_{2.2}^{0.63\pm0.17}$. The result is in reasonable agreement with that found by Kriss (1988), who explored the correlation of the 2 keV luminosity with the luminosity at 1 μm for a sample of 88 AGNS and radio-quiet QSO's. Indeed, using the 1.26 μm monochromatic luminosities, we found $L_{2\mathrm{keV}} \propto L_{1.26}^{0.70\pm0.18}$ quite close to Kriss' result ($L_{2\mathrm{keV}} \propto L_{1\mu\mathrm{m}}^{0.73}$). Moreover the fluxes at 2 keV are more tightly correlated with the 1.26μm (probability of a spurious correlation $P \sim 0.005$) than with the 2.2μm fluxes. A closer to linear correlation has been found by Mushotzky and Wandel (1989) between the X-ray and 0.75 μm rest frame luminosities ($L_x \propto L_{0.75}^{0.85}$). On the contrary, Sanders et al. (1989) claimed that there is no evidence of any correlation between the 2 keV and the 3.5 μm fluxes of PG QSOs, and argued that objects covering a narrow range of fluxes occupy a strip in luminosity-luminosity plots, thus mimicking a correlation.

All these authors have used *Einstein Observatory* X-ray data.

Hard X-ray data were used by McAlary & Rieke (1988) who concluded that the emission at 6 keV of their *hard X-ray* selected sample of Seyfert 1 galaxies doesn't show any significant correlation with the emission at 3.5 μm. On the other hand, Carleton et al. (1987), using a similar sample, found a strict correlation between the hard X-ray and the infrared *baseline* luminosity; they exploited this correlation to derive a rough estimate of the possible non-thermal IR component.

Our statistical analysis suggests that the correlation between X-ray and IR emission is significant at $\lambda = 2.2\mu$m and increases both in significance and in linearity with decreasing IR wavelength. These facts are not in contrast with an IR continuum dominated by thermal dust reradiation. Actually many models predict a tight connection between X-ray and UV-optical emissions of AGNs: X-ray photons can be produced by Compton upscattering of UV-optical photons by high energy electrons, or, alternatively, X-ray primary photons may be reprocessed into UV-optical

photons (see e.g. Collin-Souffrin 1991). On the other hand thermal dust emission is directly powered by the UV emission of the nucleus. Therefore is not surprising that a significant correlation between the IR and X-ray emissions exists. Of course this argument also implies that the variability in the three bands are related (see below).

A further interesting fact is that an important fraction of the total luminosity of the nuclei is emitted in the near and mid-IR: for the majority of our objects the IR (1.2–25μm) luminosity is more than 3 times their X-ray luminosity (2–10 keV) and can reach $30 - 40\%$ of the bolometric luminosity. Therefore any model which attributes the IR emission to dust must solve the problem of producing such huge amount of light at shorter wavelengths and enough dust to absorbe it.

The studies on the variability of Fairall 9 (Clavel et al. 1989) support this conclusion. While the optical and the J fluxes varied in the same sense and in phase with the UV continuum, the K and L emission shows a delay of about 400 days, that is suggestive of dust emission. Moreover at IRAS wavelengths normal QSOs and AGNs show no evidence of variability (Edelson and Malkan 1987) at least on time scales of up to few months.

3.5 Summary and Conclusions

We have presented and analyzed IR data on 41 objects out of the 56 comprised by the *homogeneous* sample of optically selected AGNs described in the previous chapter. High resolution K band images have been obtained for 41 objects using the IRCAM system and the respective intensity profiles have been computed and analyzed. We have also observed 27 objects of the sample with the UKT9 and UKT6 photometers in JHKL bands, with 5″ and 7.8″ apertures.

A method for reliable determinations of nuclear and galaxian fluxes using K band frames has been presented. To save computing time without loosing much information, the use of the intensity profiles has ben suggested. The host galaxies have been modeled as a superposition of bulge and disc. Their intesity profiles have been derived taking into account the effects of seeing and inclination. The nuclear profiles shaped by the seeing has then been added to get the global profiles, that depend on 5 parameters. The best fit parameters have been obtained by χ^2 minimizations. Two main problems hampered the evaluations of the parameters, the total seeing and the background subtraction.

In absence of previous comparable results, we resorted to test the reliability of the nuclear fluxes by comparison to he fluxes derived by a different method, based on multiaperture photometry. We have shown that the galactic profile can be well represented in the inner parts by a template. In this *template profile* only the

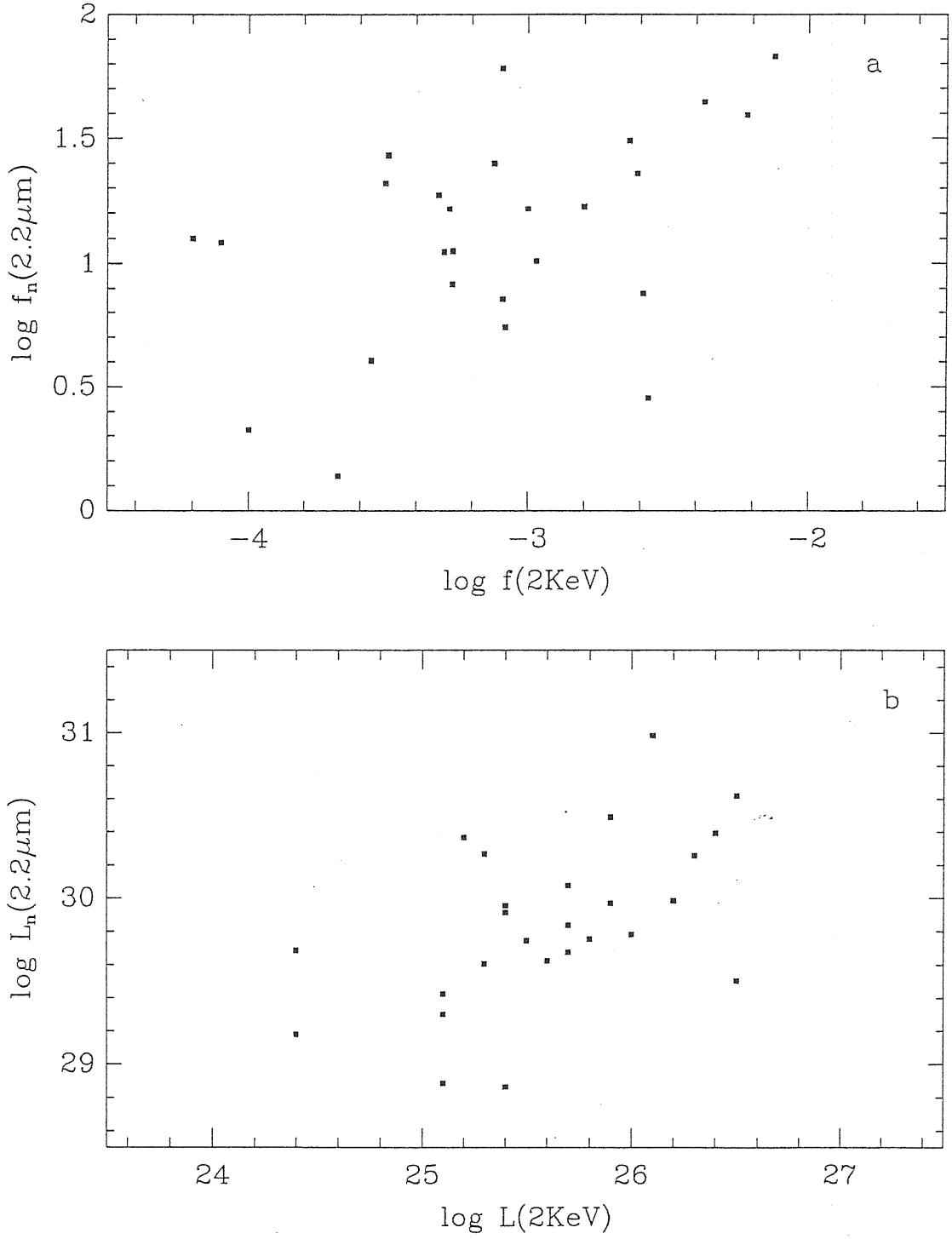

Figure 3.14: Panel a: nuclear fluxes at 2.2 μm versus fluxes at 2 keV (mJy). Panel b: same as in panela but in terms of luminosities (erg/s/Hz).

normalization is free and thus two apertures are enough to estimate the nuclear and galactic fluxes. The results obtained using the *template profile* method are in good agreement with those derived by the frames.

We have also obtained reliable values of the total magnitudes of 35 host galaxies. It is the first statistically significant sample of total K band magnitudes of galaxies hosting AGNs.

Almost all the galaxies exhibit detectable bulge and disk components, confirming that AGNs are preferentially located in early type spirals. The average luminosity of the host galaxies falls in the high luminosity tail of the K band luminosity function of the spiral galaxies. The probability that a spiral galaxy hosts a bright AGN increases with its luminosity. The average colors of the hosts are very close to the colors of moderately starbursting galaxies.

The galaxian $2.2\,\mu$m luminosities correlate with 60 and $100\,\mu$m luminosities, whereas the 12 and $25\,\mu$m luminosities show a tighter correlation with the nuclear luminosities. This fact statistically demonstrates the predominance of the disc emission longward of $25\,\mu$m. As a consequence, any synchrotron emission must fall off at these wavelengths. The total 60 and 100 μm luminosities can be easily accounted for if the host galaxies have $L(60\,\mu\mathrm{m})/L(2.2\,\mu\mathrm{m})$ and $L(100\,\mu\mathrm{m})/L(2.2\,\mu\mathrm{m})$ ratios similar to those of galaxies with normal or moderately enhanced star formation rates.

We also found that the slope α_{12-60} can be used to efficiently select AGN candidates. In particular only 15% of Seyfert 1 galaxies in our sample (either hosting a weak nucleus or undergoing a violent starbust) have $\alpha_{12-60} < -1.5$, whereas 85% of the normal galaxies do.

The curved IR spectra of the nuclei are more easily modelled by dust emission rather than by synchrotron. Moreover synchrotron emission would imply variability on time scales of order of several light-days, whereas at IRAS wavelengths radio-quiet QSOs and AGNs show no evidence of variability (Edelson & Malkan, 1987) at least on time scales of up to few months.

Our data confirm that there is correlation between the IR (K band) and the X-ray (2 keV) emissions. We have also found that the correlation strengthen with decreasing wavelengths. We argued that this is not in contrast with dust emission dominating the IR. Actually almost all the models of AGN continua predict a strict correlation between the UV-optical and X-ray luminosities; the correlation between X-ray and IR can be induced by the fact that dust is heated by UV-optical radiation. The studies on the variability of Fairall 9 (Clavel et al. 1989) support the dust emission model. While the optical and the J fluxes varied in the same sense and almost in phase with the UV continuum, the K and L emissions show a delay of about 400 days.

Our data support a picture in which the nuclear emission of optically selected AGNs in the IR is the sum of three components. The first one is the fading part of the UV-optical emission. At $\lambda \geq 3\mu$m it is overwhelmed by the emission of the *circumnuclear* dust, which is important up to $\lambda \simeq 60\mu$m, where the galactic disc contributions start to dominate the total emission.

We have obtained optical CCD images in the B, V, R and I bands of the objects studied in the IR and we will present the data and the results elsewhere. The optical data togheter with the X-ray and the radio data largely available for the sample objects will enable us to discuss the overall shape of the nuclear continua of almost all the AGNs in the *homogeneous* sample (Granato et al. in preparation).

Chapter 4

Discussion of the Optical Data

Summary. We present CCD observations in BVR optical bands of the homogeneous sample of AGNs defined in Chapter 2, that we also observed in near–IR JHKL bands (Chapter 3). Also to this imaging data we have applied the same analysis procedure described in Chapter 2, and the results are presented together with a preliminary discussion. We have addressed the problem of the uniqueness of the set of the fitting parameters. A statistical analysis shows that the distributions of morphological parameters are similar to those of normal early type spirals. The galactic colors suggest a moderate degree of starbursting. The analysis of the correlation between the B band and IRAS fluxes confirms what we found in the previous chapter, namely that while the nuclei largely dominate the 12 μm emission, the galaxies are the major contributors at $\lambda \geq 60\mu$m. The main source of difference in the 0.4–12 μm broad band SED seems to be a variable amount of internal reddening, up to $A_V \sim 1.5$ in our sample objects. Cheng et al. (1983) suggested a strict correlation between the internal reddening of the nuclei and the axial ratio of the hosting galaxy. Our study do not confirm this idea. This can be due either to large variations of the optical properties of the absorbing layer, or to the fact that it does not lie in the equatorial plane of the galaxy. The correlation between the optical and the X–ray emission is found stronger than that between the near–IR and the X–ray. The analysis of the partial correlation suggests that the latter can be induced by the former and by the strong correlation between the optical and the IR.

4.1 Introduction

As already stressed in many occasions, in order to study the SED of AGNs, in particular those of moderate luminosity such as Sy 1 nuclei, it is very important to disentangle the nuclear from the galactic contribution to the observed flux in the spectral regions where the host galaxy emits significantly. Here we present our work in this direction for the optical bands, together with a preliminary discussion of the results. Contrary to the infrared case (previous chapter), for which we have presented a discussion in a rather definitive form, our work on the optical results is still in progress, and the corresponding discussion reported here is far from complete.

4.2 Observations

We concentrated our observations on the optically selected *homogeneous* sample of 56 Seyfert 1 and 1.5 galaxies defined by Cheng et al. (1985), when deriving the Optical Luminosity Function of low luminosity AGNs, which we have described in Chapter 2. We observed 45 Seyfert 1 galaxies with the CCD camera (Bregoli et al. 1990) on the Loiano 1.5m telescope. Four of these objects (III Zw 2, VII Zw 118, Mkn 876 and Mkn 877) do not belong to the homogeneous sample, but they are nevertheless included in the following discussion. For 37 objects we have got frames in all the three BVR bands, while for the reminder we have only B and R observations. The frames have size of 512×321 pixels with a scale of $0.50''$/pix and have been calibrated, after a standard reduction (correction for linearity, background subtraction, flat-fielding correction), using standard observations.

4.3 Data Analysis

Our scope in analyzing imaging data is to obtain reliable determinations of nuclear fluxes and of the main characteristics of the galaxies hosting the AGNs, such as their total luminosity, the relative importance of the bulge and the disk components and the morphological parameters. The analysis procedure that we have developed for this purpose is described in Chapter 2. Here we add a discussion concerning the uniqueness of the final solution, a problem that we have carefully addressed for the optical data.

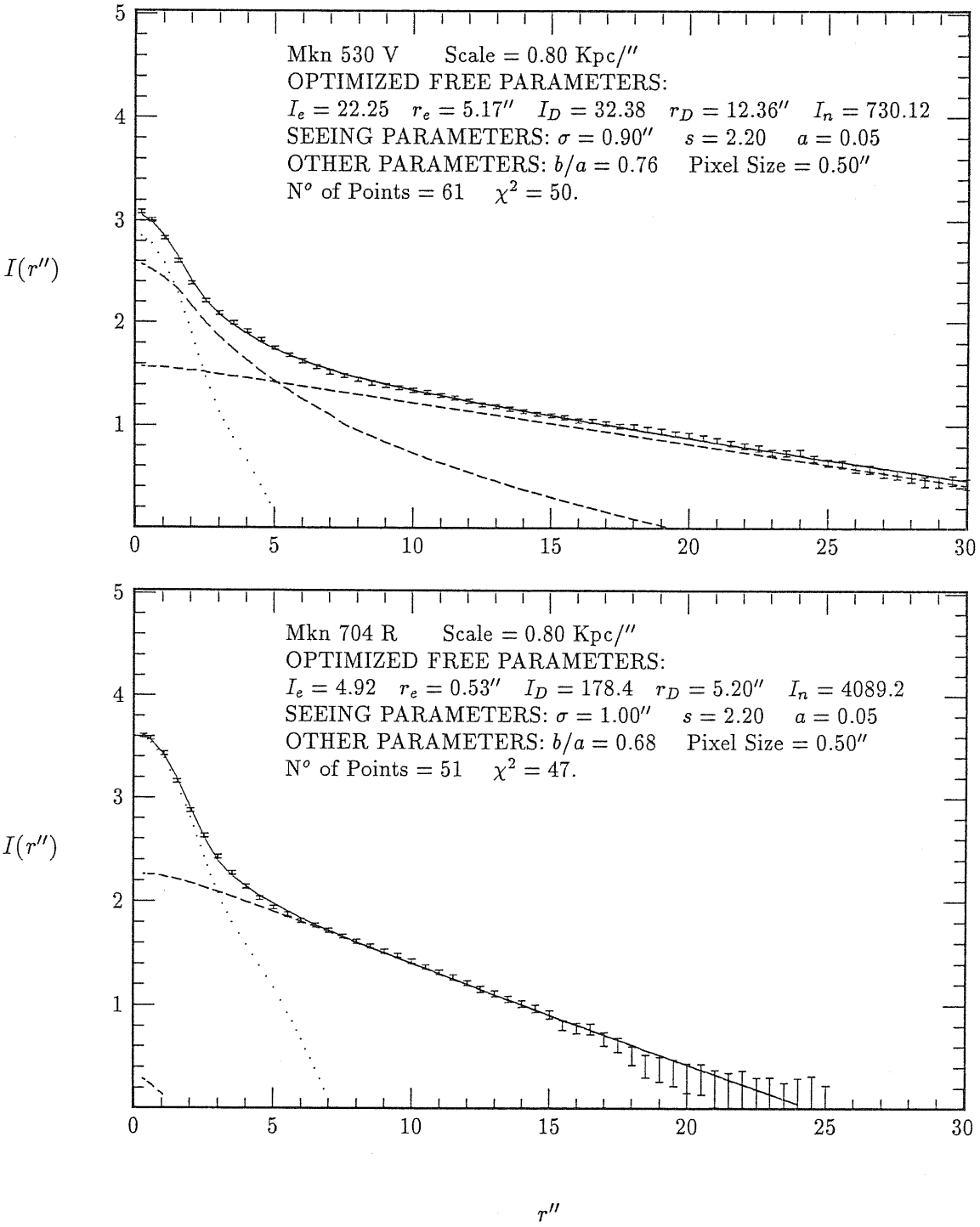

Figure 4.1: Intensity profile data (arbitrary units) and fits for two objects. The relevant parameters are shown in the panels. The global best fits (solid lines), the nuclear (dotted), the bulge (long–short dashed), and disc profiles (dashed) are reported.

4.3.1 Uniqueness of the Solutions

Given the high number of parameters to be determined, it is natural to suspect that in the space of parameters there can be many local minima, from which it could be impossible to single out the "true" solution. Indeed, we have found that the situation is usually not so dramatic because the many parameters are not very correlated. In other words, there are usually well defined regions in the profile, in which the agreement between the model and the observation is determined by only one among the three components, and this circumstance strongly constraints the possible values of its parameters (see figures 4.1). In fact the very inner region, say interior to $r = 2''$, is almost invariably dominated by the PFS of the pointlike nucleus (the mean σ used in our optical fits is $0.95 \pm .22$ (s.d.)), while outside about $10''$ the profile is determined by the exponentially decreasing disk. Therefore these extreme regions provide very often strong constraints on the contribution of the nucleus and the disk. The intermediate region is characterized by a more complex and variable behavior, because here the possible importance of the bulge shows itself, but the other two components are usually not negligible. In many cases there is no place in the profile where the bulge is the main component, but nevertheless its presence remains necessary to obtain a good fit in this intermediate region. In such circumstances we have noticed trough many tests that the parameters r_e and I_e are not well determined singularly, while their combination $I_e r_e^2$, which is proportional to the luminosity of the bulge, is much better constrained. In other words, when, as often is the case, the bulge is a detectable but nowhere a dominant component, we can obtain equivalently good fits by varying the single bulge parameters by as much as 100%, but the corresponding bulge luminosities are determined within less than say 15%. This is somehow analogous to what already reported by other authors, either when dealing with profiles of normal galaxies (e.g. Kent 1985), or those of active galaxies (Malkan 1984; Veron-Cetty and Woltjer 1990). We explicitly note that an uncertainty of this kind in the bulge luminosity is reflected in a much lower uncertainty in that of the nucleus, less than 5%, because it is in large part absorbed by the disk component. There are of course also cases in which the bulge is negligible or, at the other extreme, so important that the individual parameters are well constrained, but the more common situation is the one we have described above.

In conclusion the nuclear and disk parameters, as well as the bulge luminosity when not negligible, are usually well determined quantities, while the single bulge parameters can be more uncertain. This difficulty to characterize the bulge component has forced other authors (Yee 1983; MacKenty 1990) to give up its determination. But we can expect that in early type spiral galaxies, such as Seyfert hosts are thought to be, the bulge can give a significant contribution to the brightness in

the nuclear region, which must be taken into account if we want to obtain a good estimate of the magnitude of the active nucleus. With the aid of better quality data and/or a more careful analysis method, we are able here at least to determine the role of the bulge in the luminosity budget of our frames, and sometimes also to say something about its morphology.

4.3.2 Results

In table 4.1 we have reported the main outputs of our fits: for each object observed, the magnitude in the three bands of the pointlike nucleus and of the galactic component (within a radius of 60 Kpc), the fraction $b/t(R)$ of the galactic luminosity due to the bulge, the central surface brightness of the disk $\mu_D(B)$, the effective radius of the bulge $r_e(R)$ and the disk scale length $r_D(R)$.

We have reported the values obtained from the R frames for b/t, r_D and r_e, because in this band the galaxy, and particularly the bulge, is more easy to characterize, while for μ_D we have chosen the value in B because more directly comparable with the previous literature, in particular that regarding non-active galaxies.

The magnitudes have been corrected for the galactic extinction using the values of E_{B-V} given by Cheng et al. 1985 and reported in the table. No K-corrections have been applied, so that the results refer to the observer's frame. On the other hand, owing to the relatively low redshifts of the galaxies, such corrections are largely negligible with respect to the typical uncertainty.

4.3.3 Uncertainty

We have estimated the final uncertainty in the our magnitudes in many different ways.

We have collected 18 repeated observations, that is objects observed more than once in the same band but in different nights. When comparing the results of these multiple observations, we must take into account the fact that usually an observation was repeated when something was suspected to have gone wrong in the first trial, or at least not very well. For the nucleus, we have also to remember the "noise" due to its possible variability. Anyway, the mean absolute discrepancy in the repeated observations is 0.22 mag. for the galaxy and 0.25 for the nucleus.

Yee (1983) reports host magnitudes in the V band obtained from its fits, within a radius of 17.6 Kpc. For the 9 objects in common with our sample we have computed these magnitudes using our fits, and the mean difference we have found is -0.02 ± 0.29 (sd). The agreement is therefore quite good, especially if we take into account that Yee has observed in the r g v bands of Thuan and Gunn (1976), and the V

Name	z	E_{B-V}	b/a	B_n	V_n	R_n	B_g	V_g	R_g	$B/T(R)$	$\mu_D(B)$	r_e	r_D
0048+29	.036	.00	.60	16.74	...	15.44	15.09	...	13.82	.24	21.94	1.10	6.95
1503	.036	.01	.48	16.82	...	15.58	15.35	...	13.80	.27	22.92	5.16	9.42
2237+07	.025	.00	.71	17.66	17.00	16.30	15.57	14.70	14.14	.19	20.54	...	2.58
I Zw 1	.061	.03	.96	14.40	14.04	13.63	15.75	15.16	14.41	...	21.74	...	9.06
II Zw 1	.054	.01	.93	17.61	16.97	16.27	15.92	15.33	14.63	...	20.64	...	3.88
III Zw 2	.090	.04	.90	15.65	...	15.04	17.07	...	15.78	<0.1	21.91	...	6.30
Mkn 006	.018	.08	.50	16.27	15.50	14.81	15.26	14.54	13.81	.55	...	7.40	...
Mkn 009	.040	.03	.98	15.85	15.27	14.85	14.78	14.31	13.78	.36	21.81	4.64	4.55
Mkn 010	.029	.03	.54	16.11	15.72	15.11	13.89	13.31	12.78	.12	22.24	2.29	10.67
Mkn 079	.022	.06	.57	15.08	14.95	14.64	13.57	13.07	12.60	.26	22.54	.89	8.20
Mkn 141	.039	.02	.86	16.00	15.63	15.16	15.52	14.75	14.16	.27	21.14	11.21	3.71
Mkn 231	.041	.01	.80	14.78	14.03	13.45	14.15	13.62	13.11	.52	21.93	2.76	7.17
Mkn 279	.031	.02	.68	14.91	...	14.17	14.52	...	13.44	.32	21.94	1.57	6.32
Mkn 290	.031	.01	.97	15.81	15.29	14.81	16.25	15.36	14.81	<0.1	21.59	...	3.26
Mkn 304	.067	.05	.95	15.30	14.90	14.64	16.47	15.13	14.86	.65	21.70	7.24	4.54
Mkn 335	.025	.03	.80	14.31	13.92	13.79	15.42	15.30	14.73	<0.1	20.72	2.95	2.11
Mkn 352	.025	.03	.92	15.48	15.15	14.78	15.55	14.87	14.16	<0.1	20.64	...	1.51
Mkn 359	.017	.01	.86	16.59	16.30	15.91	14.53	13.82	13.26	.37	20.30	1.14	2.11
Mkn 372	.031	.10	.82	17.61	16.78	16.38	15.12	14.24	13.69	.38	21.06	2.30	3.65
Mkn 376	.056	.09	.69	14.57	14.27	14.11	15.00	14.68	14.06	<0.1	19.85	...	5.06
Mkn 478	.079	.00	.88	14.84	14.47	14.28	16.75	16.10	15.53	<0.1	22.38	...	7.08
Mkn 486	.039	.01	.85	15.04	14.95	14.25	...	...	16.73	<0.1	...	...	3.00
Mkn 506	.043	.03	.67	16.48	15.82	15.37	15.23	14.30	13.74	<0.1	21.55	...	7.53
Mkn 509	.036	.04	.86	14.32	14.00	13.47	15.48	14.57	14.06	.45	23.22	1.29	7.09
Mkn 530	.029	.03	.76	16.12	15.90	...	14.00	13.41	...	.36	22.10	3.98	9.85
Mkn 584	.078	.00	.91	17.71	17.28	16.91	16.19	15.49	14.69	.22	20.80	...	6.79
Mkn 590	.027	.00	.92	15.35	...	14.36	13.86	...	12.55	.61	23.07	8.18	12.14
Mkn 595	.028	.00	.69	17.21	16.42	15.89	14.68	13.79	13.24	.17	...	3.66	...
Mkn 618	.034	.05	.59	14.70	14.40	14.03	14.49	13.85	13.32	<0.1	20.62	...	5.88
Mkn 668	.079	.00	.71	17.30	...	16.13	15.20	...	14.03	.32	22.51	8.72	16.94
Mkn 704	.029	.01	.68	15.16	14.77	14.25	15.65	14.76	14.25	<0.1	21.65	...	4.16
Mkn 705	.028	.01	.87	15.99	15.83	15.52	14.57	13.99	13.65	.42	23.13	.83	6.64
Mkn 734	.050	.01	.75	15.50	15.18	15.03	...	15.48	15.08	.52	...	3.13	11.45
Mkn 766	.013	.01	.81	15.78	15.00	14.28	13.76	13.30	12.49	.35	21.35	2.21	3.07
Mkn 817	.032	.01	.95	...	14.40	14.05	...	14.25	13.74	<0.1	...	...	4.11
Mkn 841	.036	.00	.90	15.18	14.95	14.65	...	...	...	.46	...	2.37	...
Mkn 871	.034	.03	.40	16.98	16.71	16.03	14.99	14.35	13.63	.26	21.69	2.57	6.39
Mkn 876	.129	.02	.91	15.33	...	14.82	16.77	...	15.17	.30	22.83	...	9.97
Mkn 877	.115	.03	.91	16.14	15.84	15.74	17.48	...	17.62	...	25.77	...	8.28
Mkn 975	.050	.04	.66	16.43	15.81	15.46	15.32	14.81	14.39	.41	22.60	...	12.54
Ngc 3516	.009	.02	.81	15.06	14.82	14.25	12.48	11.75	11.00	.67	22.87	1.94	7.81
Ngc 5548	.019	.00	.82	14.98	14.44	14.10	13.76	13.04	12.71	.44	21.27	3.62	3.99
Ngc 5940	.034	.00	1	16.85	16.24	15.60	14.14	13.56	12.96	<0.1	20.75	...	7.20
Ngc 7469	.017	.03	.75	14.20	13.75	13.27	13.69	12.94	12.41	.14	20.46	1.07	3.18
VII Zw 118	.080	.04	.91	...	15.30	15.02	...	15.22	14.68	...	...	4.08	...

Table 4.1: Main outputs of our optical fits.

magnitudes he reports are obtained using an average transformation law.

Cheng et al. (1985), using a collection of heterogeneous photometric data taken from the literature, and by applying two raw correction methods (the "color given" and "galaxy given" methods), computed the B nuclear magnitudes for all the objects in our sample, with an estimated error of 0.5 mag. The mean difference between our magnitudes and those given by Cheng is $.19 \pm 0.76$ (sd) for the color given method and 0.49 ± 0.75 for the galaxy given method. The large dispersion of these discrepancies is clearly connected to the crude assumptions made in these methods. The relatively large systematic shift between our results and those of the galaxy given method is easy to explain: that method consists in fact in subtracting to the observed magnitude the fixed contribution of a template host galaxy. Cheng has taken $M_B = -21$ for the total absolute magnitude of the galaxy, while we have found from our fits an average of $M_B = -21.55$.

MacKenty (1990) has collected CCD frames in BVR for a sample of 51 Seyfert galaxies, fitting the external regions of 39 of them with an exponential disk model. We have data for twelve objects in its sample. As a consistency check, we compared the galactic colors derived from our fits, to those computed by MacKenty integrating in the annulus between 7.5 and 15 Kpc in radius, in which the contribution from the nucleus is negligible. The mean difference from our colors is -0.09 ± 0.20 (s.d.) in $B-V$ and 0.03 ± 0.13 (s.d.) in $V-R$. We have also computed the mean fractionary difference between the disk scale lengths in our fits and those obtained by MacKenty, $< \delta r_D/r_D >= 0.09 \pm 0.29$ (s.d.).

In view of the above considerations, we believe that 0.2 mag. is a honest conservative evaluation of the typical uncertainty in the magnitudes we have reported, which takes into account, for the nucleus, also of the noise due to variability.

	Seyfert		Non-active $0 \leq T \leq 4$		
Parameter	Mean $\pm$ s.d.	Median	Mean $\pm$ s.d.	Median	P_{KS}
$\mu_D(B)$	21.78 ± 1.08	21.72	21.67 ± 0.88	21.67	0.98
$b/t(R)$	0.36 ± 0.15	0.36	0.40 ± 0.22	0.36	0.90
r_D	6.49 ± 3.33	6.39	6.67 ± 3.94	5.06	0.90
r_e	3.64 ± 2.72	2.76	4.17 ± 2.86	3.34	0.80

Table 4.2: Comparison between the morphological parameters of Seyfert hosts and those of a sample of non active galaxies.

4.4 Discussion

4.4.1 Morphology of the Host Galaxies

The morphologies of Seyfert galaxies have been studied by many authors, either in a qualitative (Adams 1977; Simkin et al. 1980) or more quantitative way (Yee 1983; MacKenty 1990). The general well know conclusion is that the large majority of Seyfert nuclei reside in early type spirals or S0 galaxies. These studies have also put in evidence a rather generalized presence of disturbed morphologies and/or bars (see MacKenty 1990 and references therein).

Here we are mainly interested in comparing, in a quantitative way and for our large sample of objects, the morphological parameters derived from our fits to those derived in analogous studies of samples of non-active spiral galaxies (Freeman 1970; Boronson 1981; Kent 1985). We have chosen as main reference for this comparison the work done by Kent, because he presents data on the richest and better defined sample. We have extracted from it the subsample of 38 galaxies having morphological type $0 \leq T \leq 4$, and compared the distributions of $b/t(R)$, r_D, $\mu_D(B)$ and r_e in this and our sample by using the standard Kolmogorov-Smirnof (KS) test. The observed distributions of these parameters in our sample are shown in figure 4.2, 4.3, 4.5, and 4.4. Since Kent's result refers to the r band of Thuan and Gunn (1976), the bulge to disk ratios can be compared directly to ours, as determined in the R band, without any practical need of color correction. When comparing the distributions of b/t ratios, we have excluded in both samples the objects with $b/t < 0.1$, because we feel that below this limit our procedure becomes usually quite insensitive to the bulge contribution. We have reported to the B band the values of the disk central surface brightness derived by Kent, using the approximate conversion $B \simeq r + 0.9$ given by himself, and valid for spiral galaxies.

The results are summarized in Table 4.2. As can be seen, there is a well defined

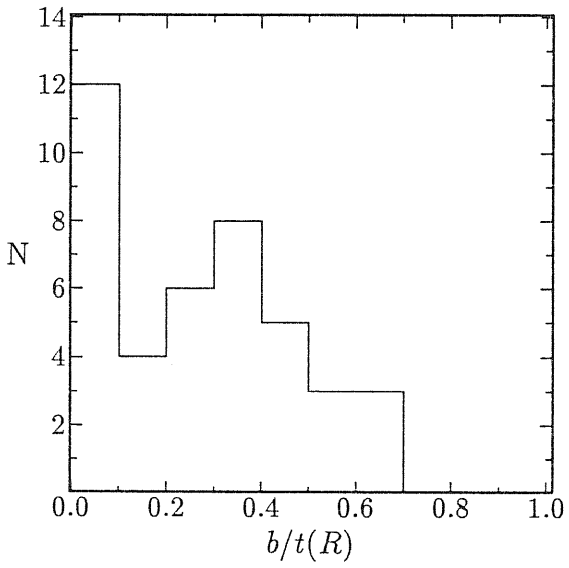

Figure 4.2: Distribution of $b/t(R)$ in our sample.

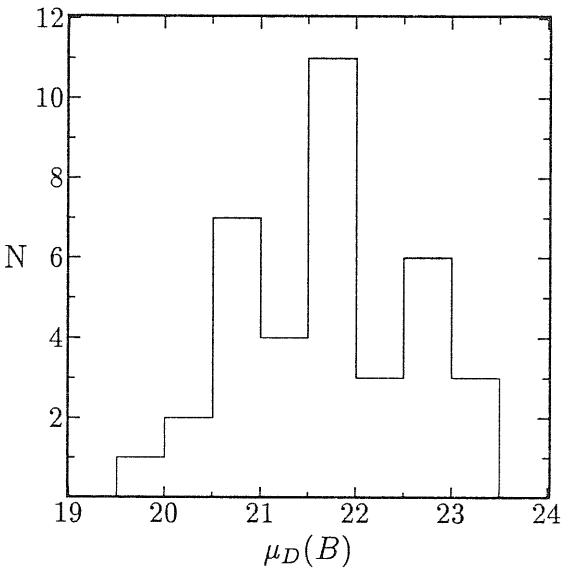

Figure 4.3: Distribution of $\mu_D(B)$ in our sample.

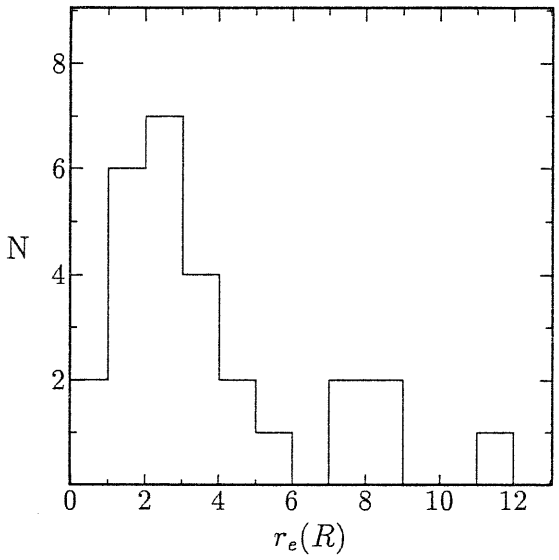

Figure 4.4: Distribution of $r_e(R)$ in our sample.

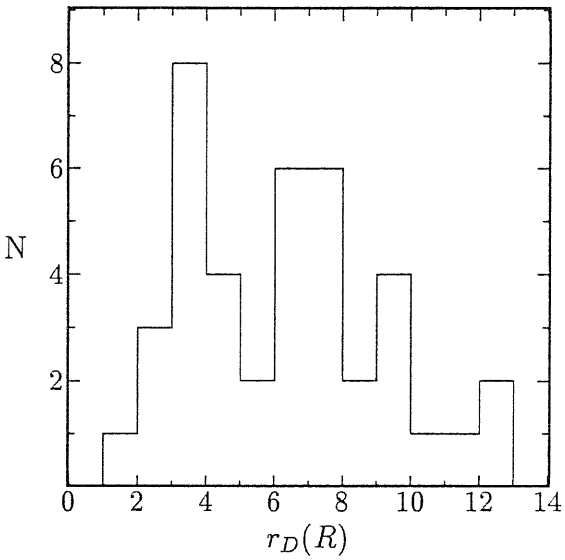

Figure 4.5: Distribution of $r_D(R)$ in our sample.

	Seyfert		Non-active $0 \leq T \leq 4$		
Parameter	Mean $\pm$ s.d.	Median	Mean $\pm$ s.d.	Median	P_{KS}
$(B-V)_g$	0.68 ± 0.22	0.67	0.82 ± 0.13	0.85	10^{-4}
$(V-R)_g$	0.57 ± 0.13	0.55	0.79 ± 0.12	0.79	10^{-10}
$(V-K)_g$	3.47 ± 0.59	3.48	3.29 ± 0.34	3.16	0.13

Table 4.3: Comparison between the optical colors of Seyfert hosts and those of a sample of non active galaxies.

statistical evidence that the observed distributions of the morphological parameters in non-active early type spiral and in Seyfert 1 galaxies are drawn from the same population. We note also that the major differences between correspondent distributions arise in the parameter r_b, which we think to be that plagued by the largest uncertainties among those examined.

The mean central surface brightness of the disk in our Seyfert sample, $\mu_D(B) = 21.78 \pm 1.08$ mag arcsec^2 (s.d.), is also in very good agreement with the values 21.65 given by Freeman (1970) and 21.79 ± 0.78 by Boronson (1981) for normal spiral galaxies. Yee (1983) suggested that Sy galaxies might have a central surface brightness higher than normal spirals, having found an average value of 21.3 even without corrections for inclination, and 21.0 if an average b/a was considered. By converse, MacKenty (1990) found, as we do, a value close to that of normal spirals, namely 21.9. We agree with the explanation given by MacKenty, but already suggested by Yee itself, for the origin of Yee's result: he was forced by the lower quality of its data to neglect the bulge contribution to the profiles, while fitting them in regions where it can be important. MacKenty, who also neglected the bulge, has found a value in agreement with us because he used the very outer regions of the profiles, where indeed the profiles of spiral galaxies are usually largely dominated by the disk (see for instance the plots in Boronson 1981 or Kent 1985).

In conclusion we see that the morphological parameters of the galaxies hosting Sy 1 nuclei do not show any statistical difference with respect to that of non active early type spirals.

4.4.2 Colors of the Host Galaxies

Yee (1983) compared the integrated colors of Seyfert host to those of normal galaxies of the same morphological type, finding that while there is not a clear difference when considering Sy 1 and Sy 2 together, galaxies hosting Seyfert 1 nuclei might be

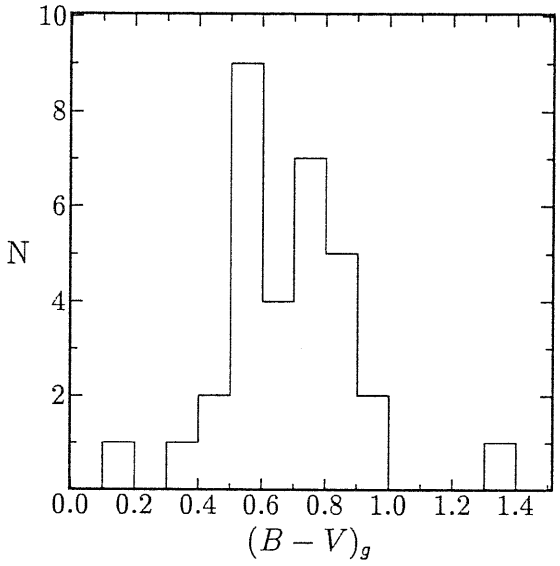

Figure 4.6: Distribution of $(B-V)_g$ in our sample.

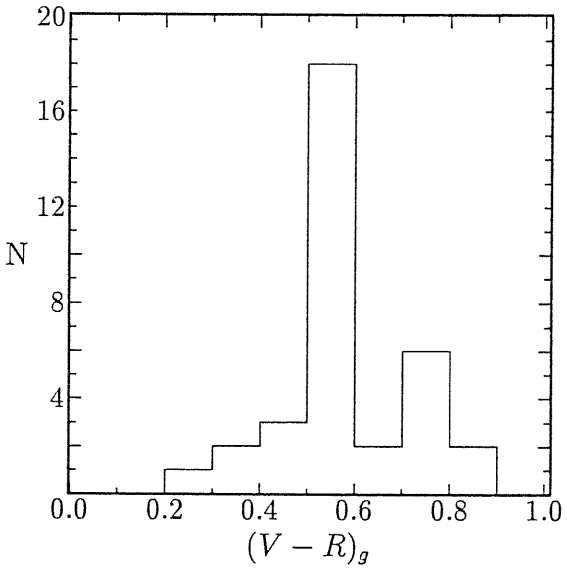

Figure 4.7: Distribution of $(V-R)_g$ in our sample.

slightly bluer than early type spiral galaxies, but the result was very uncertain due to the rather poor statistic (only 9 objects).

We have carried out a similar comparison between the distributions of the galactic colors of our active galaxies (Fig. 4.6 and 4.7) and those of normal early type spirals, using the data collected by Marsiaj (1991) . Table 4.3 reports the result. In contrast with the previous situation, here we see that the optical $(B-V)_g$ and $(V-R)_g$ colors of the galaxies hosting Seyfert activity are slightly (about 0.2 mag), but clearly, bluer than those of non active galaxies of the same morphological type. Indeed, the probability given by the KS test that the two distributions are drawn from the same population is negligible. More similar seem to be the distributions of the optical-IR color $(V-K)_g$, obtained combining the magnitudes presented here with those reported in the previous chapter. We noticed there that the IR colors of our sample galaxies seem to be slightly redder than those of normal early type spirals. All these facts together tend to suggest that the galaxies hosting Seyfert nuclei could be sites of a mild form of starbursting, like that observed in non-Seyfert Markarian galaxies, possibly linked to the nuclear activity and/or to the observed increased frequency of disturbed morphologies or bars (MacKenty 1990 and references therein). In order to check this hypothesis we compared our observed distribution of $(B-V)_g$ also to that of the "morphological sample" of non-Seyfert Markarian defined by Huchra (1977), confining ourselves to objects classified as having $0 \leq T \leq 4$. The mean $(B-V)_g$ in that sample is 0.65 ± 0.11 (s.d.) while the median is 0.67, in practise identical to the corresponding quantities in our sample, and indeed the KS test yields a probability that the two distributions are drawn from the same parent population $P_{KS} = 30\%$.

4.4.3 Luminosities of the Host Galaxies

The luminosity distributions of the host galaxies are shown in Figs. 4.8, 4.9 and 4.10. We find $< M_{Bg} >= -21.54 \pm 0.76$ (s.d.), $< M_{Vg} >= -22.14 \pm 0.73$ and $< M_{Rg} >= -22.69 \pm 0.85$: the galaxies in our sample appear to be quite bright, being drawn from the high luminosity "exponential tail" of the luminosity function (the characteristic magnitude in the Schechter formula is $M_{*B} = -20.78$ according to Felten 1977).

Yee (1983) has found $< M_{Vg} >= -21.5 \pm 0.8$ within a radius of 17.6 Kpc for 20 Seyfert galaxies. Integrating within the same galactic region, we find in our sample $< M_{Vg} >= -21.70 \pm 0.80$, in reasonable agreement with Yee's result. More uncertain is the comparison with the luminosity of galaxies hosting higher redshift AGNs, mainly because in such objects the results are more model dependent, but also because there could be a significant contribution from extended line emission. In works dealing with higher redshift samples, a distinction between Seyfert nuclei and

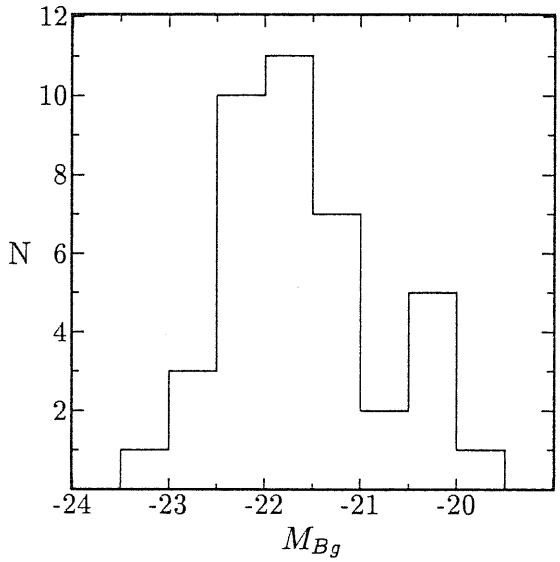

Figure 4.8: Distribution of M_{Bg} in our sample.

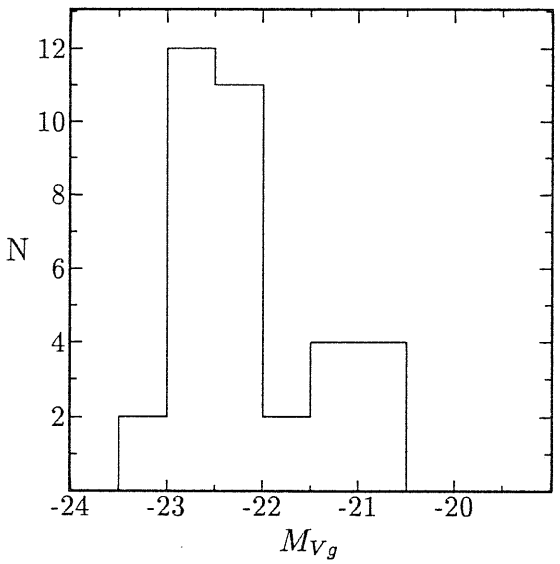

Figure 4.9: Distribution of M_{Vg} in our sample.

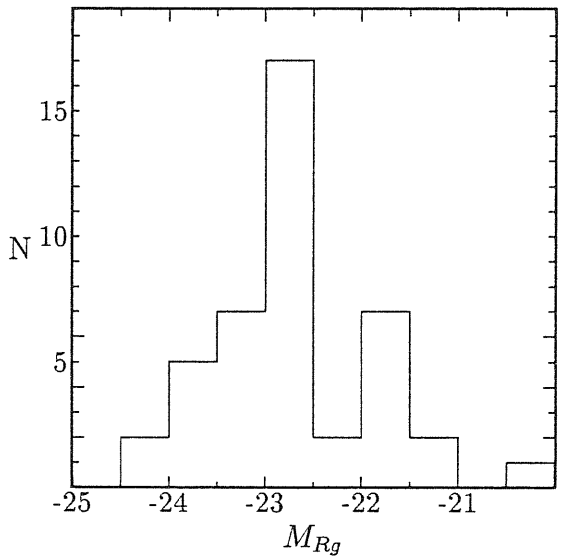

Figure 4.10: Distribution of M_{Rg} in our sample.

QSOs is generally made on the usual criterium that an AGN should have a nuclear luminosity brighter than $M_{Bn} = -23$ to be dignified as "true" QSO. According to the nuclear magnitudes we have derived with our procedure, only four objects in our sample (marginally) satisfy this criterium, though 15 objects are known as PG-QSOs. The sample is therefore essentially a Seyfert sample, as long as this distinction is to be considered meaningful.

Smith et al. (1986) have presented the luminosity distribution of 89 galaxies hosting AGNs, finding a mean absolute blue magnitude, within the isophote at 25B mag arcsec^{-2}, of $< M_{Bg} >= -21.8$ for 22 radio quiet QSOs, and $< M_{Bg} >= -20.9$ for 20 Seyfert hosts. Within the same isophote, we find from our fits $< M_{Bg} >= -21.29$ (the light from outside the 25B mag arcsec^{-2} contribute on average for 0.25 mag in our galaxies); Veron-Cetty and Woltjer (1990) found in the V band an average (total) absolute magnitude $< M_{Vg} >= -22.3$ for radio quiet QSOs and $< M_{Vg} >= -21.3$ for galaxies hosting Sy 1 nuclei. We explicitly note that the QSOs for which the fuzziness can be measured are relatively low redshift, low luminosity objects, thus it is not surprising that their host galaxies are found to be on average not much brighter than those of the more luminous Seyfert of our sample.

In conclusion we have found that the galaxies hosting Seyfert activity turn out to be very bright in comparison with non-active galaxies, having typical luminosities slightly higher than those found from other authors in Seyfert samples, and maybe

Parameter	N	Mean $\pm$ s.d.	Median
M_{Bn}	43	-20.83 ± 1.48	-20.68
M_{Vn}	38	-21.22 ± 1.40	-21.20
M_{Rn}	44	-21.78 ± 1.32	-21.70
M_{Kn}	40	-24.77 ± 1.16	-24.60
$(B-V)_n$	36	0.44 ± 0.20	0.38
$(B-R)_n$	42	0.89 ± 0.31	0.85
$(B-K)_n$	29	4.14 ± 0.66	4.09

Table 4.4: Distributions of nuclear colors and magnitudes.

Values Correlated	P_{BHK}
$L_{0.4,n}$—L_{12}	3×10^{-5}
$L_{0.4,g}$—L_{12}	0.05
$L_{0.4,n}$—L_{25}	4×10^{-5}
$L_{0.4,g}$—L_{25}	0.03
$L_{0.4,n}$—L_{60}	4×10^{-3}
$L_{0.4,g}$—L_{60}	2×10^{-3}
$L_{0.4,n}$—L_{100}	0.01
$L_{0.4,g}$—L_{100}	7×10^{-4}

Table 4.5: Correlation between the 0.4μm and IRAS fluxes.

not much less than those found in radio-quiet low redshift QSOs.

In Chapter 3 we described the correlation between the 2.2μm luminosities of the nuclei and those of the galaxies, which is also apparent in the optical at 0.44μm (Fig 4.11), with a significance level of 0.994, a bit lower than that found at 2.2μm. As we noted there, the correlation is in part due to a selection effect, because our UVx sample is biased against low luminosity nuclei hosted in bright galaxies, while the tendency of bright nuclei to reside in bright galaxies is probably real.

4.4.4 Properties of the Nuclei

The observed distributions of nuclear absolute magnitudes and colors are plotted in Figs 4.12, 4.13 and 4.14, while in Table 4.4 we have reported a little of statistic concerning the same parameters. As we already noticed, though in our sample

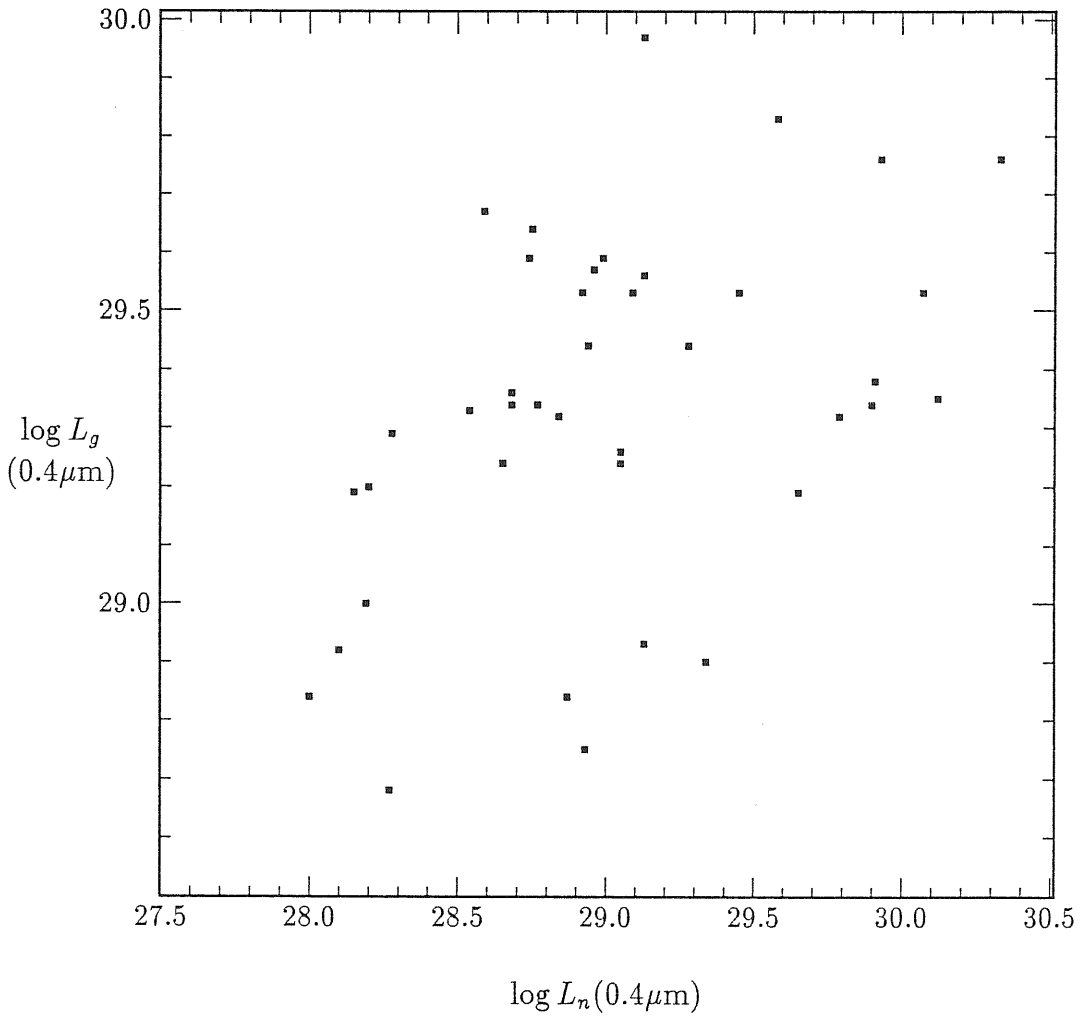

Figure 4.11: Correlation between the 0.4μm luminosities of the nuclei and those of the galaxies.

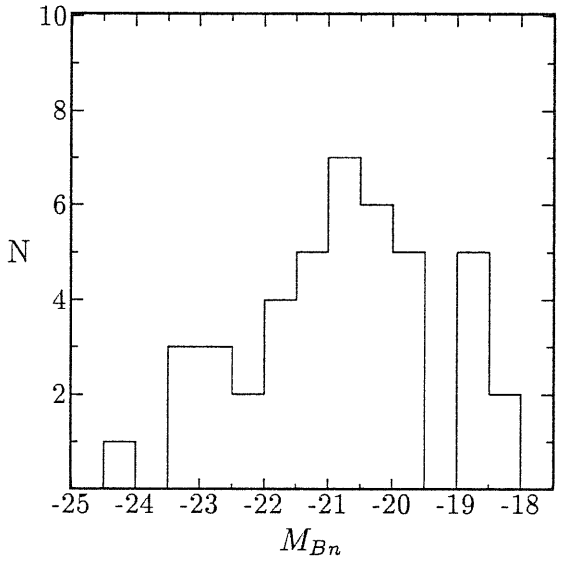

Figure 4.12: Distribution of M_{Bn} in our sample.

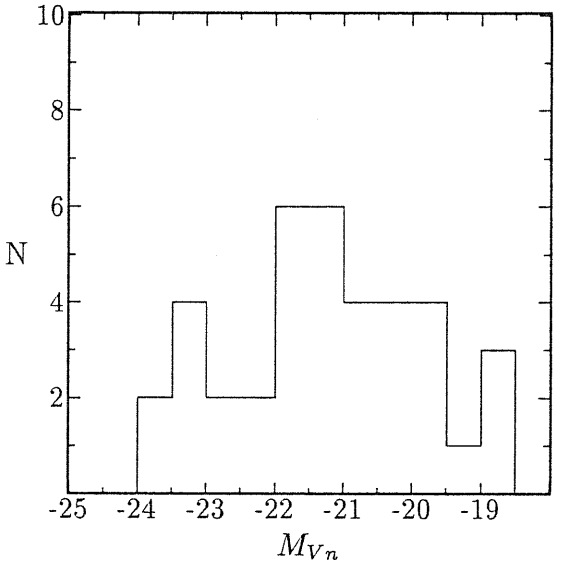

Figure 4.13: Distribution of M_{Vn} in our sample.

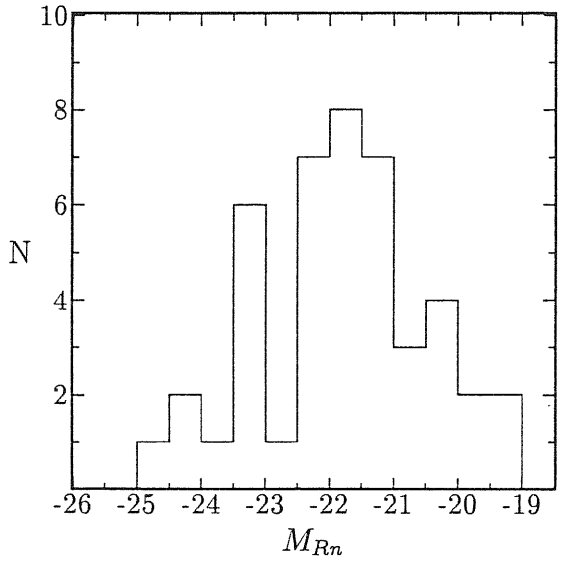

Figure 4.14: Distribution of M_{Rn} in our sample.

there are 15 low redshift PG-QSOs and 12 of them have been observed in the B band, only four of them (marginally) fulfill the condition $M_{Bn} < -23$, when the contribution of the host galaxy is taken into account according to our decomposition. The questionable distinction between Sy 1 nuclei and QSOs seems therefore very difficult to realize with raw photometric data, because at these levels of luminosity the host galaxy can contribute in a significant and misleading way to the photometry, even within small apertures.

In the previous chapter we have presented a detailed statistical analysis of the correlations of the nuclear and galactic K-band luminosities with those at the IRAS wavelengths. The conclusion was that while at 60 and 100 μm the emission is dominated by the diffuse galactic component, at 12 and 25 μm the observed IRAS flux is essentially due to the nucleus. A similar analysis of the correlation between the 0.4 μm and IRAS fluxes reinforces this statement. In Table 4.5 are reported the probabilities of reproducing the observed correlation by chance, as computed using the BHK test, a generalized version of the usual Kendall correlation test which takes into account also the upper limits in the observations (Schmitt 1985; Isobe et al. 1986). As apparent also from the Figs. 4.15 and 4.16a,b, the nuclear luminosity at 0.4 μm is very well correlated with that at 12 μm, with a probability of reproducing the correlation by chance $P_{BHK} = 3 \times 10^{-5}$, while the correlation between the 0.4 μm galactic luminosity and that at 12 μm is much weaker ($P_{BHK} =$

Values Correlated	P_k
$\frac{L_{Vn}}{L_{Bn}}$ — $\frac{L_{Rn}}{L_{Bn}}$	2×10^{-7}
$\frac{L_{Kn}}{L_{Bn}}$ — $\frac{L_{Rn}}{L_{Bn}}$	5×10^{-3}
$\frac{L_{12}}{L_{Bn}}$ — $\frac{L_{Rn}}{L_{Bn}}$	5×10^{-5}
$\frac{H_\alpha}{H_\beta}$ — $\frac{L_{Rn}}{L_{Bn}}$	0.62

Table 4.6: Correlations between some luminosity ratios (see text).

0.05), probably induced only by the observed correlation between the galactic and nuclear luminosities. By converse, the significance of the correlation with the 100 μm flux appears much weaker for the nucleus ($P_{BHK} = 0.01$) than for the galaxy ($P_{BHK} = 7 \times 10^{-4}$).

We have investigated the effects of the reddening on the continuum emitted by the nuclei with many "color–color" diagrams. In Fig. 4.17abc we present for instance plots of L_V/L_B vs. L_{Rn}/L_{Bn}, L_{Kn}/L_{Bn} vs. L_{Rn}/L_{Bn} and L_{12}/L_{Bn} vs. L_{Rn}/L_{Bn}, including reddening vectors corresponding to a maximum $E(B-V) = 0.5$. In Table 4.6 is reported the probability that the observed correlations among these ratios arise by chance, computed, when necessary, taking into account also of the limits.

The good correlations found between these "colors", and in particular the fact that the observed points tend to cluster along the reddening lines indicates that the nuclear SEDs can be described, at least in a first approximation, as a common intrinsic shape, reddened in a variable amount, up to $\sim$ 1.5 visual magnitudes. Stated in another way, the major source of differences among the broad band 0.4–12 μm SEDs of the objects in our sample seems to be a variable, and often quite large, amount of reddening. This result is in agreement with the findings of Carleton et al. 1987, except that those authors have found a still larger maximum reddening (up to $A_V = 3$). This difference is not surprising, provided that our sample is optically selected, and therefore the more heavily absorbed objects are missed, while that considered by Carleton et al. is dominated by members of an hard X–ray selected sample.

A similar plot for the Balmer decrement in the BLR (BDB) vs. the ratio L_R/L_B

(Fig. 4.17d) shows that the reddening expected from the steepness of the BDB is weakly correlated and larger than that expected from the "color". This is indeed what we expect to be the case, since it is currently widely concluded that the steepness of the Balmer decrement in the BLR is only in part due to reddening, the reminder part being ascribed to collisional and self-absorption effects (Shields 1974).

Cheng et al. (1983) have studied the behavior of the color of Sy 1 as a function of the axial ratio, with the aim of investigating the spatial distribution of the absorbing layers, and derive a recipe to correct the observed magnitudes for the effects of internal extinction. They found that the more powerful objects tend to cluster, in the $(B-V)$—b/a plane, along a line well described by the functional form appropriate to the case of a thin uniform absorbing layer in the equatorial plane of the galaxy, and, since they used magnitudes including the emission from the host galaxy, they concluded that the observed dispersion of the data points in the plane was due to the host contamination, and that Sy 1 nuclei should be embedded in an equatorial absorbing layer, with optical properties virtually independent of the galaxy under consideration, so that the observed magnitudes could be corrected for internal extinction using the law $E(B-V) = 0.15 + 0.25(a/b - 1)$. Our results do not confirm this conclusion: if we plot our $(B-V)_n$ colors of the bare nuclei against the axial ratios of the hosts (Fig. 4.18) we find, for a given value of b/a, a dispersion very similar to that observed in Fig. 1 of Cheng et al. (1983), and the points do not show any correlation. Since our colors are not contaminated by the host, the source of this dispersion must be found elsewhere. Possible explanation can be one or more of the following: (i) the intrinsic colors of the nuclei can vary widely from object to object (ii) the optical properties of the absorbing layers are very different from galaxy to galaxy or (iii) they do not lie in the equatorial plane. Since our previous considerations tend to exclude a large dispersion of the intrinsic colors of the nuclei (before absorption), we favor (ii) and/or (iii).

In Chapter 3 we have discussed the relation between the IR and X–ray nuclear emissions, suggesting that the positive correlation found in our and other samples between them does not necessarily imply that the IR emission is nonthermal, as often has been argued, but instead that both the IR and the X–ray continuum are powered by the same optical-UV primary continuum. Indeed, the correlation of the 2 keV and 0.4μm fluxes (B band) is more than one order of magnitude stronger than that found between the 2 keV and the 2.2μm fluxes, and the same is true for the luminosities (Fig. 4.19). The Kendall's rank test gives a probability $P_k = 1.4 \times 10^{-3}$ that the correlation of the fluxes is spurious. As for the luminosities, the probability of a spurious correlation falls to 5×10^{-5}. Therefore, the weaker correlation between the X–ray and IR can well be induced by those between the X–ray and the optical and between the optical and the IR. Indeed, we find from our

data a very strong correlation between the 0.4 and 2.2μm luminosities ($P_k = 10^{-7}$). In order to check this possibility we have considered the subsample of 26 objects for which we have both derived nuclear 2.2 μm fluxes and also 2 keV fluxes are available. For 19 of them we have also 0.4 μm nuclear fluxes derived with our procedure. For the reminder 7 we have employed the B band magnitudes derived by Cheng et al. (1985). Using this data set we have computed the Spearman partial correlation coefficient $R_{x,y;z}$ (Macklin 1982) between $L(2.2\mu\text{m})$ and $L(2\text{keV})$, taking constant $L(0.4\mu\text{m})$. We have found that $R_{x,y;z}$ is only 0.02, which corresponds to a probability $P_{x,y;z} = 0.91$ that the correlation between $L(2.2\mu\text{m})$ and $L(2\text{keV})$ entirely arises from the $L(0.4\mu\text{m})$–$L(2\text{keV})$ and $L(0.4\mu\text{m})$–$L(2.2\mu\text{m})$ ones separately. By converse, in the case of $L(0.4\mu\text{m})$ and $L(2\text{keV})$, the probability of a completely induced correlation drops to 0.01. These results confirm our suggestion that the observed correlation between the IR and X–ray emissions is induced by the optical–UV emission.

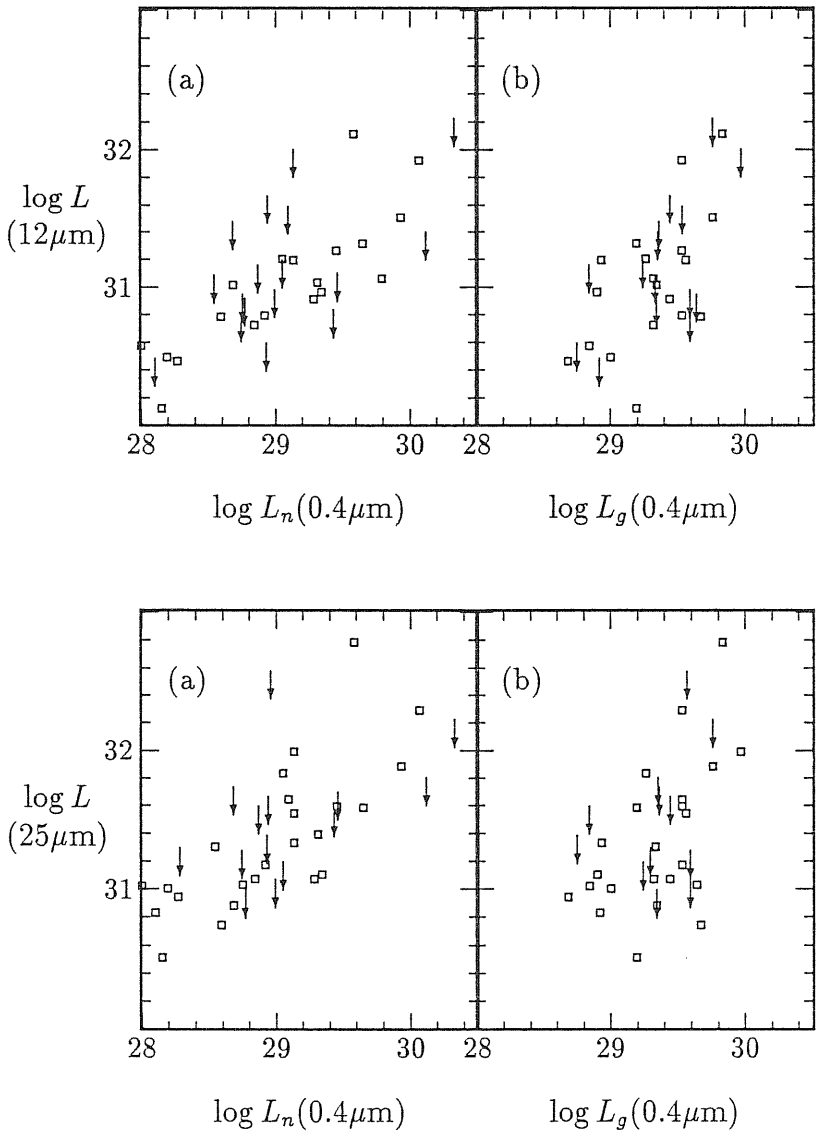

Figure 4.15: IRAS 12 μm and 25 μm luminosities versus nuclear (panels a) or galactic (panels b) luminosities at 0.4 μm.

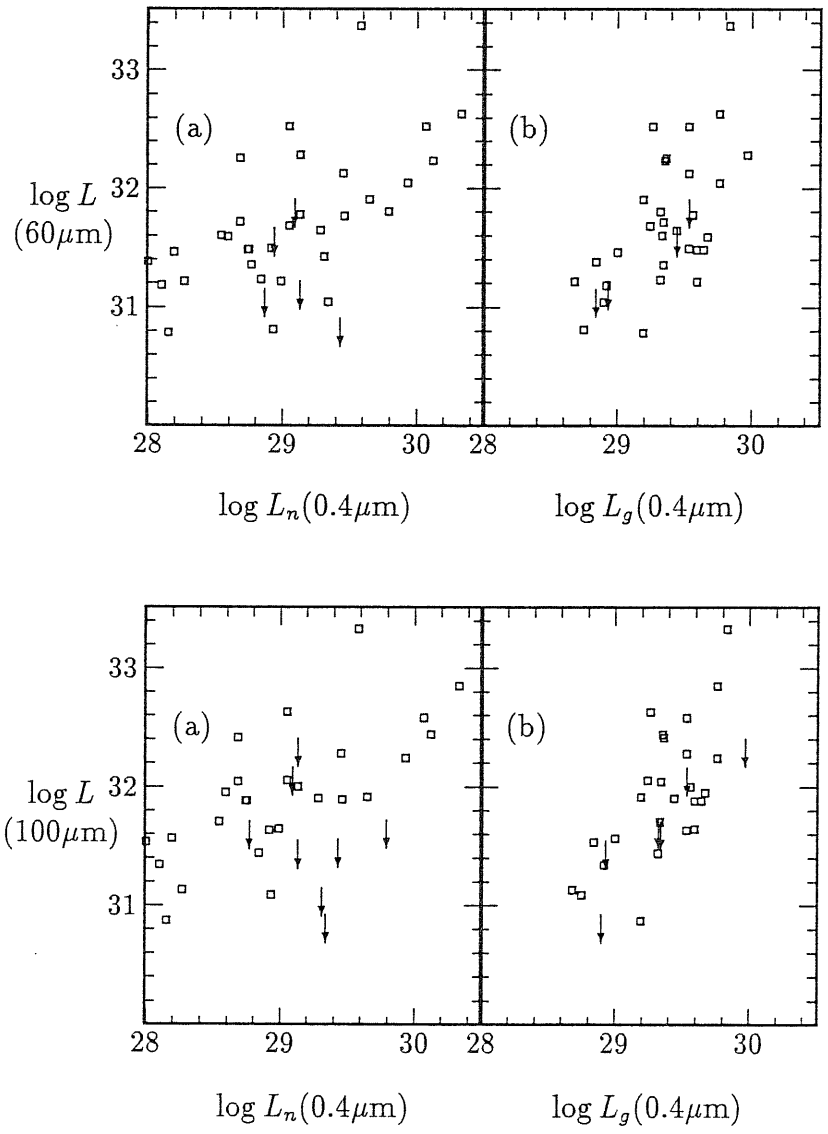

Figure 4.16: IRAS 60 μm and 100 μm luminosities versus nuclear (panels a) or galactic (panels b) luminosities at 0.4 μm.

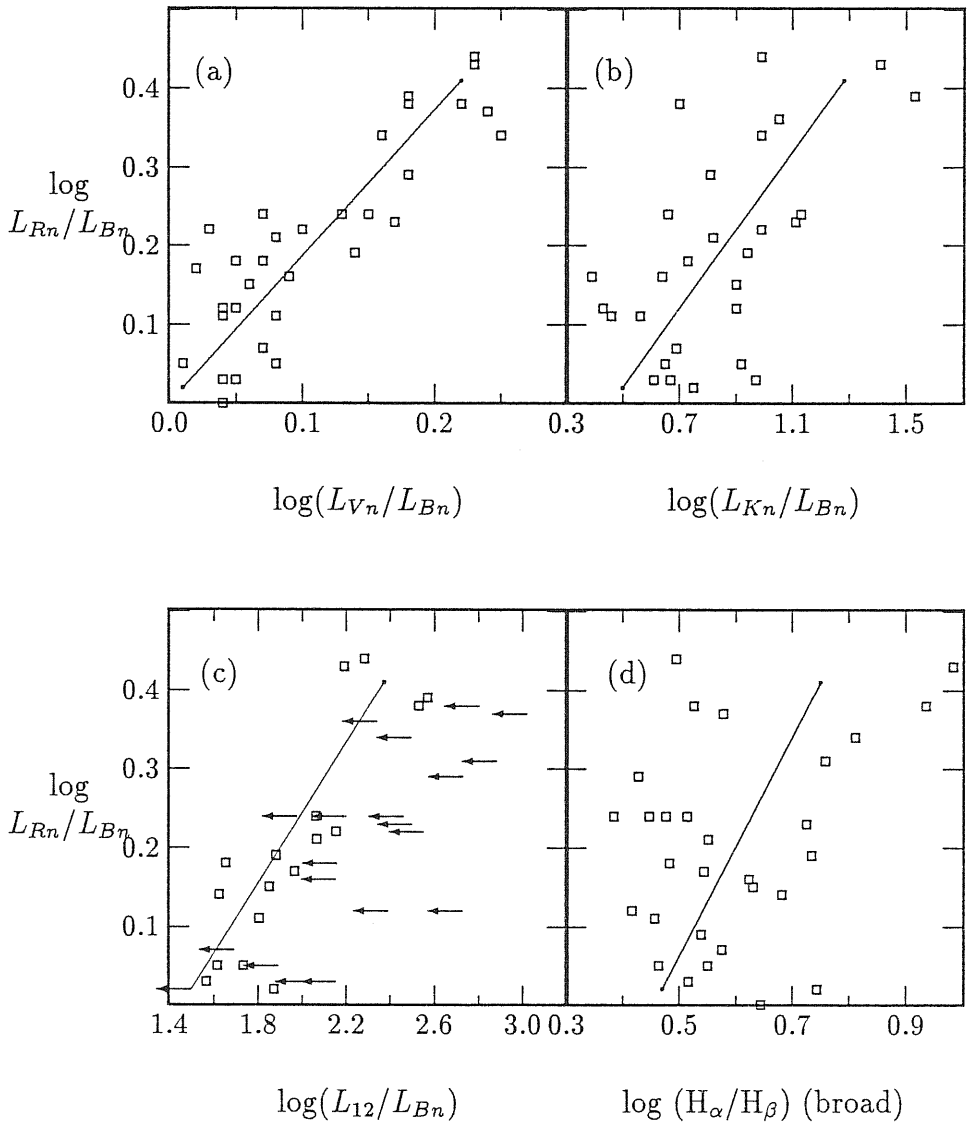

Figure 4.17: "Color–color" plots of L_V/L_B, L_K/L_B, L_{12}/L_B and of the Balmer decrement vs. L_R/L_B. The segments represents the reddening vectors corresponding to E(B-V)=0.5. In all but the last diagrams the points tend to cluster along the direction defined by these vectors.

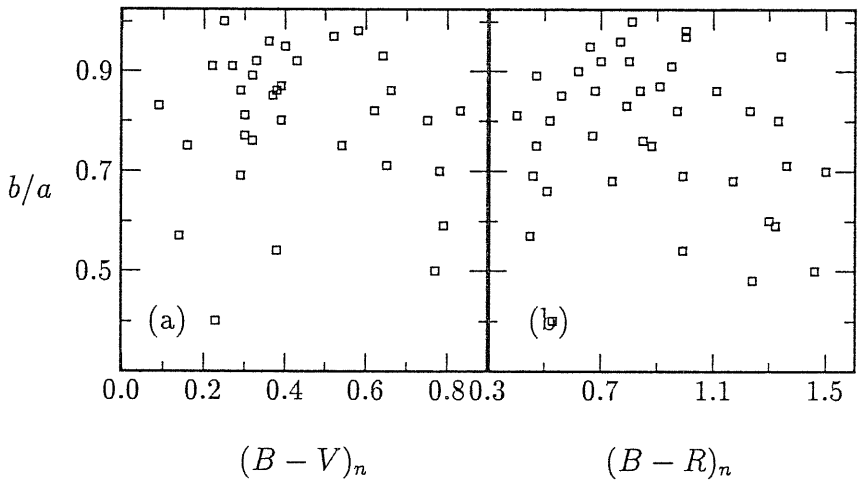

Figure 4.18: $(B-V)_n$ and $(B-R)_n$ colors of the bare nuclei against the axial ratios of the hosts.

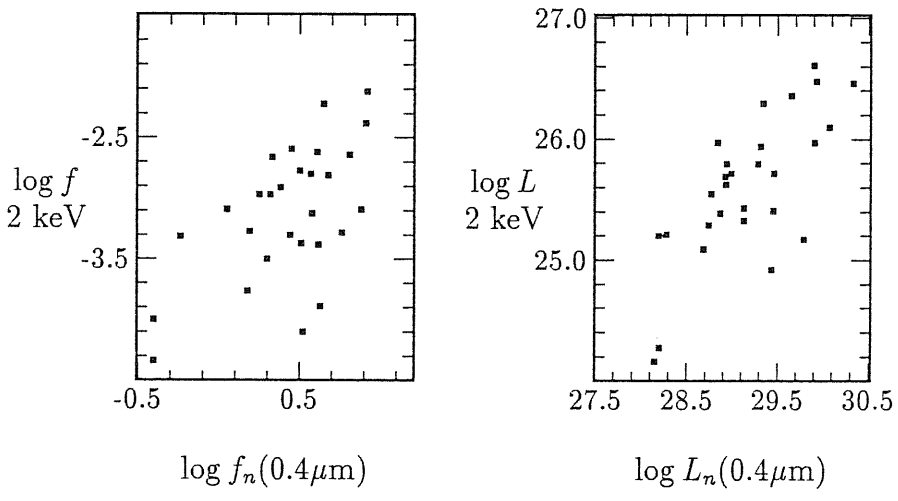

Figure 4.19: Correlation between the 2 keV and 0.4μm fluxes and luminosities.

Chapter 5

A model for the 0.1–100 μm SEDs

Summary. We have used the simple dust model for the IR emission described by Barvainis (1987,1990) to fit the UV–optical-infrared SEDs of some AGNs of our sample, for which we have derived in the previous chapters nuclear optical and infrared magnitudes. The model comprises a thermal emission by dust and a hot blackbody peaking in the UV which heats the dust, plus a template galactic far IR spectrum, with normalization given by the K band galactic magnitude, to take into account that IRAS fluxes include the emission from the host galaxy. The model is very simple and can be improved in many ways, but our purpose here is to show that the broad band 0.1–100 μm SEDs of radio quiet AGNs can be reproduced reasonably well without the inclusion of any nonthermal (power law) component, and to suggest possible direction of our work for the near future.

5.1 Introduction

The methods described in the last two chapters, among other things, have provided us with reliable determination of the nuclear magnitudes in the optical and infrared bands B V R J H K L, for many objects of the homogeneous sample defined in Chapter 2. Combining these data with available satellite observations in the UV (IUE), far IR (IRAS) and X–ray bands, plus ground based radio measurements, it is possible to obtain broad band nuclear SEDs over nine decades in frequency. A problem in doing this may be that these measurements are far from simultaneous, and the AGNs are known to be variable objects. However, for radio quiet AGNs, the

variability is not dramatic in most of the bands, and the requirement of simultaneous observations is not so stringent as in the case of Blazars, at least for statistical studies of large samples.

Our aim for the near future is to check, and if necessary to improve, the proposed models for radio quiet AGNs emission (Chapter 1) using our data. This chapter describes the first effort made in this direction. The considerations developed in the previous chapters tend to favor the dust picture for the IR emission of radio quiet AGNs. Therefore we have used, adapting it to our purposes, the dust model proposed by Barvainis (1987, 1990). We shall see that the model described below, though very simple, can provide reasonable fit to the nuclear SEDs from the far UV to the far IR.

5.2 The model

The nuclear SED in this spectral region is described with only two components closely linked together: an optical–UV thermal continuum, which we approximate with a single blackbody spectrum, and an IR thermal continuum, due to a distribution of dust which absorbs in part the primary optical–UV continuum, and thermally emits the energy absorbed at higher wavelengths, corresponding to the dust equilibrium temperature. We adopt at this stage the single blackbody representation of the blue bump, even if we are well aware that it is a crude oversimplification, since broader spectra such of those emitted by thin disks are known to provide better fits (see Chapter 1 and references therein). We do this because at the moment our aim is to demonstrate that a reasonable distribution of circumnuclear dust can explain the IR emission, if heated by the observed optical-UV radiation, and therefore only a rough functional description of the blue bump is needed. A blackbody with $T \sim$ few $\times 10^4$ K can be considered as a first order approximation of the spectra emitted by almost all the proposed model for the blue bump (Chapter 1). A precise choice between them seems premature here, probably implying the consideration also of the emission in the extreme–UV and soft–X regimes, and it is of little relevance for the limited purpose of this chapter.

The dust grains are supposed to be heated solely by the exposure to the primary optical–UV radiation, while the reemission in the IR is optically thin, since the absorption efficiency Q_ν of the grains is much smaller in the infrared than in the optical. The optically thin emission spectrum of grains at a given temperature T_{gr} is $Q_\nu B_\nu(T_{gr})$, where B_ν is the Planck function. With realistic choiches of Q_ν, the emission spectrum of a single temperature grain is found to be very narrow, and therefore to account for the emission in the whole IR regime requires grains with a broad range of T_{gr}. This situation can arise naturally if the dust is heated by the

central source, since grains at different distances will come into thermal equilibrium at different temperatures. In order to produce enough thermal IR radiation, the dust need to be optically thick to the optical-UV continuum. Since in the objects with which we are dealing here the optical radiation is observed, and appears affected by a relatively moderate internal reddening (at most $A_V = 1.5$, see Chapter 4), the covering factor of the dust distribution must be a fraction of one, in order to provide a less obscured view along our line of sight. There are two main possibilities: a smooth distribution of dust organized in a torus or disklike configuration, or a clumpy medium. Since the two situations led to very similar spectra (Barvainis 1987), which cannot be distinguished on the basis of fits to currently available data, we refer the following considerations to the former case, for which evidence has rapidly mounted in recent years (see for instance references in Krolik and Lepp 1989). The idea of dust organized in a torus is appealing in particular because it is usually invoked by the proposed unification schemes for the different classes of AGNs (e.g. Lawrence 1987; Blandford 1991), in which the orientation of this structure, with respect to our viewing angle, would produce the observational difference between types 1 and 2 Seyfert galaxies.

The characteristics of grains in AGNs are unknown, and are expected to be strongly affected by the environment (e.g. Chang et al. 1987). Graphite and silicate grains have been proposed as likely constituents of Galactic dust. Graphite has a significantly higher evaporation temperature ($\sim 1500 \div 2000$ K), and can therefore emit up to shorter wavelengths. Since the model aims to explain the IR emission down to $\sim 2\mu$m, it is simply assumed that the dust is composed by spherical graphite grains of radius $a = 0.05$ μm. For this grain radius a good approximation to the near–IR absorption efficiency is a power law $Q_\nu = q_{ir}\nu^\gamma$ with $q_{ir} = 1.4 \times 10^{-24}$ and $\gamma = 1.6$ (Barvainis 1987). Grains of other size would change only some numerical details of the model. The spectral luminosity of an individual grain in the infrared is given by

$$L_\nu^{gr} = 4\pi a^2 \pi Q_\nu B_\nu(T_{gr}) \tag{5.1}$$

The grain equilibrium temperature T_{gr} is found from the balance between the rate at which the energy is absorbed and the rate at which it is radiated. Approximating the ultraviolet absorption efficiency of the grains Q_{uv} as constant and equal to one, it is found:

$$T_{gr} = 1650 \left(\frac{L_{uv,46}}{r_{pc}^2} \right)^{1/5.6} e^{-\tau_{uv}/5.6} \quad \text{K} \tag{5.2}$$

where $L_{uv,46}$ is the optical-UV luminosity in units of 10^{46} ergs s^{-1}, r_{pc} is the distance from the central source in parsecs and τ_{uv} is the dust optical depth to the UV continuum. Interior to the evaporation radius r_1 the grains are destroyed by

Name	$L_{uv,46}$	$T_{bb}[10^4\mathrm{K}]$	E_{B-V}	$\Omega/4\pi$	β	$\log(r_2/r_1)$	r_1[pc]	$\log M_d$
I Zw 1	.90	1.69	.35	.74	.78	4.36	1.05	8.19
II Zw 136	.50	2.25	.23	.39	.78	4.03	.92	7.06
Mkn 79	.10	2.42	.27	.39	.74	4.27	.41	6.85
Mkn 335	.26	2.48	.24	.27	.84	2.75	.66	4.08
Mkn 376	.24	1.47	.24	.63	.19	1.88	.72	3.19
Mkn 478	1.24	2.14	.30	.16	.88	2.45	1.45	3.92
Mkn 486	.07	1.28	.21	.62	.80	2.79	.35	4.01
Mkn 509	.29	1.45	.14	.34	.87	3.16	.70	4.97

Table 5.1: Parameters of fits.

evaporation. This occurs when the equation 5.2 would yield a temperature to high for the dust to survive. From this condition, it is found

$$r_1 = 1.3 L_{uv,46}^{1/2} T_{1500}^{-2.8} \quad \mathrm{pc} \tag{5.3}$$

where T_{1500} is the grain evaporation temperature in units of 1500 K, which we set equal to one.

The dust is assumed to follow a radial number density law of the form

$$n_{gr}(r) = n_{gr,1}(r/r_1)^{-\beta} \tag{5.4}$$

The inner radius of this dust distribution is given by equation 5.3, while the outer radius is set by the condition that the optical depth to the UV radiation becomes significantly greater than one, say $\tau_{uv}(r_2) = 3$, since beyond r_2 the grains are no longer heated by the UV continuum. The optical depth is given by

$$\tau_{uv}(r) = \pi a^2 \int_{r_1}^{r} n_{gr}(r')dr' \tag{5.5}$$

Since the dust is optically thin to its own radiation, the total infrared spectral luminosity is obtained integrating the contribution from all grains between r_1 and r_2:

$$L_{\nu,ir} = \Omega \int_{r_1}^{r_2} n_{gr} L_\nu^{gr} r^2 dr \tag{5.6}$$

where Ω is the solid angle subtended by the dust distribution at the nucleus.

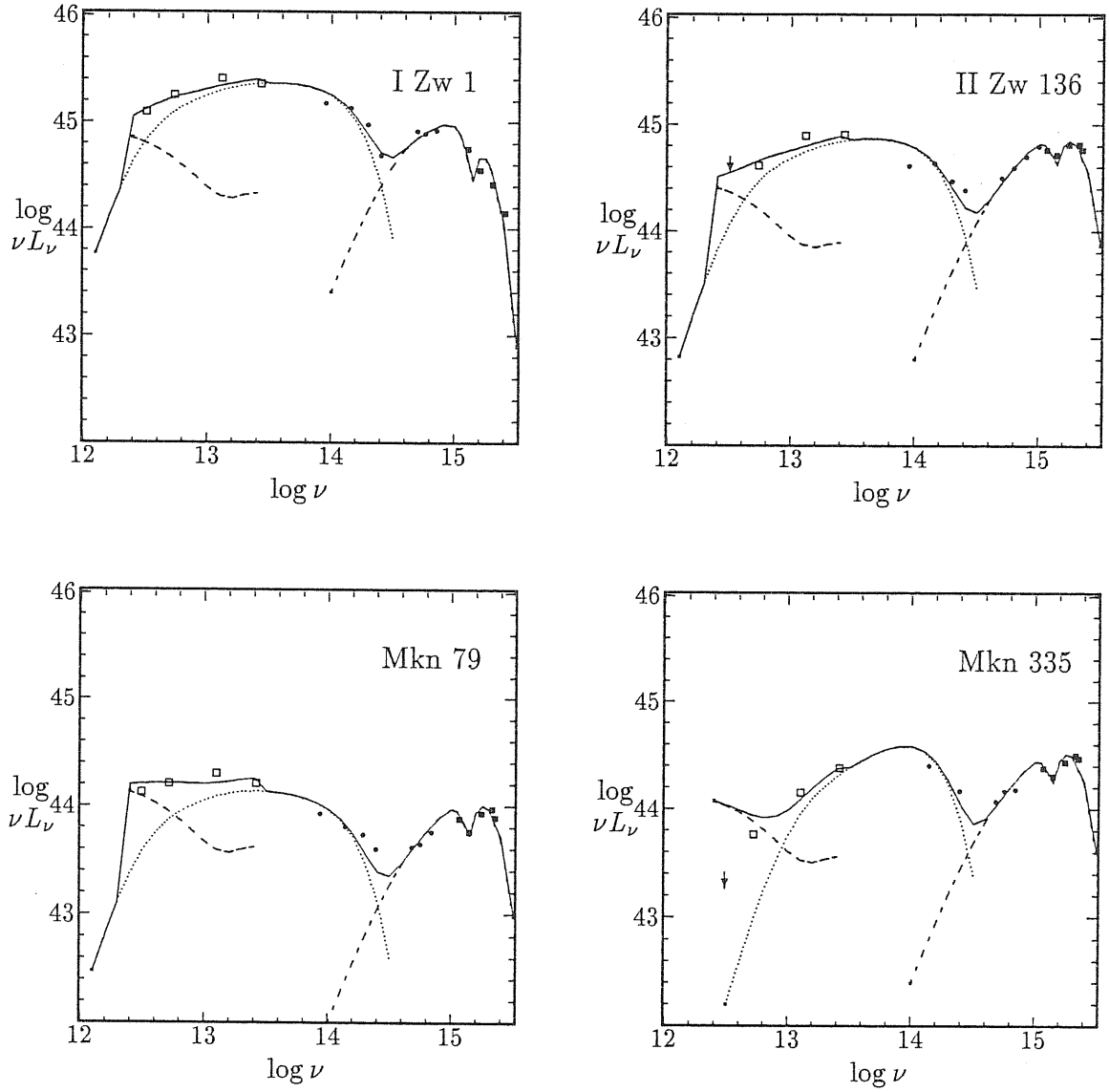

Figure 5.1: SEDs and fits obtained with the model described in the text for four objects. The SEDs have been constructed using IRAS data (open squares), near–IR and optical nuclear magnitudes derived in Chapters 3 and 4 (filled circles) and IUE data (filled squares). The global best fits (solid lines), the dust (dotted), the optical–UV blackbody (short–long dashed), and the template galactic far–IR spectra (dashed) are reported.

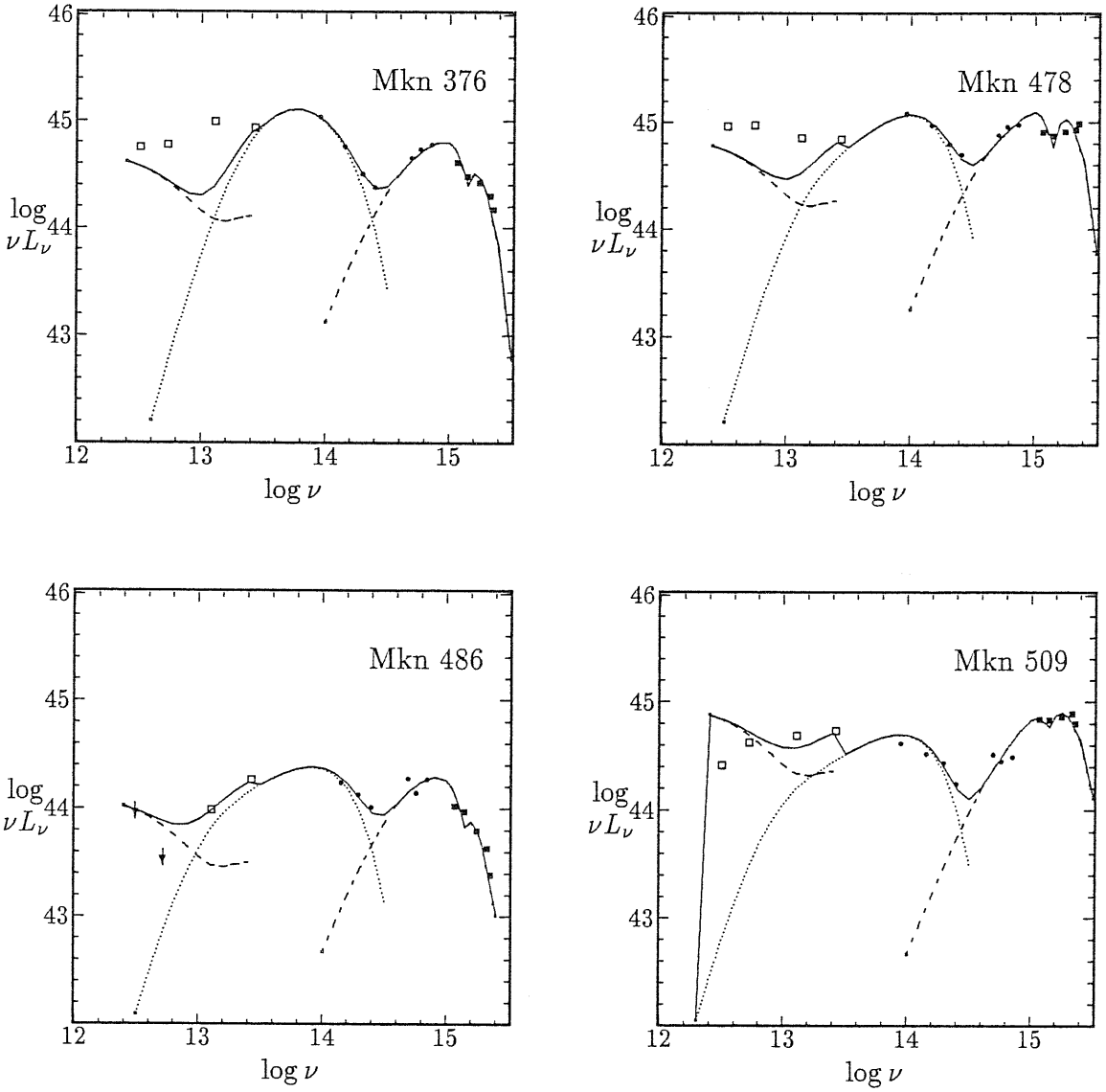

Figure 5.2: Same as the previous figure.

5.3 Fits to AGN spectra

With the model described above, we have fitted the 0.1–100 μm SEDs of 8 objects for which we have collected enough data to construct reasonably well sampled spectra. The IRAS data for all the objects of our sample have been collected in Granato 1988. For the near-IR and optical portion of the spectrum we used the determinations of nuclear magnitudes which we have obtained in Chapters 3 and 4, except in the case of II Zw 136 for which we used the optical data reported by Sun and Malkan 1989. As for the UV data, we have collected, using the package ULDA, all the good quality spectra of our objects available in the IUE database, averaging the flux in five 100 Å regions, for which the contamination from lines have been estimated by Chapman et al. 1985 to be less than 10%. The SEDs so obtained have been reported to the rest frames of the nuclei.

The adjustable parameters of the dust model which fits the IR part of the spectrum are β, r_2/r_1 (or equivalently the grain density at r_1, $n_{gr,1}$) and Ω, which serves as a normalization factor between the UV and IR luminosity ($L_{ir}/L_{uv} = \Omega/4\pi$). The optical-UV blackbody is described by other two parameters: the blackbody temperature T_{bb} and the total luminosity $L_{uv,46}$. The last free parameter we have used in our fit is the color excess $E(B-V)$, which defines the amount of internal reddening in the optical-UV continuum. Indeed, even if we have assumed that the UV continuum is observed from directions essentially free from the the dust which is responsible of the bulk of the IR emission, it is nevertheless affected by a moderate reddening. In fact, in many of the objects for which we have IUE data, the characteristic dust absorption feature around 2200 Å is clearly discernible. The reddened blackbody spectrum is computed, for a given value of $E(B-V)$ using the standard Galactic reddening law (Seaton 1979). The applicability of this curve to the environment of an AGN is somewhat questionable, but this is at the moment the best we can do. In particular, it is troublesome the fact the value of $E(B-V)$ obtained from the fit is set primarily by the 2200 Å feature, which is attributed mainly to graphite grains (Mathis et al. 1977), and therefore it is expected to be sensitive to the dust composition (Seab and Shull 1983). The problem becomes worse when one realizes that the value of this parameter is closely coupled with the derived UV intrinsic luminosity (before absorption) and therefore with the dust covering factor $\Omega/4\pi$.

The analysis presented in the previous chapters, in particular in Chapter 3, has demonstrated that the 60 and 100 μm IRAS fluxes are mainly contributed by the host galaxy, and therefore we cannot hope to fit these data with the model described so far. To check this, and to circumvent somehow the problem, we have tried three different approaches in our fits: (i) we have ignored the 60 and 100

μm data; (ii) we have tried to fit also these data with the dust model; (ii) we have introduced a template far-IR galactic spectrum, obtained interpolating the average ratios $L(12\mu\text{m})/L(2.2\mu\text{m})$, $L(25\mu\text{m})/L(2.2\mu\text{m})$, $L(60\mu\text{m})/L(2.2\mu\text{m})$ and $L(100\mu\text{m})/L(2.2\mu\text{m})$ reported in Section 3.4.2. The normalization of this template spectrum is given by the host galaxy K band magnitudes that we have derived in Chapter 3, and therefore this last method does not introduce any additional free parameter. In many cases the method (ii) has given unsatisfactory results: sometimes it was simply impossible to fit the 60 and 100 μm data, and even when it was formally possible, the outer radius of the dust distribution so obtained was of the same order of the galactic radius or larger. On the contrary, methods (i) and (iii) gave usually very similar and reasonable solutions, and when this happened we have reported the results obtained with (iii). However, for two objects, Mkn 376 and Mkn 478, it was not possible to get a good fit with (iii). We think that the reason is that in this case the template far–IR host galaxy is badly inadequate to describe the far IR observations. For these objects we have instead reported a fit obtained excluding the 25, 60 and 100 μm data, which describes very well the remaining portion of the SED. In general we explicitly note that it is not surprising that our fits can have problems in describing the far IR data, even those obtained with method (iii). Indeed the far IR to K band luminosity ratios in normal galaxies have a quite broad distributions, ranging over one order of magnitude or more (see Section 3.4.2). In particular the 60 to 100 μm spectral index of normal galaxies ranges typically from -2 to +1. Despite this, the fits we have obtained for the remaining 6 objects are rather good at least up to 60 μm.

The best fit solutions have been obtained by χ^2 minimization, using the routine MRQMIN described in Press et al. 1986 and giving to all the data points the same weight. The fits are presented in the Figures 5.1 and 5.2, showing the individual model components as well as their sum. The corresponding fitting parameters are listed in Table 5.1, together with the dust evaporation radius r_1 and the total mass of the emitting dust M_d.

5.4 Conclusion

As we anticipated, this chapter describes a first effort of modeling the nuclear SEDs we derived for the objects in our sample. The model presented can be improved in many ways, and the effects of the simplifing assumption concerning the dust properties must be studied. More physical models for the optical–UV continuum can be considered, with particular attention to those suspected to play a role in the production of X–rays photons. These topics will be objects of our work in the next future, and therefore a detailed discussion of the results obtained so far seems

premature.

It is anyway promising for the dust emission picture that this simple model reproduces well, and with reasonable masses of the emitting dust, the main features of the observed SEDs of non blazar AGNs, in particular the universally seen minimum at $\log \nu \simeq 14.5$ (1 μm), which is explained as due to the sharp cutoff of the dust emission around this frequency, resulting from dust sublimation above $T \sim 1500$ K.

This picture, if substantially correct, may have deep consequences. It implies that AGNs can be heavily obscured along our line of sight (the typical covering factor we have found is ~ 0.5), and therefore it is possible that an entire population of such objects is missing in optical and soft X–ray surveys, but could be found with mid–IR instruments well suited to detect the hot dust emission associated with the absorbing material (e.g. ISOCAM). These objects may be extremely relevant in connection with the still open problem of the origin of the X–ray background. As already noticed, the idea of dust torii is also closely linked with unified theories of AGNs.

Bibliography

Adams, T. F. 1977, ApJS, 33, 19.

Aitken, D. K. and Roche, P. F. 1985, MNRAS, 213, 777.

Aitken, D. K., Roche, R. J., and Phillips, M. M. 1981, MNRAS, 196, 101P.

Allen, D. A. 1976, ApJ, 207, 367.

Balzano, W. A. and Weedman, D. W. 1981, ApJ, 243, 756.

Band, D. L. and A, M. M. 1989, ApJ, 345, 122.

Bardeen, J. M. 1970, ApJ, 162, 71.

Barvainis, R. 1987, ApJ, 320, 537.

Barvainis, R. 1990, ApJ, 353, 419.

Begelman, M. C. 1990. In Miller, J. S., editor, *Astrophysics of Active Galaxies and Quasi-Stellar Objects*, page 411. Oxford University Press.

Berriman, G. 1989, ApJ, 345, 713.

Blandford, R. D. 1991. In Corvoisier, T. J. L. and Mayor, M., editors, *Active Galactic Nuclei*, page 161. Springer–Verlag.

Bollea, D. and Cavaliere, A. 1976, A&A, 49, 313.

Boronson, T. 1981, ApJS, 46, 177.

Bregoli, G., Federici, L., Focardi, P., Merighi, R., Oculi, L., Piccioni, A., Volta, O., and Zitelli, V. 1990. In Baluteau, J. P. and D'odorico, S., editors, *The Optimization of the use of CCD Detectors in Astronomy*, page 177.

Campins, H., Rieke, G. H., and Lebofsky, M. J. 1985, AJ, 90, 896.

Carico, D. P., Sanders, D. B., Soifer, B. T., Elias, J. H., Matthews, K., and Neugebauer, G. 1988, AJ, 95, 356.

Carleton, N. P., Elvis, M., Fabbiano, G., Willner, S. P., Lawrence, A., and Ward, M. 1987, ApJ, 318, 595.

Chang, C. A., Schiano, A. V. R., and Wolfe, M. 1987, ApJ, 322, 180.

Chapman, G. N. F., Geller, M. J., and Hucra, J. P. 1985, ApJ, 297, 151.

Cheng, F. Z., Danese, L., and De Zotti, G. 1983, MNRAS, 204, 13P.

Cheng, F. Z., Danese, L., and De Zotti, G. 1985, MNRAS, 212, 857.

Chini, R., Kreysa, E., and Biermann, P. L. 1989, A&A, 219, 87.

Clavel, J., Wamsteker, W., and Glass, I. S. 1989, ApJ, 337, 236.

Coleman, H. H. and Shields, G. A. 1990, ApJ, 363, 415.

Collin-Souffrin, S. 1991, A&A.

Cutri, R. M., Rudy, R. J., Rieke, G. H., Tokunaga, A. T., and Willner, S. P. 1984, ApJ, 280, 512.

Czerny, B. and Elvis, M. 1987, ApJ, 321, 305.

Danese, L., Zitelli, V., Granato, G. L., Wade, R., De Zotti, G., and Mandolesi, N. 1991, submitted to APJ.

Devereux, N. A. 1987, ApJ, 323, 91.

Devereux, N. A. 1989, ApJ, 346, 126.

Devereux, N. A., Becklin, E. E., and Scoville, N. 1987, ApJ, 312, 529.

Edelson, R. A. and Malkan, M. A. 1986, ApJ, 308, 59.

Edelson, R. A. and Malkan, M. A. 1987, ApJ, 323, 516.

Edelson, R. A., Malkan, M. A., and Rieke, G. H. 1987, ApJ, 321, 233.

Elvis, M., Green, R. F., Bechtold, J., Schmidt, M., Neugebauer, G., Soifer, B. T., Matthews, K., and Fabbiano, G. 1986, ApJ, 310, 291.

Elvis, M., Wilkes, B. J., and McDowell, J. C. 1990. In Malina, R. F. and Bowyer, S., editors, *Extreme Ultraviolet Astronomy.* Pergamon.

Engargiola, G., Harper, D. A., Elvis, M., and Willner, S. P. 1988, ApJ, 332, L19.

Felten, J. E. 1977, AJ, 82, 861.

Ferland, G. J. and Rees, M. J. 1988, ApJ, 332, 141.

Franceschini, A., Toffolatti, L., Mazzei, P., Danese, L., and De Zotti, G. 1990, A&AS, in press.

Frank, J., King, A. R., and Raine, D. J. 1985. *Accretion Power in Astrophysics.* Cambridge University Press.

Freeman, K. C. 1970, ApJ, 160, 811.

Geheren, T., Fried, J., Wehinger, P. A., and Wyckoff, S. 1984, ApJ, 278, 11.

Ghisellini, G., Guilbert, P. W., and Svensson, R. 1988, ApJ, 334, L5.

Glass, I. S. 1973, MNRAS, 164, 155.

Glass, I. S. 1979, MNRAS, 186, 29P.

Glass, I. S. and Moonrwood, A. F. M. 1985, MNRAS, 211, 461.

Granato, G. L. 1988. *Degree Thesis Universitá di Padova.*

Griersmith, D., Hyland, A. R., and Jones, T. J. 1982, AJ, 87, 1106.

Guilbert, P. W. and Rees, M. J. 1988, MNRAS, 233, 475.

Haardt, F. and Maraschi, L. 1991, Preprint.

Heckman, T. M., Blitz, L., Wilson, A. S., Armus, L., and Miley, G. K. 1989, ApJ, 342, 735.

Hutchings, J. B., Crampton, D., and Campbell, B. 1984, ApJ, 280, 41.

Isobe, T., Feigelson, E. D., and Nelson, P. I. 1986, ApJ, 306, 490.

Kent, S. 1985, ApJS, 59, 115.

Kolykhalov and Sunyaev 1984, Adv. Space Res., 3, 249.

Kriss, G. A. 1988, ApJ, 324, 809.

Krolik, J. H. and Kalmann 1987.

Krolik, J. H. and Lepp, S. 1989, ApJ, 347, 179.

Kruper, J. S. and Canizares, C. R. 1989, ApJ, 343, 66.

Laor, A. and Netzer, H. 1989, MNRAS, 238, 897.

Laor, A., Netzer, H., and Piran, T. 1990, MNRAS, 242, 560.

Lawrence, A. 1987, PASP, 99, 309.

Lawrence, A., Rowan-Robinson, M., Efstathiou, A., Ward, M. J., Elvis, M., Smith, M. G., Duncan, W. D., and Robson, I. E. 1991, MNRAS, 248, 91.

Lawrence, A., Ward, M., Elvis, M., Fabbiano, G., Willner, S. P., Carleton, N. P., and Longmore, A. 1985, ApJ, 291, 117.

Lightman, A. P. and White, T. R. 1988, ApJ, 335, 57.

Maccacaro, T., Gioia, I. M., Wolter, A., Zamorani, G., and Stocke, J. T. 1988, ApJ, 326, 680.

MacKenty, J. W. 1990, ApJS, 72, 231.

Macklin, J. T. 1982, MNRAS, 199, 1119.

Madau, P. 1988, ApJ, 327, 116.

Malkan, M. A. 1983, ApJ, 268, 582.

Malkan, M. A. 1984, ApJ, 287, 555.

Malkan, M. A. 1988, Adv. Space Res., 8, 49.

Malkan, M. A. and Filippenko, A. V. 1983, ApJ, 275, 477.

Maraschi, L. and Molendi, S. 1990, Preprint.

Marsiaj, P. 1991. *Degree Thesis Universitá di Padova.*

Mathis, J. S., Rumpl, W., and Nordsieck, K. H. 1977, ApJ, 217, 425.

McAlary, C. W., McLaren, R. A., Dennis, R., and Crabtree, D. R. 1979, ApJ, 234, 471.

McAlary, C. W., McLaren, R. A., McGonegal, R. J., and J, M. 1983, ApJS, 52, 341.

McAlary, C. W. and Rieke, G. H. 1988, ApJ, 333, 1.

McLean, I. S., Chuter, T. C., McCaughrean, M. J., and Rayner, J. T. 1986, Proceedings of SPIE, 627, 430.

Meixer, M., Puchalsky, R., Blitz, L., Wright, M., and Heckman, T. 1990, ApJ, 354, 158.

Mushotzky, R. F. and Wandel, A. 1989, ApJ, 339, 674.

Netzer 1997, MNRAS, 225, 55.

Neugebauer, G., Matthews, K., Soifer, B. T., and Elias, J. H. 1985, ApJ, 298, 275.

Neugebauer, G., Oke, J., Becklin, E., and Matthews, K. 1979, ApJ, 230, 79.

Neyman, J. and Scott, E. L. 1961. In *Proc of 4th Berkeley Symp. Math. Stat. and Prob. Vol. 3*, page 261. University of California Press, Berkeley.

Neyman, J. and Scott, E. L. 1974. In *Confrontation of Cosmological Theories with Observational Data, IUA Symp. No. 63*, page 129.

Novikov, I D Thorne, K. S. 1973. Black holes.

O'Dell, S. L. e. a. 1987, ApJ, 313, 164.

Page, D. N. and Thorne, K. S. 1974, ApJ, 191, 499.

Penston, M. V., Penston, M. J., Selmes, R. A., Becklin, E. E., and Neugebauer, G. 1974, MNRAS, 169, 357.

Piccinotti, G., Mushotzky, R. F., Boldt, E. A., Holt, S. S., Marshall, F. E., Serlemitsos, P. J., and Shafer, R. A. 1982, ApJ, 253, 485.

Pounds, K. 1989. In *Proc of the* 23^d *ESLAB Symposium on X-Ray Astronomy ESA SP-296*, page 753.

Press, W. H., Flannery, B. P., Teukolsky, S. A., and Vetterling, W. T. 1986. *Numerical Recipes.* Cambridge University Press.

Rees, M. J., Silk, J. I., Werner, M. W., and Wickramsinghe, M. C. 1969, Nature, 223, 788.

Rieke, G. H. 1978, ApJ, 226, 550.

Rieke, G. H., Lebofsky, M. J., Thompson, R. I., Low, F. J., and Tokunaga, A. T. 1980, ApJ, 238, 24.

Rieke, G H Cutri, R. M., Black, J. H., Kailey, W. F., McAlary, C. W., Lebofsky, M. J., and R, E. 1985, ApJ, 290, 116.

Rodriguez Espinosa, J. M., Rudy, R. J., and Jones, B. 1986, ApJ, 309, 76.

Rodriguez Espinosa, J. M., Rudy, R. J., and Jones, B. 1987, ApJ, 312, 555.

Rudy, R. J., LeVan, P. D., Puetter, R. C., Smith, H. E., Willner, S. P., and Tokunaga, A. T. 1982a, ApJ, 257, 570.

Rudy, R. J., LeVan, P. D., and Rodriguez-Espinosa, J. M. 1982b, AJ, 87, 598.

Sandage, A. R. 1973, ApJ, 180, 687.

Sanders, D. B., Phinney, E. S., Neugebauer, G., Soifer, B. T., and Matthews, K. 1989, ApJ, 347, 29.

Schmidt, M. and Green, R. F. 1983, ApJ, 269, 352.

Schmitt, J. H. M. M. 1985, ApJ, 293, 178.

Scoville, N. Z., Soifer, B. T., Neugebauer, G., Young, J. S., Matthews, K., and Yerka, J. 1985, ApJ, 289, 129.

Seab, C. G. and Shull, J. M. 1983, ApJ, 275, 652.

Seaton, M. J. 1979, MNRAS, 187, 73P.

Sekigichi, K. 1987, ApJ, 316, 145.

Shakura, N. I. and Sunyaev, R. A. 1973, A&A, 24, 337.

Shields, G. A. 1974, ApJ, 191, 309.

Shields, G. A. 1978, Nature, 272, 706.

Simkin, S. M., Su, H. J., and Schwarz, M. P. 1980, ApJ, 237, 404.

Simons, D. A., Tokunaga, A. T., Rudy, R. J., and Stein, W. A. 1988, AJ, 96, 481.

Smith, E. P., Heckman, T. M., Bothun, G. D., Romashin, W., and Balick, B. 1986, ApJ, 306, 64.

Spinoglio, L. and Malkan, M. A. 1989, ApJ, 342, 83.

Stein, W. A. and Weedman, D. W. 1976, ApJ, 205, 44.

Sun, W. H. and Malkan, M. A. 1989, ApJ, 346, 68.

Thuan, T. X. and Gunn, J. E. 1976, PASP, 88, 543.

Treves, A., Maraschi, L., and Abramowicz, M. 1988, PASP, 100, 427.

Turner, T. J. and Pounds, K. A. 1989, MNRAS, 240, 833.

Veron-Cetty, M. P. and Woltjer, L. 1990, A&A, 236, 69.

Wade, R. A. 1984, MNRAS, 208, 381.

Wandel, A. 1987, ApJ, 316, L55.

Ward, M., Allen, T. A., Wilson, A. S., Smith, M. G., and Wright, A. E. 1982, MNRAS, 199, 953.

Ward, M., Elvis, M., Fabbiano, G., Carleton, N. P., Willner, S. P., and Lawrence, A. 1987, ApJS, 63, 615.

Webb, W. and Malkan, M. A. 1986. In Mason, K. O., Watson, M. G., and White, N. E., editors, *The Physics of Accretion onto Compact Objects*, page 15. Springer Verlag, Berlin.

Wilkes, B. J. and Elvis, M. 1987, ApJ, 323, 243.

Wills, B. J., Netzer, H., and Wills, D. 1985, ApJ, 288, 94.

Wilson, A. S. 1979, Proc. Roy. Soc. Lon., 366, 461.

Woltjer, L. 1991. In Corvoisier, T. J. L. and Mayor, M., editors, *Active Galactic Nuclei*, page 1. Springer–Verlag.

Worral, D. M., Puschell, J. J., Bruhweiler, F. C., Miller, H. R., Aller, M. F., and Aller, H. D. 1984, PASP, 96, 699.

Xu, C. and De Zotti, G. 1989, A&A, 225, 12.

Yee, H. K. C. 1983, ApJ, 272, 473.

Zitelli, V., Granato, G. L., Mandolesi, N., Wade, R., and Danese, L. 1991, submitted to APJS.